Understanding the gamma-ray emission from Globular Clusters

ABIGAIL KATHARINE PEAKE

Abstract

Observations with the Large Area Telescope (LAT) on-board the *Fermi* Gamma-ray Space Telescope have led to the discovery of gamma-ray emission from many Globular Clusters. The high stellar encounter rates in Globular Clusters favour the formation of millisecond pulsars, which have been postulated as the source of the gamma-ray emission. However, the evidence for this is indirect and there have been limited studies attempting detailed spectral comparison between Globular Clusters and their millisecond pulsar populations. The detection of pulsed gamma-ray emission would constitute direct evidence of millisecond pulsars contributing to the Globular Cluster emission.

In this work, I use 13 years of *Fermi*-LAT data to perform a detailed spectral analysis of 6 Globular Clusters where no pulsed gamma-ray emission has been reported, but millisecond pulsars have been detected using radio telescopes. I also analyse the Globular Cluster NGC 6624, where pulsed gamma-ray emission has already been observed and find that a single millisecond pulsar can account for the majority of NGC 6624's gamma-ray emission over 13 years. I then find no evidence of any statistically significant pulsed emission in any of the Globular Clusters I selected. Based on these findings and motivated by previous studies, I consider the possibility of dark matter annihilation contributing to the Globular Cluster emission. I perform likelihood fits of three scenarios for the Globular Cluster emission: dark matter only, millisecond pulsars only, and a combination of millisecond pulsars and dark matter. I use these results to place upper limits on the millisecond pulsar contribution to the gamma-ray emission in each Globular Cluster. I find evidence that the millisecond pulsars in some of the Globular Clusters are fainter than those in the Galactic neighbourhood. Finally, I conclude that a dark matter component cannot be ruled out for any of the Globular Clusters I studied.

Understanding the gamma-ray emission from Globular Clusters

Abigail K. Peake

A Thesis presented for the degree of Master of Science by Thesis

Supervisors: A. M. Brown and P. M. Chadwick

Gamma-ray Astronomy Group
Department of Physics
University of Durham

August 2022

Contents

List of Tables

List of Figures

The work in this thesis is based on research carried out by the author in the Department of Physics, Durham University, UK, under the supervision of Dr Anthony M. Brown. and Prof Paula M. Chadwick. No part of this thesis has been submitted elsewhere for any other degree or qualification.

I would like to thank Anthony and Paula for being wonderful supervisors this past year. I am very grateful to them both for agreeing to supervise me, and for all their support, advice and encouragement. I would like to thank everyone in the Gamma-ray astronomy group for making my trips to Durham so enjoyable. I am particularly grateful to Sheridan for sharing his insight and for our discussions on Globular Clusters and Millisecond pulsars. I would also particularly like to thank Max and Cameron for their IT support and assistance with *Fermi* analysis.

I would finally like to thank my family and friends for all their help and support, particularly over the past year.

This work has made use of public *Fermi* data obtained from the High Energy Astrophysics Science Archive Research Center (HEASARC), provided by NASA Goddard Space Flight Center.

For Mum and Dad

Chapter 1

Introduction

1.1 Gamma-ray Astronomy

Gamma-rays are photons with energies over 511 keV[1]. The field of gamma-ray astronomy usually refers to the observation of photons with energies above 100 MeV, with the most energetic photons detected being around 100 TeV [43].

The advancement of satellite technology in the 1960s allowed gamma-ray astronomy to become an advancing and exciting field. Gamma-rays originating from the direction of the Galactic centre were first detected using the OSO III satellite in 1967 [89]. Since then, both space and ground based instruments have been used to observe the entire sky in gamma-rays. This has led to the discovery of the diffuse gamma-ray background surrounding the Galactic plane [71] and many, discrete sources of gamma-ray emission. Some of the first and most notable discoveries within the Milky Way include the pulsars detected within the Crab and Vela Supernova remnants [45, 126] by the COS-B satellite. Since then many more galactic point sources with associated gamma-ray emission have been discovered including pulsar wind nebulae [31], supernova shell remnants [6], cataclysmic variables [116] and low mass X-ray binary stars [14]. Extra-galactic gamma-rays have also been detected: it is thought that the cores of Active Galactic Nuclei (AGN) are a dominant source of these extra-galactic gamma-rays. Recent studies have also concluded that some of the diffuse, extra-galactic gamma-rays originate from radio galaxies [121].

1.2 Producing Gamma-rays

Gamma-rays are produced by predominantly two different processes:

1. Leptonic processes, where high energy electrons and positrons are accelerated by magnetic fields, and are boosted by interactions with other photons. This is known as the Inverse Compton effect.

2. Hadronic processes where high energy protons and nuclei interact, producing short lived particles (often π_0) which then decay into photons. This usually occurs in dense regions (such as a supernova remnant) and can produce very high energy photons of order GeV.

[1] $0.511\,\mathrm{MeV/c^2}$is the rest mass of an electron, and a pair of gamma-ray photons can be produced during electron-positron annihilation.

As gamma-rays are electromagnetic radiation and therefore follow a straight trajectory through space-time, observation of gamma-rays enables us to identify the positions of discrete sources that produce gamma-rays (which therefore implies there is likely particle acceleration and high magnetic fields in that object). Identifying these objects enables them to be studied. Additionally, studying the spatial distribution of diffuse gamma-ray emission provides information about the motion of charged particles through the ambient magnetic fields on an inter and extra galactic scale which enables us to determine the spatial and energy distributions of high energy charged particles in the Universe, which may enable us to shed insight on the elusive dark matter, dark energy and the matter antimatter asymmetry in the Universe [62].

1.3 Observing Gamma-rays

Gamma-rays are absorbed in the Earth's upper atmosphere which means that space based instruments are required to directly observe and detect gamma-rays for astronomical observations. Space based instruments are generally most sensitive to gamma-rays below energies of 100 GeV. Higher energy photons (above 100 GeV) are far less abundant and therefore have a much smaller flux and they also tend to pass straight through the detector. In order to detect these photons, a large detection area is needed. Ground based instruments (notably HESS [2] and the upcoming Cherenkov Telescope Array (CTA)) are considerably larger than space based instruments (for obvious reasons) and can be used to detect high energy photons indirectly. Indirect detection is when the gamma-rays are converted into showers of particles in the atmosphere (known as air showers). Ground based instruments measure the Cherenkov radiation emitted by the air showers and use this to reconstruct the energy and directionality of the incident photons. [62]

In this work, I am going to be using data obtained with the *Fermi* Large Area Telescope (referred to as *Fermi*-LAT) which is currently the most sensitive space based gamma-ray instrument.

1.4 The *Fermi* Gamma-ray Space Telescope

The *Fermi* Gamma-ray space Telescope (FGST, formerly known as GLAST [3]) is an international and multi-agency space observatory operated by NASA (pictured in Figure 1.1) designed to study cosmic gamma-ray photons. FGST was launched on 11th June 2008 and has been operating ever since, the satellite is in a low Earth orbit (with a period of around 95 minutes) enabling observations of the entire sky. There are two main instruments on board of FGST, which are the gamma-ray burst monitor (GBM) and the Large Area Telescope (known as *Fermi*-LAT which is the instrument I am using data from for my analysis). Since the launch, *Fermi*-LAT has surveyed the whole sky in order to create a map of all sources of gamma-rays (as shown in Figure 1.2) and can also focus on specific sources of interest (such as a gamma-ray burst).

Fermi-LAT was originally intended to operate for ten years but is still, at the time of writing, taking data. The *Fermi*-LAT collaboration publishes all data online and it

[2] an acronym for the High Energy Stereoscopic System
[3] an acroynm for the Gamma-ray Large Area Space Telescope

is open access via the *Fermi* Science support centre [4].

Figure 1.1: An artist's impression of the *Fermi* Gamma-ray space Telescope observatory *Image Credit: NASA/DOE/Fermi LAT Collaboration*

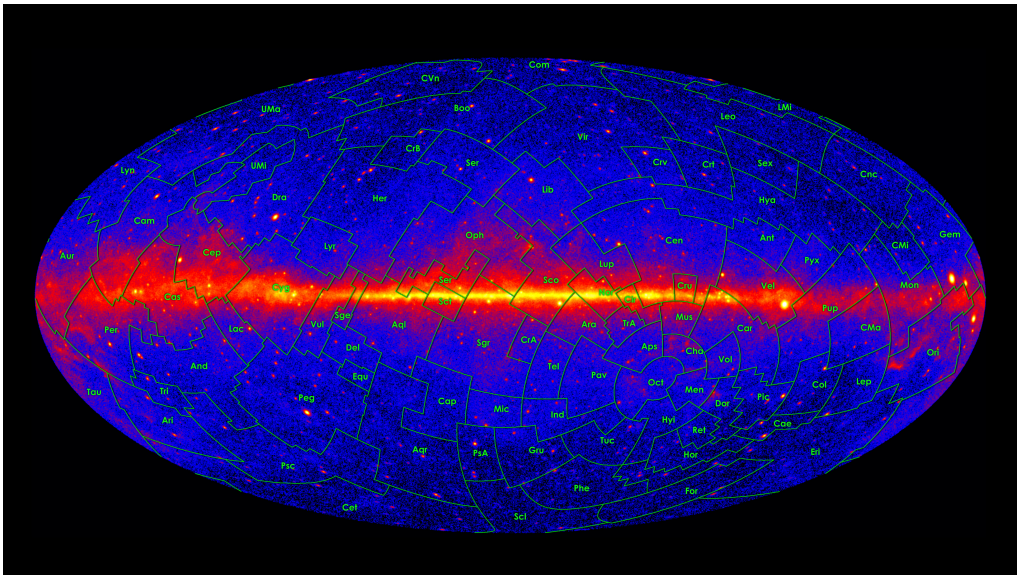

Figure 1.2: Taken from [48]. The *Fermi*-LAT 60-month image, constructed from front-converting gamma-rays with energies greater than 1 GeV. The most prominent feature is the bright band of diffuse glow along the map's centre, which marks the central plane of our Milky Way galaxy.

1.5 How *Fermi*-LAT Works

Fermi-LAT is an imaging, high energy gamma-ray telescope (capable of detecting photons in an energy range of 20 MeV-300 GeV). Despite having a small cross-sectional area (40×40 cm^2), LAT has a very large field of view of 2 steradians (which corresponds to viewing around one-fifth of the sky at a time). The LAT has four subsystems that enable the detection of gamma-rays and the rejection of the intense background produced by Cosmic Rays. Cosmic rays are high energy protons and atomic nuclei, originating from the Sun, and also from outside the Solar system, which move at relativistic speeds.

[4] *Fermi* Science support centre: `https://fermi.gsfc.nasa.gov/ssc/`, accessed 10/07/22

They form showers of secondary particles when they interact with the Earth's atmosphere. Cosmic rays are very abundant and for every gamma-ray that enters the LAT, it will have to filter out $10^5 - 10^6$ cosmic rays . Additionally, these charged particles resemble the particles produced in the conversion foils inside of LAT and so need to be rejected, which is no easy feat [22].

The diagram in Figure 1.3 shows the cross-section of LAT with its four main subsystems. I will now outline the role of each subsystem [96]:

1. **Tracker (TKR):** The tracker consists of four-by four tower modules, each made up of 18 layers of paired, x-y silicon-strip detector planes. Each silicon-strip is interleaved by thin tungsten converter foils. The incoming gamma-ray interacts with the tungsten foil creating electron-positron pairs whose positions are determined by each silicon strip and the trajectory measured. The pair-conversion signature (produced by the electron-positron pair) in the tungsten is unique, and enables the rejection of cosmic ray events which is the dominant background.

2. **Calorimeter:** The Calorimeter is made from caesium iodide and measures the energy deposited by the electron and positron at the bottom of the detector. Caesium iodide is a scintillator and the intensity of the light produced is used to determine the energy of the incoming particles.

3. **Anti-coincidence Detector:** The Anti-coincidence Detector covers the tiles of the detector and is made of a scintillator. This means that photons can pass through it to the conversion foils, but will absorb energy from a charged particle (such as from a cosmic ray) that hits it. The light from the charged particle will trigger the DAQ and enable the event to be distinguished from a gamma-ray photon and reject it.

4. **Data Acquisition System (DAQ):** The Data Acquisition System (DAQ) combines all the electronic signals to trigger on events that are not cosmic rays and reconstruct the gamma-ray photons energy and directionality. Algorithms on board of the *Fermi* satellite filter out gamma-rays originating from the Earth's atmosphere (based on their direction). The DAQ also helps monitor the instrument response and search for gamma-ray bursts within the collected data.

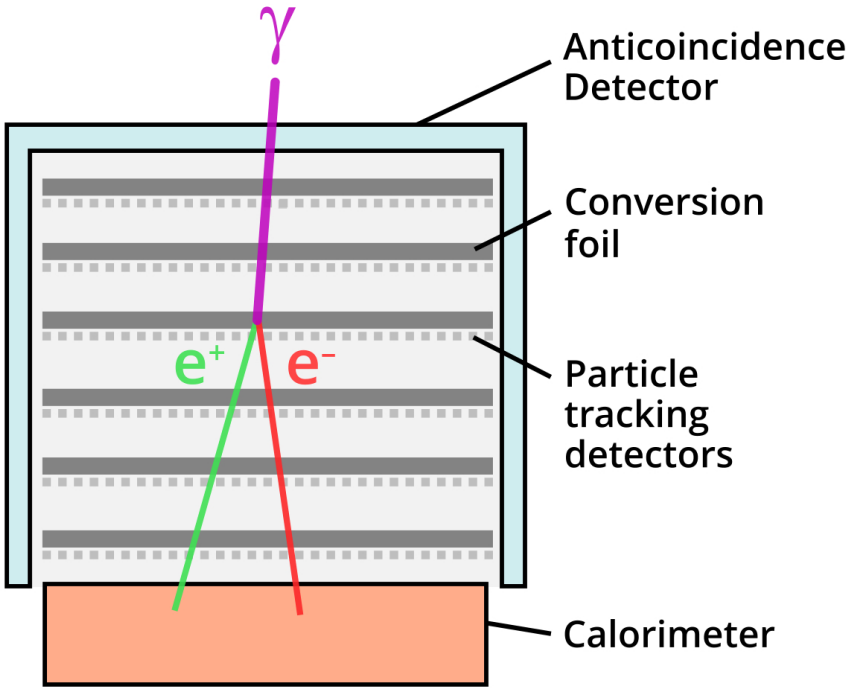

Figure 1.3: Taken from [96]. Diagram showing the cross-section of the LAT. The layers of tracker conversion foils convert an incident gamma-ray photon (shown in purple) into an electron and positron pair. The LAT tracks the trajectory of both particles through the conversion foils, enabling the directionality of the incident photon to be obtained. The electron and positron deposit their energy in the calorimeter, which means that the energy of the incident gamma-ray can also be determined.

1.6 *Fermi*-LAT Event Classes

Every detection of a photon (that has not been rejected as a likely cosmic-ray event) is called a photon 'event'. The energy and directionality of each 'event' is reconstructed and is also given a classification. The classification is determined by the probability that the photon event was actually a gamma-ray and not a background event. The event classes include 'SOURCE', 'CLEAN' and 'ULTRACLEAN', with the 'ULTRACLEAN' class being the purest and least likely to be a background photon [22].

1.7 Instrument Response Functions (IRF)

The sensitivity and performance of *Fermi*-LAT depends on the methods used for event reconstruction and rejecting background photons. These methods are described by the Instrument Response Functions (IRF). The IRF are calibration tools used to combine the detector's effective area, resolution (determined by the Point Spread Function (PSF)) and energy dispersion to characterise its performance for photons of different energies and different incidence angles to the detector. The event selection algorithms are devised using Monte Carlo simulations of a large number of photon events. The results of the simulation are regularly updated to correspond to the changing function of the detector. These updates are called *Passes*, the latest update is *Pass 8*.

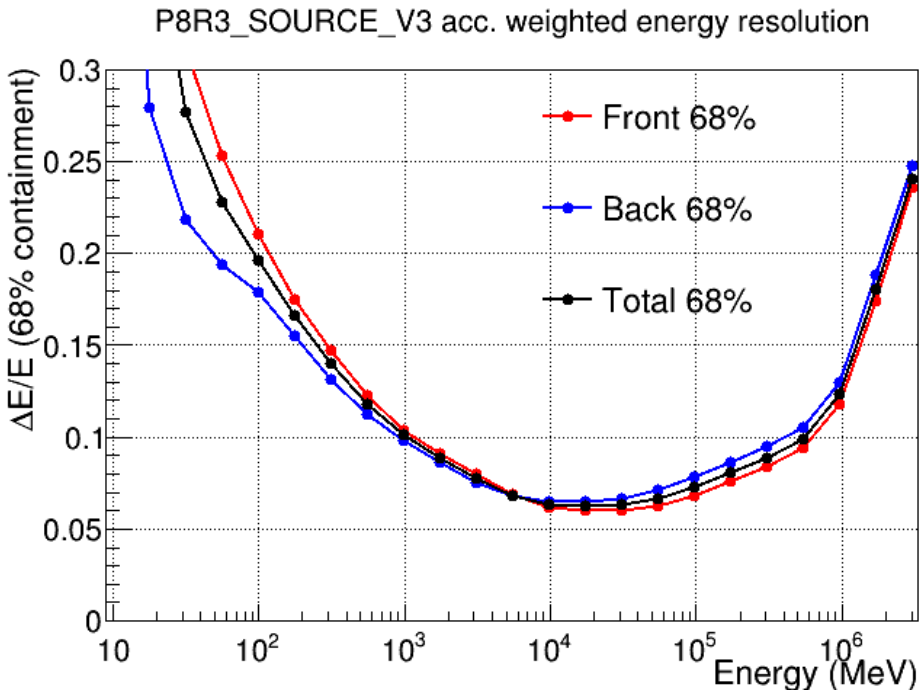

Figure 1.4: Acceptance weighted energy resolution (i.e. 68% containment half width of the reconstructed incoming photon energy) as a function of the photon energy for *Fermi*-LAT. This graph demonstrates how the instrument has poorer energy resolution (cannot determine the exact photon energy as precisely) below 100 MeV and above 1000 GeV. The 'Front' and 'Back' correspond to where the photons are entering the detector. Credit: The *Fermi*-LAT Collaboration. For the latest performance plots see: `https://www.slac.stanford.edu/exp/glas/groups/canda/lat_Performance.htm`, accessed 01/07/22

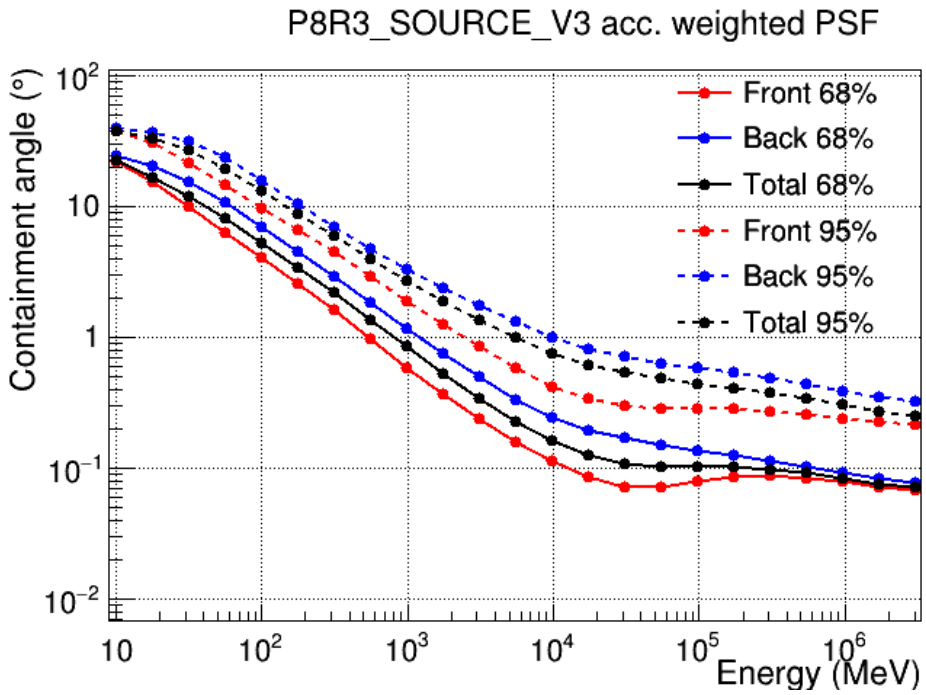

Figure 1.5: The Point Spread Function (PSF) describes the degree to which a point source is spread by the imaging system. It can be used to measure the resolution of an instrument. This plot demonstrates that *Fermi*-LAT has poorer resolution at low energies (it is more difficult to determine whether low energy resolution has originated from the point source or not). Credit: The *Fermi*-LAT Collaboration. for the latest performance plots see `https://www.slac.stanford.edu/exp/glas/groups/canda/lat_Performance.htm`, accessed 01/07/22

1.8 Interesting Scientific Advancements with *Fermi*-LAT

Many exciting discoveries have been made with since *Fermi*-LAT since it was launched. These include:

1. Gamma-ray emission from Pulsars. A significant proportion of Millisecond Pulsars (previously detected by radio telescopes) have been found to also emit at gamma-rays. [8]. Additionally the first pulsar (CTA 1 supernova remnant [7]) was discovered to emit only gamma-rays.

2. *Fermi*-LAT confirmed that supernova remnants act as Cosmic particle accelerators : accelerating charged particles to near relativistic speeds and these charged particles are observed as Cosmic Rays [6].

3. Confirmation that most gamma-ray bursts (GRBs) do not originate from Active Galactic nuclei (AGN) as previously thought[18] .

4. In 2010, *Fermi*-LAT discovered bands of gamma-ray radiation spanning a length of 5×10^4 ly originating from the Galactic centre. This feature is now known as the Fermi Bubbles and is shown in Figure 1.6. The precise origin of this emission is not yet known, however, based on observations of other galaxies one theory is that the Fermi bubbles may originate from the supermassive black hole that has now been confirmed to be at the centre of the galaxy [122].

5. Many objects have been discovered to have associated gamma-ray emission, including Globular clusters. Globular clusters are some of the oldest star clusters known to exist and can be used as probes to better understand galaxy formation. The first globular cluster to be discovered to be emitting gamma-rays was 47 Tuc [4], followed by Terzan 5 [80].

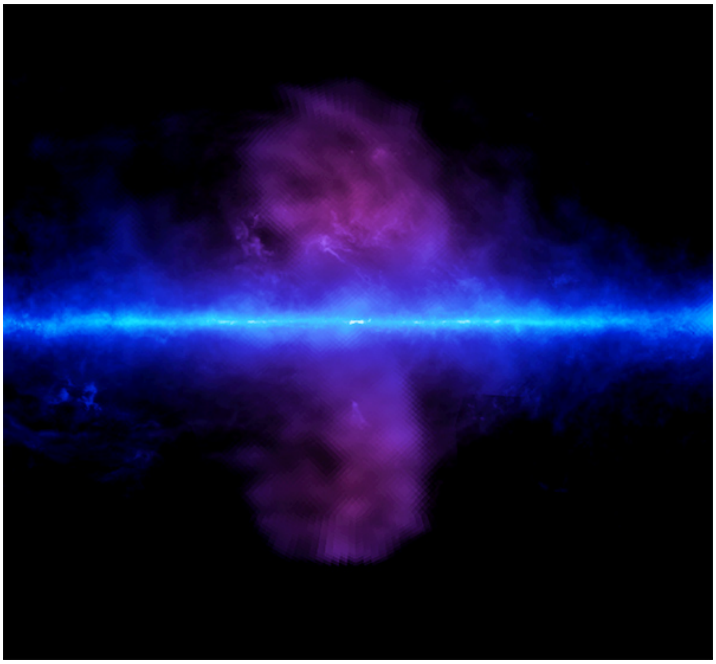

Figure 1.6: Taken from [47]. The Fermi Bubbles are two clouds of gas and cosmic rays which extend 50° above and below the Galactic centre. This image is a false colour image showing the bright gamma-ray emission observed from the Galactic plane (coloured blue) and the Fermi bubbles (coloured purple).

Chapter 2

Objects for Study

2.1 An Introduction to Globular Clusters

Globular Clusters (GC) are gravitationally bound star clusters, approximately spherical in shape. The first GC observed was Messier 22 (NGC 6656) in 1665 [95] and since then, at least 150 GC have been discovered in the Milky Way alone. [118]. GC tend to have masses between $10^4 - 10^6 M_\odot$ and dense cores of around $100 - 1000$ stars per cubic parsec which can be described using the Plummer model [1]. The high stellar density can be inferred from the measurements of the stellar velocity dispersion of particularly bright stars within each GC [104]. GC also have particularly high densities compared to other stellar systems (such as Dwarf galaxies), and (as a direct consequence of the high density) this results in GC having particularly high stellar encounter rates (star collisions) [23]. For this reason, GC contain some exotic classes of stars and an unusually high number of binary systemsthat are not observed in such abundance anywhere else in the Universe. These exotic classes of star include the likes of blue stragglers [29], low mass X-ray binary stars [70] and also an unusually high number of millisecond pulsars (the latter I will discuss in more detail later).

There are two distinct GC populations: the metal-poor GC (containing stars of metallicity around $\frac{1}{300}$ of solar metallicity) which are thought to have been accreted from satellite galaxies and the metal-rich GC (containing stars of metallicity between $\frac{1}{10}$ and $\frac{1}{3}$ of solar metallicity) and there is evidence to suggest that these formed in-situ with the Milky Way and these tend to lie closer to the Galactic Plane [112, 118]. In the Milky Way, the majority of GC are satellites (away from the Galactic centre) [21], the distribution of GC around the Milky Way is shown in Figure 2.1. Additionally, no star formation has been observed in any GC and they tend to have little dust or gas [66]. GC have been observed around the majority of types of galaxies, but their role in galaxy formation is not yet understood.

[1] The Plummer model was first used to fit the observed stellar density profiles $\rho(r)$ within a GC [106]. This is defined as:

$$\rho(r) = \frac{3M_0}{4\pi a^3}\left(1 + \frac{r^2}{a^2}\right)^{\frac{-5}{2}} \tag{2.1}$$

where M_0 is the total mass if the cluster and a is the Plummer radius which is a scale parameter dependant on the size of the GCs core

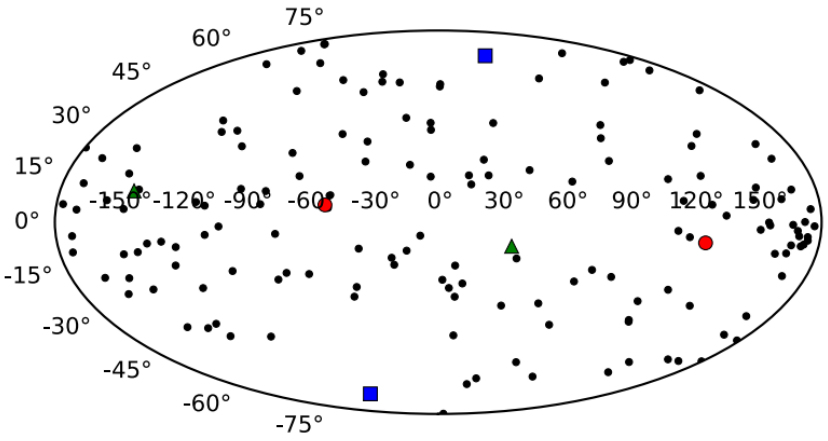

Figure 2.1: Taken from [21]. A sky map, showing the distribution of GCs in the Milky Way (each GC is a black dot). The units are the Galactic coordinates with respect to the Galactic Place (at 0° latitude). The red circles, green triangles and blue squares respectively mark the major, intermediate and minor axii of the Milky Way gyration tensor.

2.1.1 Why are Globular Clusters Interesting to Study?

GC are of great research interest for several reasons. Firstly because of their age (inferred by their metallicity and observed population of old stars): there is evidence that many GC formed at the same time as the Milky Way and are therefore an important probe in understanding galaxy formation [28]. Secondly, observing the composition of GC stellar populations assists in constraining the age of the Universe, and can also increase our understanding on the evolution of binary star systems [118]. GC have also been observed to contain little gas and dust (which is likely why no star formation has been observed either) and means that observations are easier than in other types of star clusters [26]. There is also some evidence to suggest that some GC may contain an intermediate mass black hole (IMBH) at their centre, it is not fully understood how IMBH form however it is thought that the dense cores in GC may favour their creation [79]. It is also thought that some GCs may also have formed within Dark Matter sub-halos and may still contain a component of DM [50]. Also studies of GC proper-motions can enable estimates of Galactic mass as well as the mass and distribution of the hypothesised dark matter halo surrounding the Milky Way [107].

2.1.2 Gamma-rays and Globular Clusters

In 2009, gamma-rays associated with the globular cluster NGC 104 (47 Tuc, shown in Figure 2.2) were detected with *Fermi*-LAT [5]. Since then, *Fermi*-LAT has found statistically significant gamma-ray emission associated with 35 GC, roughly one quarter of all GC within the Milky Way [10]. The gamma-ray emission observed in many GC is thought to originate predominantly from their millisecond pulsar population [30, 10]. This connection was postulated because gamma-rays have been detected from a number of isolated millisecond pulsars with *Fermi*-LAT [9]. The connection between millisecond pulsars and gamma-ray emission from GC has been strengthened by the detection of pulsed gamma-ray emission from three GC [60, 76, 135]. However, for the majority of GC Millisecond pulsars in have only been detected at radio wavelengths and no millisecond

pulsar has been individually resolved in gamma-rays [61, 75] [2].

The lack of direct evidence for gamma-ray emission from MSP in many GC means that it is also possible that there are some other sources of gamma-ray emission in the GC. Some studies such as [39, 40] have found that some GC may have a Dark Matter component that may be responsible for some of the gamma-ray emission: I will explore this later in Chapter 8. Additionally there is some evidence that there is excited gas in GC Terzan 5 to contribute to the emission [102]. Many GC have also contain X-ray binary star systems (which are believed to be a progenitor for millisecond pulsars [70]) and could also contribute to the GC gamma-ray emission.

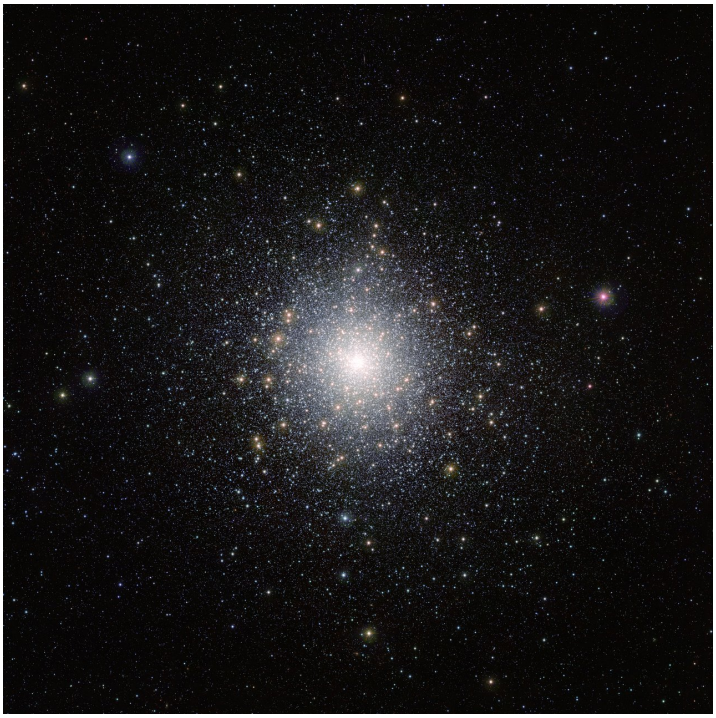

Figure 2.2: Image taken by ESO's VISTA (Visible and Infrared Survey Telescope for Astronomy) from the Paranal Observatory in Chile of 47 Tuc (also referred to as NGC 104) [123].

[2] mainly because *Fermi*-LAT does not have sufficient angular resolution to do this and the millisecond pulsars may not be bright enough

2.1.3 Spectral Shapes of Globular Clusters

GC appear as point sources to *Fermi*-LAT because of their distance and the angular resolution of the instrument. A spectral energy distribution (or SED) shows the energy flux emitted by a source as a function of photon energy. The best-fit spectral shape depends on the sources inside the GC. For example, pulsars have SEDs with a cut-off energy (where the spectrum drops steeply at the cut-off energy). The differential flux $\frac{dN}{dE}$, (the photon flux per energy bin) of detected GC can be described by one of the following models [94]:

1. Log Parabola:
$$\frac{dN}{dE} = N_0 \left(\frac{E}{E_b}\right)^{-(\alpha+\beta\log(\frac{E}{E_b}))} \tag{2.2}$$
where N_0 is the normalisation and is measured in units of $\mathrm{MeV}^{-1}\mathrm{cm}^{-2}\mathrm{s}^{-1}$ and the exponents α and β are dimensionless. E_b is an energy scale parameter measured in MeV.

2. Power Law:
$$\frac{dN}{dE} = N_0 \left(\frac{E}{E_0}\right)^{\gamma} \tag{2.3}$$
where N_0 is the normalisation prefactor and is measured in units of $\mathrm{MeV}^{-1}\mathrm{cm}^{-2}\mathrm{s}^{-1}$. The exponent γ is dimensionless and E_0 is the scale energy measured in MeV.

3. Power Law with an Exponential cut-off:
$$\frac{dN}{dE} = N_0 \left(\frac{E}{E_0}\right)^{\gamma_1} \exp\left(-\frac{E}{E_c}\right)^{b} \tag{2.4}$$
where N_0 is the normalisation prefactor and is measured in units of $\mathrm{MeV}^{-1}\mathrm{cm}^{-2}\mathrm{s}^{-1}$. The exponents γ_1 and γ_2 are dimensionless. E_c is referred to as the cut-off energy (measured in MeV), which is the energy at which the photon flux drops off steeply. This is the typical spectral shape of MSPs, and the typical cut-off energy is around 1 GeV.

2.2 Millisecond Pulsars

2.2.1 Introduction to Pulsars

Pulsars are magnetised neutron stars [3] - that emit beams of radiation out from their magnetic poles. This is shown in a diagram in Figure 2.3. Pulsars are usually observed at radio wavelengths, but also emit electromagnetic radiation at higher energies [126]. Pulsars rotate on short time periods which means that the intensity of the radiation beams detected changes as the position of the beam changes direction relative to the observer - which is why the signal detected is pulsed.

Pulsars were first discovered by Jocelyn Bell in 1967 using a newly built radio telescope and noticing a regular, 'scruffy' pulse in the data that could not be explained by interference [72]. The first pulsar to be observed was the Crab Pulsar, which remains

[3] Neutron stars are formed following the core-collapse of a massive super giant star of mass $10M_\odot - 25M_\odot$ in a Supernova explosion. They are the smallest and most dense stellar object (known) in the Universe

the strongest and brightest pulsar discovered. Pulsars are useful objects to study for a number of reasons:

1. Pulsars have very high densities, exceeding those of atomic nuclei (over 10^{14} gcm^{-3}) and these densities have not been observed anywhere else in the Universe. This makes them unique test beds for testing theories (such as General Relativity) in extreme conditions. Gravitational waves have recently been detected from Pulsars [1].

2. Pulsars also produce some of the highest magnetic fields observed anyway in the Universe which are not reproducible in a physical laboratory [90]

3. Pulsars can be timed very precisely because they spin at a constant rate. This means that they can be used to make sensitive measurements.

Millisecond pulsars (MSP) are pulsars with pulse periods (P) between 0.1 ms and 10 ms [92]. MSP make up a relatively small proportion of the older pulsars, but they are observed in such abundance because they have a long lifetime [90]. There are 489 MSP pulsars that have been observed by the Australia Telescope National Facility Catalogue (ATNF) throughout the Milky Way [4] including a substantial proportion from within GC [90]. It is thought that many of the Galactic MSPs originate from spun-up neutron stars, wound up by accretion of a neighbouring star [90]. There is evidence to suggest that the MSP within GC have evolved from X-ray binary star systems [70, 90].

2.2.2 Millisecond Pulsars in Globular Clusters

MSP have been detected within many GC using radio telescopes [61] [5]. A histogram showing the number of MSPs in each GC is shown in Figure 2.5. Studies have shown that many GC have spectra similar to MSP: MSP spectra have spectral cut-off (a rapid decrease in energy flux) at a few GeV in energy, which is one of the reasons why MSP have been assumed as being the source of GC gamma-emission [81]. It has also been observed that there is a positive correlation between GC gamma-ray luminosity and the expected number of MSP [6], which has been shown to be consistent with the number of observed MSP in other studies [10]. This is shown graphically in Figure 2.4.

However these findings are qualitative comparisons linking GC and MSP gamma-ray emission and cannot explain all the observations. Some GC have spectra that do not show evidence of cut-off (such as NGC 7078 in [88]) which is therefore not consistent with what is expected from MSP. Additionally, MSP have not been detected from all GC that have been detected with *Fermi*-LAT [24] and furthermore, pulsed emission (associated with an MSP) has not been detected from the majority of GC. For these reasons, a more detailed, quantitative spectral comparison is needed, as well as evidence of pulsed emission from GC to determine if MSP are really the source of GC gamma-emission.

[4] `https://www.atnf.csiro.au/research/pulsar/psrcat/` Date accessed: 27/07/22

[5] A catalogue listing all GC with known pulsars and all the pulsars in the can be found here: `http://www.naic.edu/~pfreire/GCpsr.html`. Date accessed: 27/07/22

[6] there is a positive correlation between GC gamma-ray luminosity and the observed stellar encounter rate (which is presumed to encourage MSP formation from the evolution of low mass X-ray binary stars [70])

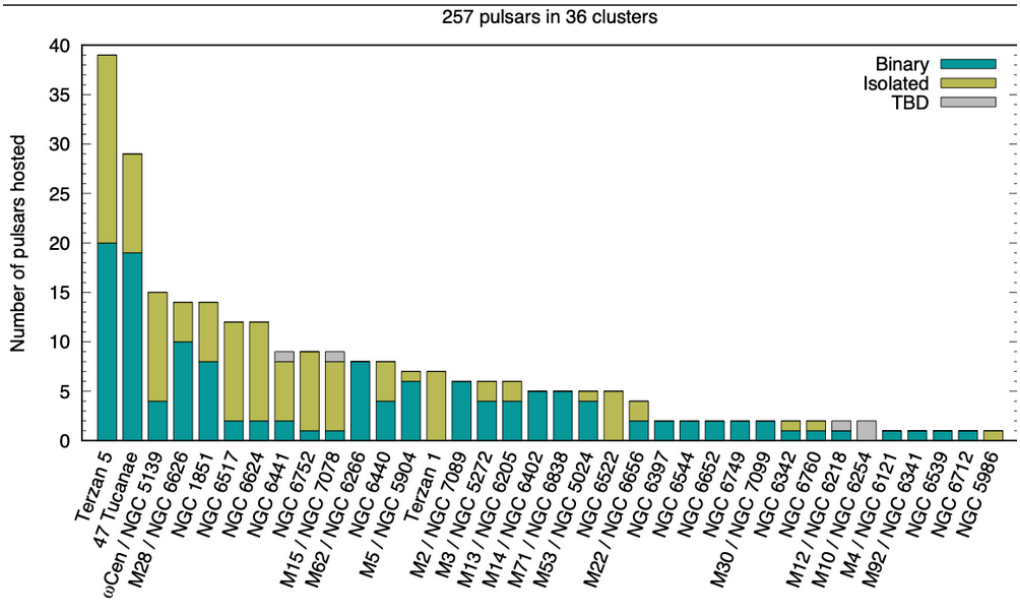

Figure 2.5: Taken from [46]. A histogram showing the number of MSP detected in different GC. These MSP have all been initially detected using radio telescopes. Some of the pulsars are within binary systems (shown in blue) and some are isolated pulsars (shown in green).

2.2.3 Mechanism for Gamma-ray Emission in MSPs

The most commonly accepted mechanism of the origin of the gamma-ray emission from MSPs is from electron/positron (e^-e^+) pair production cascades in the magnetosphere and from curvature radiation. Curvature radiation is produced when charged particles (moving relativistically) move along the curved magnetic field lines and e^-e^+ pair production cascades in the magnetosphere [2]. It is thought that the gamma-ray emission is produced in the same region of the magnetosphere as the radio beam because of their similar pulse profiles observed [90].

2.2.4 Spectral Shape of MSPs

Studies of MSPs in the local Galactic neighbourhood have demonstrated that they all have very similar spectral shapes. This spectral shape is described as a power law with exponential cut-off. Studies of MSPs detected in the local Galactic neighbourhood detected by *Fermi*-LAT have produced models for the expected spectrum for an ensemble of MSPs. One of these studies used the 39 MSP listed in the second gamma-ray pulsar catalogue for *Fermi*-LAT [9] over a 7.5 year observation period to produce a stacked emission spectrum, shown in Figure 2.6. This particular study found that the best fit spectral shape was a power law with exponential cut-off with the following parameters [134]:

$$\frac{dN}{dE} = \left(\frac{E}{10\,\mathrm{GeV}}\right)^{-1.54} e^{-\frac{E}{3.7\,\mathrm{GeV}}} \tag{2.5}$$

From now on, I will refer to this spectrum as the Xing+Wang spectrum.

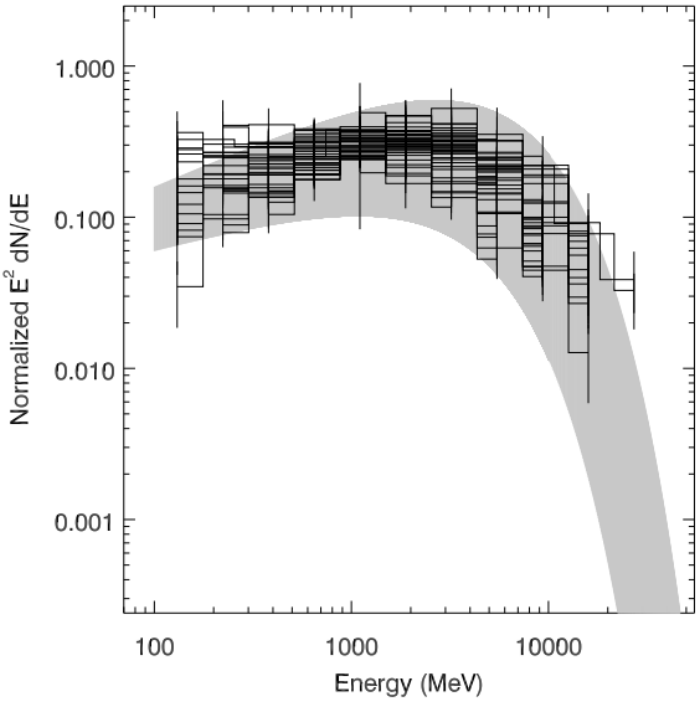

Figure 2.6: Taken from [134]. The normalised spectra of 39 MSP taken from the second *Fermi*-LAT pulsar catalogue [9]. The uncertainties for each MSP combines the statistical and systematic uncertainty (the systematic uncertainty originates from the Galactic diffuse emission model used). The shaded grey band indicates the 3σ region of the best-fit spectral model. The best fit spectral model is a power law with exponential cut-off (see equation 2.4).

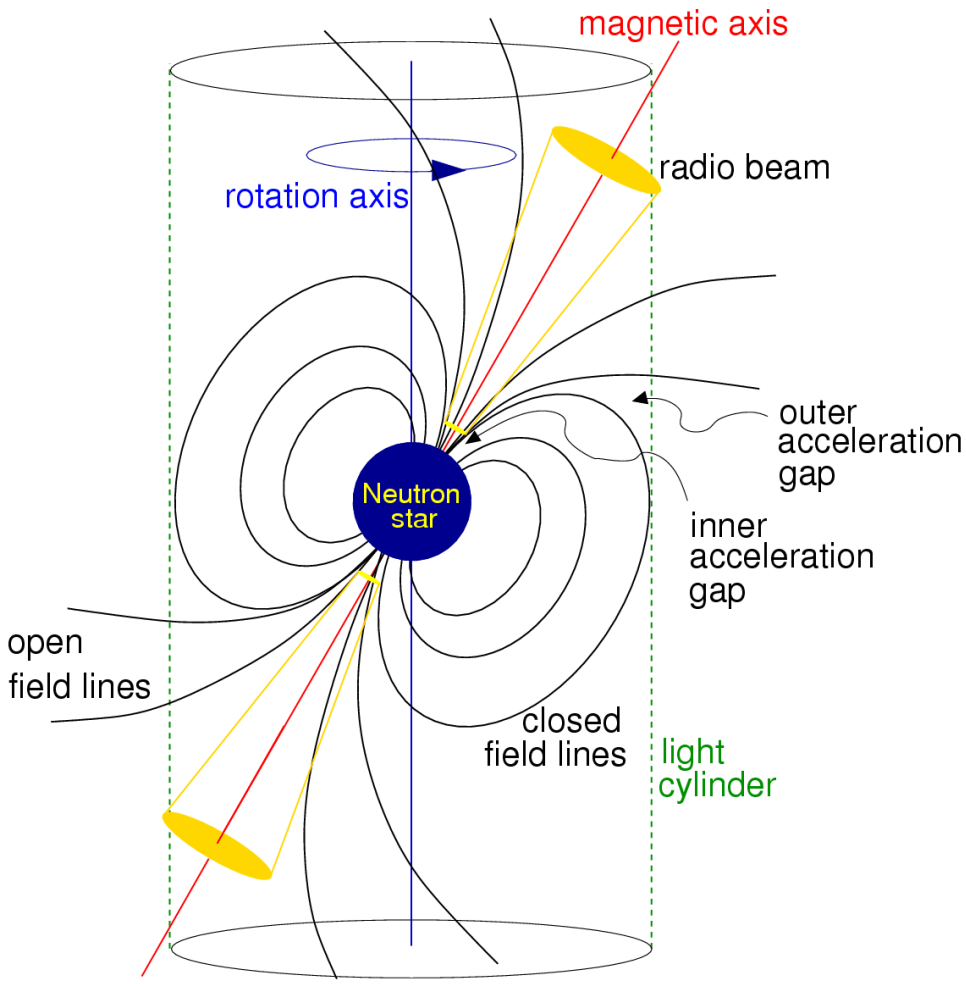

Figure 2.3: Figure showing the pulsar magnetic dipole model. Electrons and positrons originating from particle cascades are accelerated in the "gap" regions of the magnetosphere. The particles follow trajectories along the open magnetic field lines (shown in black) emitting coherent radio waves. In the highest-energy pulsars (such as millisecond pulsars) X-rays and gamma-rays are also emitted. Figure credit: `https://www.cv.nrao.edu/~sransom/web/Ch6.html`. Date accessed: 30/06/2022

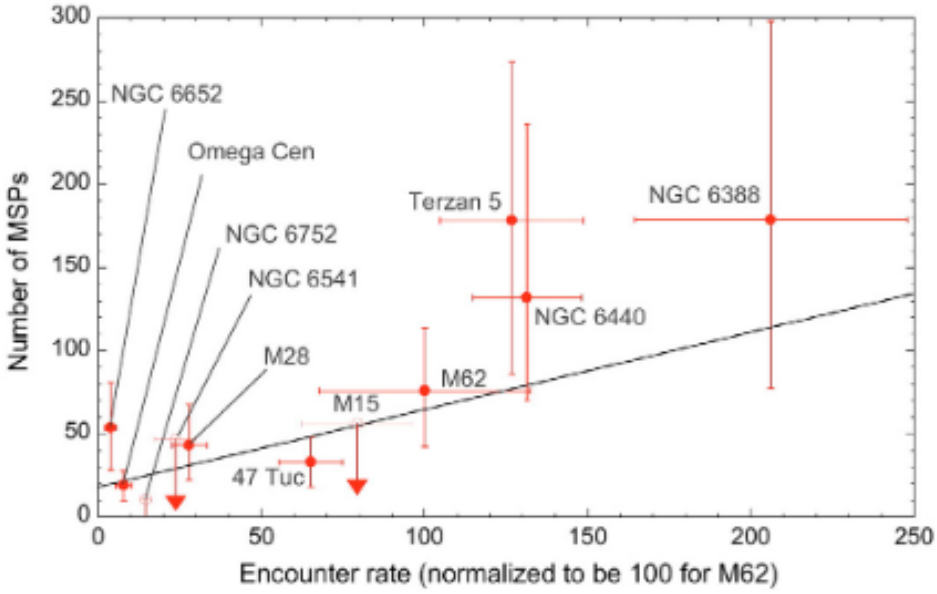

Figure 2.4: Taken from [10]. Graph showing the correlation between the predicted number of MSPs in each GC and the stellar encounter rate. The number of MSPs is estimated from the GC gamma-ray luminosity and the stellar encounter is estimated from the observed stellar density and velocity dispersion. The horizontal error bars indicate the uncertainties in encounter rate due to the distance uncertainties which have been estimated from the spread of values quoted in the recent literature.

Chapter 3

Selection of Globular Clusters for Study

In this chapter I will discuss how I selected the GC to study. I decided to chose six GC to analyse. I made my selection from the GC in the *Fermi* 4FGL-DR2 catalogue [24]: these are the GC that *Fermi*-LAT have detected as having gamma-ray emission with a Test Statistic (TS) larger than 25, which corresponds to being detected at least a 4σ significance [24]. The TS is a measure of how likely the gamma-ray emission originated from the object of interest.

3.1 Selection Criteria

I chose GC after considering the following criteria:

1. GC with the highest detection significance (TS), which means that gamma-ray emission is most statistically likely to be coming from the GC, and not another nearby source.

2. GC with the highest energy flux, because they are brighter and have therefore emitted more photons. More photons means better photon statistics.

3. GC that have MSP detected inside of them and have ideally been studied several times in different wavelengths (often radio and X-ray). This means that it is easier to produce an accurate ephemerides of each MSP. [1]

4. The MSP have been studied sufficiently so that there is a full timing solution available (this is called an ephemeris and I will discuss this in more detail in Chapter 4.6).

5. GC that are not too far away, because the Radio ephemerides (for the MSP) are likely to be better. The precision of Radio wavelength measurements decreases with distance due to dispersion caused by gas in the interstellar medium.

6. Ideally GC with a high Galactic latitude/longitude. I consider a high Galactic latitude/longitude to be $|b| > 15^\circ$ from the Galactic plane. This means that

[1] MSP catalogue used is the NAIC catalog: `http://www.naic.edu/~pfreire/GCpsr.html`, accessed 30/06/22 .

background gamma-emission from the Galactic centre will be smaller and therefore easier to remove during my analysis.

3.1.1 List of GC Detected with *Fermi*-LAT

The *Fermi* 4FGL-DR2 catalogue [24] is a summary of the LAT results covering the time period August 4 2008, to August 2 2018 and is available online and is open-access [2]. 3.1 lists all the GC detected by *Fermi*-LAT in order of decreasing 'TS'. Each source has a '4FGL' Name which is based on its Julian coordinates. The $\sqrt{TS}$ column is the source detection significance in Gaussian sigma units between 100 MeV to 1 TeV. The Galactic latitude (lii) and longitude (bii) are measured in J2000 coordinates that are fitted by *Fermi*. The energy flux is the integrated energy flux between 100 MeV to 100 GeV obtained by spectral fitting. The photon flux is the integrated photon flux for 1 GeV - 100 GeV in units of photons $cm^{-2}s^{-1}$ and is a measure of the brightness of the GC.

The *Fermi* collaboration assigns a spectral shape based on the source's observed curvature following a quick analysis: based on whether the spectrum shows statistically significant curvature. A more detailed analysis is required to confirm the spectral shape. In Table 3.1 the GC all have a Log Parabola model (equation 2.2), apart from NGC 1904, NGC 362 and NGC 5286 which have been found to exhibit a Power Law model (equation 2.3)). Many GC have been observed in multiple wavebands and the 'Other Name' column indicates the most common other name for each GC.

[2] `https://fermi.gsfc.nasa.gov/ssc/data/access/lat/10yr_catalog/`

Name (4FGL)	Alternative Name	$\sqrt{TS}$ (σ)	lii (°)	bii (°)	Photon flux ($\times 10^{-10}$) ($cm^{-2}s^{-1}$)	Energy flux ($\times 10^{-6}$) ($MeVcm^{-2}s^{-1}$)
J0024.0-7204	47 Tuc	99	305.90	-44.89	45.5 ± 1.0	16.9 ± 0.4
J1748.0-2446	Terzan 5	68	3.85	1.69	126.8 ± 2.8	48.7 ± 1.9
J1701.2-3006	M 62	40	353.58	7.32	32.0 ± 1.2	12.5 ± 0.7
J1736.2-4443	NGC 6388	38	345.56	-6.73	29.2 ± 1.1	11.7 ± 0.7
J1326.6-4729	Omega Cen	28	309.08	14.96	20.26 ± 1.0	6.7 ± 0.4
J1750.3-3702	NGC 6441	25	353.55	-5.02	20.4 ± 1.1	10.1 ± 0.9
J1848.7-0129	GLIMPSE C01	20	31.3	-0.1	71.7 ± 6.7	22.3 ± 3.4
J1716.7-2808	NGC 6316	19	357.18	5.74	16.6 ± 1.1	6.4 ± 0.7
J1748.9-2021	NGC 6440	18	7.74	3.79	19.8 ± 1.4	9.2 ± 1.2
J1910.8-6001	NGC 6752	18	336.45	-25.64	6.5 ± 0.5	2.2 ± 0.2
J1835.7-3258	NGC 6652	14	1.55	-11.37	7.2 ± 0.7	3.3 ± 0.5
J0912.1-6449	NGC 2808	13	282.17	-11.22	4.7 ± 0.5	2.5 ± 0.4
J1616.9-2257	M 80	12	352.68	19.49	6.5 ± 0.7	2.7 ± 0.5
J1807.8-4340	NGC 6541	12	349.31	-11.14	6.0 ± 0.7	2.3 ± 0.4
J1735.7-3026	Terzan 1	11	357.59	1.02	17.2 ± 1.9	4.8 ± 0.5
J2129.9+1208	NGC 7078	11	64.99	-27.32	3.2 ± 0.5	2.4 ± 0.4
J1855.1-2243	NGC 6717	10	12.86	-10.91	5.7 ± 0.7	2 ± 0.4
J1818.5-1656	GLIMPSE C02	10	14.17	-0.65	27.8 ± 3.2	10.1 ± 2.5
J1727.6-3050	Terzan 2	9	356.3	2.26	11.6 ± 1.4	5.8 ± 1.6
J1627.6-3852	NGC 6139	9	342.34	6.92	6.5 ± 0.8	3.1 ± 0.7
J1716.8+4310	NGC 6341	9	68.38	34.92	2.3 ± 0.4	0.9 ± 0.2
J1737.5-0313	NGC 6402	8	21.34	14.83	5.6 ± 0.8	2.0 ± 0.4
J1953.6+1846	NGC 6838	8	56.73	-4.54	4.3 ± 0.6	2.6 ± 0.6
J1714.2-2928	NGC 6304	7	355.78	5.41	5.5 ± 0.9	2.6 ± 0.8
J0513.9-4005	NGC 1851	7	244.57	-35.07	1.7 ± 0.3	0.9 ± 0.3
J1647.2-0154	NGC 6218	7	15.75	26.33	2.2 ± 0.5	0.8 ± 0.1
J1518.8+0203	NGC 5904	7	3.89	46.73	2.4 ± 0.4	1.0 ± 0.3
J1741.1-5341	NGC 6397	6	338.19	-12.02	3.0 ± 0.5	1.8 ± 0.5
J0524.4-2413	NGC 1904	6	226.92	-29.2	1.3 ± 0.3	1.7 ± 0.3
J0102.9-7051	NGC 362	5	301.57	-46.23	1.3 ± 0.3	0.9 ± 0.2
J1853.2-0841	NGC 6712	5	25.39	-4.35	4.5 ± 0.8	1.9 ± 0.6
J1346.1-5121	NGC 5286	5	311.57	10.59	2.1 ± 0.4	1.7 ± 0.4
J1808.8-1949c	2MS-GC01	5	10.53	0	21.4 ± 4.0	12.7 ± 4.9
J1855.1-3025	M 54	5	5.67	-14.09	2.5 ± 0.6	0.9 ± 0.3
J1641.6+3622	M 13	4	58.9	40.91	1.2 ± 0.3	0.3 ± 0.1

Table 3.1: Table of GC detected with *Fermi*-LAT from the 4FGL DR2 catalogue [24]. The GC have been ordered in descending detection significance ($\sqrt{TS}$), measured in Gaussian units of σ).

3.2 Final Selection of GC

The final selection was made using Table 3.1 and NAIC pulsars in globular clusters catalogue (see Figure 2.5). It was not possible to meet all the selection criteria for each GC. I choose each object by balancing the brightness, location and the number of MSPs. The final six GC I have selected for study are listed below:

1. ω Centauri: Which I have chosen because of its position (a high Galactic latitude and longitude) . It is also bright and has been detected with high significance (28σ).

2. 47 Tuc: Which I have again chosen because of its position, high energy flux (the second brightest GC detected with *Fermi*-LAT) and high significance. A disadvantage of analysing this GC is that it contains a lot of MSPs which could make picking out individual pulsars more challenging.

3. NGC 7078: This GC has a lower energy and photon flux compared to 47 Tuc and ω Centauri. Nevertheless, it has been detected with high significance (11σ) and also contains a manageable number of MSPs (which may make it easier to resolve individual MSP in gamma-rays). This GC is also interesting because it has been observed as having a PL spectral shape instead of a LP.

4. NGC 6752: This GC has been detected with high significance, is bright, and has a high Galactic latitude and longitude. There are 10 known MSP within this GC, which is a manageable number.

5. NGC 6441: I have chosen NGC 6441 because despite it being close to the Galactic plane it is bright (with a similar energy flux to ω Centauri), and has been detected with high significance.

6. Terzan 5: I have chosen Terzan 5 because despite being close to the Galactic plane, it is the brightest GC detected with *Fermi*-LAT and has the second highest detection significance. It also has the largest number of MSPs of any GC in [24], even though none of these MSPs have been individually detected in gamma-rays.

Chapter 4

Pulsar Timing and Measurement

4.1 Motivation for Timing Pulsars

There are many rotating astrophysical objects whose rotation period and orbit can be determined with great accuracy and precision. Indeed, the Earth's rotation is used as a clock, accurate to one part in 10^8 per day [90]. Outside of the Solar System, studying the pulse arrival times from pulsars using measurements taken with radio telescopes can be used as accurate clocks. Pulsars can also be used to accurately determine the position of a source (for example, the measurements of emission from a MSP in a GC can be used to verify its distance and position) and also to determine how the composition of the interstellar medium between the observer and pulsar by measuring the dispersion of the pulse [53].

4.2 Measuring Pulsar Arrival Times

4.2.1 Timing Correction

The arrival time of an individual pulse (relative to the time it was emitted by the pulsar) depends on the radio frequency due to dispersion as the pulse travels through ionised gas of the interstellar medium between the observer and the pulsar.

Various corrections need to be made to the arrival time of a photon in order to relate it to the time of emission from the pulsar. The arrival time of an individual pulse at the observatory, $t_{\rm obs}$ is related to the emission, $t_{\rm e}$, time by

$$t_{\rm obs} = t_{\rm e} - (\Delta_\nu + \Delta_{R\oplus} + \Delta_{E\oplus} + \Delta_{S\oplus}) \tag{4.1}$$

Where Δ_ν is the correction due to dispersion as the pulse travels through ionised gas of the interstellar medium between the observer and the pulsar. This depends on the radio frequency (ν) of the pulse [1] and the distance it has travelled.

$\Delta_{R\oplus}$ (known as the Römer correction) is the correction to the reference frame of the Solar system barycentre [2] The final two terms $\Delta_{E\oplus}$ and $\Delta_{S\oplus}$ are corrections due

[1] $\Delta_\nu \propto \frac{1}{\nu^2}$

[2] The barycentre is the centre of mass of the entire solar system. The position of the barycentre

to the effects of General Relativity. $\Delta_{E\oplus}$ is the Einstein delay caused by Gravitational red-shift and time dilation. $\Delta_{S\oplus}$ is known as the Shapiro delay which accounts for the fact that the radiation passes through curved space-time, most noticeably close to the Sun and when the Sun is in the line of sight of the pulsar [90].

4.2.2 Determining the Pulse Profile

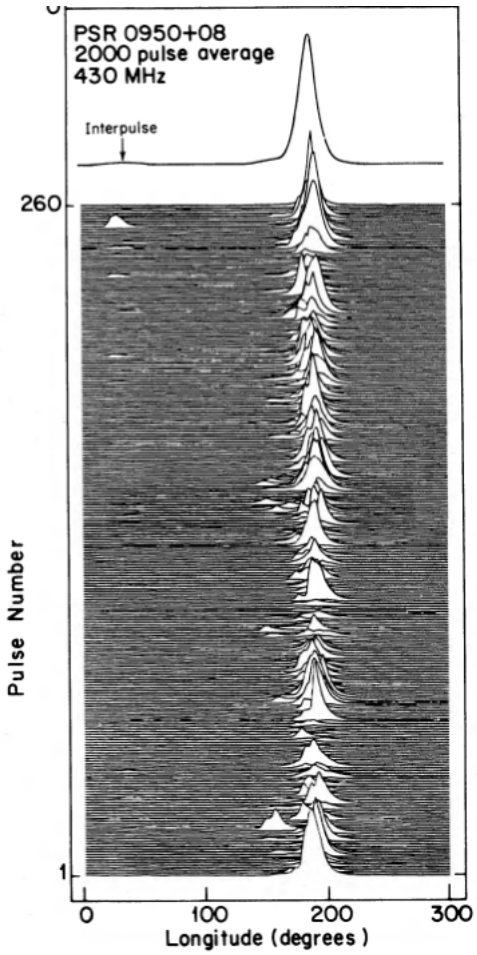

Figure 4.1: A sequence of radio pulses observed from PSR B0950+08. The integrated profile is obtained by summing these individual pulses [69].

Figure 4.1 demonstrates that individual radio pulses from any given pulsar will vary greatly in their intensity and shape. This variation occurs because pulsar emission is intrinsically a noise process (and we only observe pulsed emission due to the relative rotation between the observer and Radio beam as shown in 2.3). By measuring hundreds (or even thousands) of individual pulses over a short time interval allows observers at the Radio observatory to produce an integrated profile (with a unique shape, pulse width and frequency) for the pulsar. For MSPs, this standard profile is very reproducible and varies very little. A time-averaged profile enables high-precision timing [119]. The process of summing individual pulses is often referred to as Phase folding [3] When multiple pulses

constantly changes from being near the centre of the Sun to being outside the surface of the Sun. The position changes due to the movement and orbit of each planet and therefore needs to be corrected for.

[3]pulses are added (with the timing corrections described in Section 4.2.1 so that the signal is visible above the background noise.

are superposed, you have to account for the timing corrections described in Section 4.2.1. The individual pulse length varies due to the relative motion of the Earth and the Sun (due to the Doppler effect), and an observer on Earth will notice that the observed times of arrival will vary sinusoidally with an annual period. This Doppler effect will need to be corrected for as well. Radio ephemerides are the complete timing solution produced for a pulsar following many observations using a radio telescope. When examining the average (folded) pulse profile it is useful to consider the pulse period P and the instantaneous pulse phase ϕ.

The average pulse period P is given as:

$$P = \frac{1}{f} \tag{4.2}$$

where f is the average frequency of pulsation. The instantaneous pulse phase ϕ is defined as:

$$\phi = \int_0^{2\pi} f dt \tag{4.3}$$

where

$$0 \leq \phi \leq 1 \tag{4.4}$$

4.3 Determining Ephemeris Validity

It is only possible to analyse pulsars that hold their phase over the time in which you are analysing. As the variation in the rotation period of a pulsar is small, the phase ϕ can be written as a Taylor expansion about the time t_0 where the pulsar was measured:

$$\phi(t) = \phi(t_0) + f(t - t_0) + \frac{1}{2}\frac{df}{dt}(t - t_0)^2 + ... \tag{4.5}$$

where t is the time at which the pulsar is being observed. The main errors are due to the measurement uncertainty in the phase compared to the current time. The error on the phase due to the uncertainty in the Period P measurement is shown in equation 4.6

$$\Delta\phi = \frac{\Delta t \Delta P}{P^2} \tag{4.6}$$

the error on the phase due to the uncertainty in the period derivative, $\frac{dP}{dt}$, measurement is:

$$\Delta\phi = \frac{t^2 \frac{dP}{dt}}{2P^2} \tag{4.7}$$

the pulsars need to have errors of no more than 20% in order to phase fold and produce valid results [90].

4.4 Phase-folding Gamma-ray Data

4.4.1 TEMPO2

TEMPO2 is a software package used for the analysis of pulsar pulse times of arrival (often referred for as TOAs). The method of timing Pulsars involves measuring the

pulse TOAs at the observatory and then fitting these TOAs to a model. The model then relates the measured TOA to the time of emission at the pulsar, and TEMPO2 aims to measure with a precision and accuracy of up to 1 ns [73].

The *Fermi* plug-in for TEMPO2 enables the calculation of a pulsar's rotational phase for each photon arrival time in a *Fermi*-LAT photon event file.

The plug-in calculates the position of the observatory for each photon (contained in a photon 'event' file). [4] By using the time-dependent *Fermi*-LAT coordinates (contained in the spacecraft photon file which can be downloaded from the Fermi Science Support center) the plugin then converts the topocentric coordinates (measured from the surface of the Earth i.e at the Radio observatory) to barycentric dates (defined using Galactic latitude and longitude) and calculates the pulse phases using the barycentric dates [5][110].

Timing Solution for Pulsar used by TEMPO2

TEMPO2 requires a timing solution for the pulsar in order to phase fold the gamma-ray data from *Fermi*-LAT. This is known as an ephemeris and is produced from Radio measurements.

```
1  PSRJ         J1326-4728B
2  RAJ          13:26:49.563(6)
3  DECJ         -47:29:24.62(2)
4  F0           208.686833122(5)
5  F1           -1.2(4)e-15
6  PEPOCH       58768.0
7  DM            100.2733
8  START         58444.95
9  FINISH        58798.08
10 TZRSITE         7
11 TZRMJD         58643.30
12 TZRFRQ         208.33
```

Figure 4.2: An example of a pulsar ephemeris used in the format required by `TEMPO2`.

Figure 4.2 shows an example ephemerides file (in the *par* format required by TEMPO2), this is quite a simple ephemeris and in reality they can be more complex. An ephemeris must contain at least the following parameters:

1. PSRJ: Pulsar Julian Name
2. DM : Dispersion Measure, which is the "integrated column density of free electrons between an observer and a pulsar" and causes the sharp pulse emitted to appear broadened when a pulsar is observed over a finite bandwidth [118].
3. RAJ: J2000 Right Ascension of pulsar (hh:mm:ss.sss)
4. DECJ: J2000 Declination of pulsar (dd:mm:ss.sss)
5. P0 or F0: Pulse Period (s), or Frequency (Hz)
6. P1 or F1: Pulse Period (or frequency) derivative ($\frac{dP_0}{dt}$ or ($\frac{dF_0}{dt}$))
7. PEPOCH: Epoch when pulsar period (P0) was determined (MJD [6])

[4] using the same interpolation algorithm as implemented in the Fermi Science Tools `gtbary` and `gtpphase`. I have chosen TEMPO2 over using the *fermitools* because TEMPO2 is known to be more accurate with pulsars with more complex ephemerides and over larger-time periods.

[5] See `https://fermi.gsfc.nasa.gov/ssc/data/analysis/user/Fermi_plug_doc.pdf` for full documentation on TEMPO2 fermi plugin. Date accessed: 04/07/22.

[6] Modified Julian Date `https://core2.gsfc.nasa.gov/time/` accessed: 13/08/22

8. TZRSITE: Location code of radio observatory

9. TZRMJD: a reference time of arrival (MJD) calculated as the first site arrival time (at the radio telescope) with an MJD greater than the PEPOCH that produces zero residual

10. TZRFREQ: The frequency (Hz) of the arrival time corresponding to TZRMJD

These parameters can be found in the discovery or observation papers for each pulsar, or alternatively may already be in the *Fermi* gamma-ray pulsar catalogue if they have already been observed in gamma-rays.

Output File of TEMPO2

For short time intervals, TEMPO2 provides plots (shown in Figure 4.3) of the H-test value over time, a phase folded light curve over two periods (with 1σ error bars) and the number of photons detected at each time of each phase.

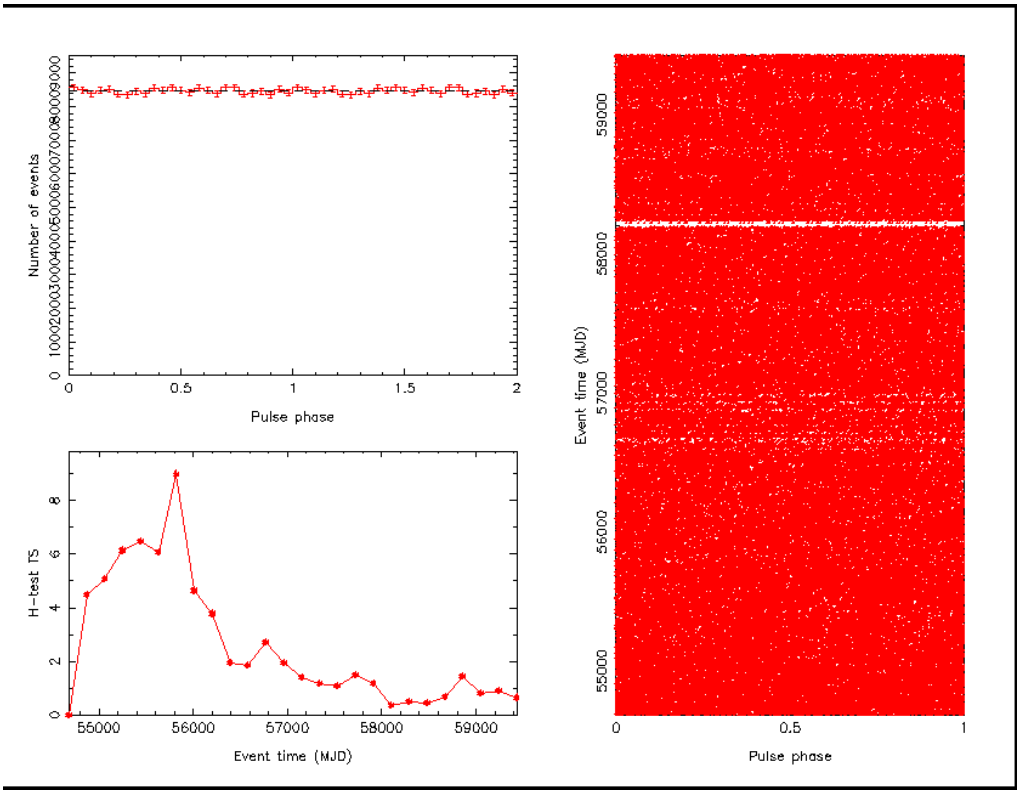

Figure 4.3: Shows a short time period for MSP in NGC 6624. Plot on top left is phase folded photons over two phase cycles. Bottom left is the H-test statistic over time. Right is the pulse phase and number of photons detected. The white band corresponds to the time interval when *Fermi*-LAT was not in operation for a short period in 2009.

4.5 Testing for Pulsed Emission

Once the gamma-ray data has been phase folded, there are many different ways of determining whether pulsed emission has been observed or not. In this section I am going to outline several approaches to statistically determine whether pulsed emission has been detected from a Pulsar.

4.5.1 Method 1 - Chi-square Test

The Chi-square (χ^2) test-statistic can be used to test the assumption of a null hypothesis (H_0), that there is no association between the pulse phase and number of counts in each bin (i.e the light curve is statistically 'flat') against an alternative hypothesis (H_1) that there is evidence for a association between the phase and counts per bin. Evidence for H_1 could be evidence for pulsed emission. The χ^2 test statistic is defined as:

$$\chi^2 = \sum_{i=1}^{N} \frac{(O_i - Ei)^2}{E_i} \tag{4.8}$$

where O_i and E_i are the observed and expected number of photons in bin i. The expected number of counts E_i assuming that there are equal photons in each bin (i.e the phase profile is flat). This method is advantageous in that it makes no assumption about the shape of the light-curve: the precise position of any many pulses (and inter-pulse) and their relative intensity is often not the same in different wavebands. A disadvantage of this method is that the result is dependent on the number of bins (N) chosen. There are many possible valid approaches to choosing the binning. A first approach would be to look at the width of the main pulse in the radio pulse profile, and choose the binning from that. Another disadvantage is that χ^2 test statistic can only determine whether data is statistically 'flat' or not. The χ^2 test statistic may indicate that the pulse profile is not flat, but this does not mean that there is one-two main pulses that would show the pulsed emission you would expect from a pulsar.

4.5.2 Method 2 - H-Test

Another method is known as the statistical H-test. The H-test was initially derived to test for periodicity in gamma-ray emission [54] in order to improve the sensitivity to periodic signals from gamma-ray telescopes, which all have problems distinguishing specific signals and removing background contamination. There are different ways to implement the H-test, depending on the type of objects you are looking at. The H-test was revised specifically for searching for weak, pulsed emission in *Fermi*-LAT [77] to include photon weights in order to pick out weaker pulsed signals more effectively.

The mathematical definition of the weighted H-test statistic is defined as:

$$H_{mw} = \max[{Z^2}_{iw} - c(i-1)], 1 \leq i \leq m \tag{4.9}$$

where Z is the weighted Z-statistic, which is calculated in a summation over the N photons observed:

$${Z^2}_{nw} = \frac{1}{\sum_{i=1}^{N} w_i^2} \sum_{k=1}^{n} (\alpha_{wk}^2 + \beta_{wk}^2) \tag{4.10}$$

α_{wk} (equation 4.11) and (equation β_{wk} 4.12) are the coefficients that describe the periodicity of the flux of the pulsar.

$$\alpha = \sum_{i=1}^{N} \alpha_i \cos(\omega_i \phi) \tag{4.11}$$

$$\beta = \sum_{i=1}^{N} \beta_i \sin(\omega_i \phi) \tag{4.12}$$

The optimal weighting (for each photon) w_i to detect a pulsation is to weight each photon with the probability it originated from a specific pulsar. As most pulsars in GC cannot be observed individually by *Fermi*-LAT (as the angular resolution is not sufficient), we can weight photons according to the probability they originated from the globular cluster. The probabilities are computed using the *Fermi*-LAT instrument response function (which is dependant on photon reconstructed energy, position in the sky and time-averaged arrival time of each photon), and the a full spectral model (which is optimised in the `FERMIPY` analysis). It has been shown that the H-test can increase the sensitivity to pulsars by over %, and this percentage is likely to be higher for Millisecond pulsars, which we are trying to detect. This weighting can be implemented by using the *gtsrcprob* tool in *fermitools*, or alternatively using the *compute_srcprob* in `FERMIPY` [132].

4.5.3 Method 3 - Photon Weights

There are some disadvantages if using the *gtsrcprob* weighting outlined above. The first is that a high test significance is needed in order to make the weights meaningful. I have selected GC with a high TS so this in itself is not a problem, but it does however mean that any faint pulsations from MSP in the GC could be difficult to detect, particularly in GC with many MSP and consequently the emission is messy. Secondly, *gtsrcprob* requires the diffuse response of all extended sources in the ROI (computed using *gtdiffrsp* tool in the FSSC *fermitools*) which is very computationally intensive when analysing 13 years of data, and using a large Radius Of Interest (ROI) around the GC of 15° (which I will discuss more in Chapter 5).

A simpler method that does not have either of these disadvantages using the H-test with a different, simpler weighting. This was derived by Bruel (2019) [41]. The photon weights w depend on the energy E, and angular position $\Delta\theta$ they are detected from within the ROI. The weights $w(E, \Delta\theta)$ are defined as:

$$w(E, \Delta\theta) = g(E, \Delta\theta) \exp(2 \log^2 (E/E_{ref})), \tag{4.13}$$

where $g(E, \Delta\theta)$ is

$$g(E, \Delta\theta) = \left(1 + \frac{9(\Delta\theta)^2}{4\sigma^2 (E)}\right)^{-2} \tag{4.14}$$

which is known as the Moffat distribution and describes how gamma-ray photons are emitted from a point-like source. E_{ref} is the energy at which pulsar's weight distribution peaks. It is found that the distribution between pulsar weights $w(E, \Delta\theta)$ and $\log E$ (with E being the photon energy)is independent of the pulsar's precise spectral shape and can be described as a Gaussian function with width of 0.5. Using this method, it is possible to scan through a photon file that has phases assigned using TEMPO2. The energy at which the H-test is maximised can be found by iterating over the energy range in the event file. This method not only indicates the energy range with maximum pulsation, but also shows whether there is statistical evidence for pulsation.

4.6 Methods Chosen

I trialled each of the statistical tests outlined above for my analysis in order to compare the results. The Chi-squared test indicated that the light-curve was not flat for the majority of the pulsars (which I analyse in Chapter 7), but this does not mean that there is evidence of a main pulse or an inter-pulse that is expected (based on the radio pulse profile). I also observed that the shape of the light-curve changes greatly through the choice of binning. For these reasons I have decided that the Chi-square test is not sufficient to determine whether there is evidence of pulsed emission. I will test for pulsed emission using a combination of the H-test (Method 2) and also using photon weights (Method 3). By doing two independent analyses for pulsed emission will allow me to compare the results from each.

Chapter 5

Fermi Analysis of NGC 6624

NGC 6624 is not one of the GC I selected in Chapter 2.2.4, however previous studies with *Fermi*-LAT have detected pulsed emission from the GC [60]. In this chapter I am going to carry out a detailed spectral analysis of the GC NGC 6624 using 13 years of *Fermi*-LAT data, and then I will use the methods outlined in Chapter 3.2 to see if I can detect pulsed emission over 13 years.

5.1 Previous Studies of NGC 6624

The GC NGC 6624 was first detected in gamma-rays with the *Fermi*-LAT in 2008 [60]. In the *Fermi*-LAT 4*FGL* catalog, the GC is classified as an associated source, since it has only been detected in gamma-rays because of the observable MSP [24]. This demonstrates a direct connection between MSP and GC gamma-ray emission a connection also seen in NGC 6626 [76], and (very recently) in NGC 6652 [135] where the pulsed emission of a single MSP can account for 25% and possibly 100% of the GC emission respectively. To date, twelve MSP have been detected within NGC 6624 at radio wavelengths [46]. A previous study of NGC 6624 [60] observed pulsed gamma-ray emission over a two year period [1] (August 2008 - October 2010) associated with the MSP J1823−3021A. The derived energy flux for MSP J1823−3021A suggests that this MSP accounts for the majority of the emission, and is currently the most luminous MSP observed in any GC. Additionally no other MSP could be detected in the off-pulse period of the pulsar.
This chapter presents an analysis of the gamma-ray data from a 13 year period to attempt to reproduce this result over this longer time period and test my analysis methods.

5.2 An Introduction to *Fermi*-LAT Analysis

5.2.1 *Fermi Science Tools* and `FERMIPY`

Broadly, the analysis of any *Fermi*-LAT data follows a model fitting procedure in which different spectral parameters of sources (such as the normalisation and spectral shape) are varied until their likelihood is maximised such that each parameter has the most likely value based on the assumed model. This process is broken into a series of steps where the event and source model are selected, the LAT exposure and live-time responses are computed and finally the spectral model is fitted. These steps of the analysis chain

[1] the pulsed emission was observed with a significance of 7σ over the observation period [60]

are implemented using the *Fermi Science Tools* [2] which can be invoked directly (after installing within a `PYTHON` environment) or more conveniently through the `PYTHON` wrapper code called `FERMIPY`, which is written by members of the *Fermi* collaboration.

I have used `FERMIPY` for all my *Fermi* analysis in this thesis. The `FERMIPY` package is based on the `pyLikelihood`interface and is described fully in [132]. I am using the latest `v1-0-1` version of `FERMIPY` in conjunction with the latest `PASS 8` instrument response functions . [3].

5.2.2 Obtaining *Fermi*-LAT data

The photon and spacecraft data files are downloaded in a series of *.fits* files from the NASA *Fermi*-LAT data server (also referred to as the *Fermi* Science Support Centre (FSSC)) [4] [97]. The object name (or coordinates) and radius around the object are chosen prior to download, along with the desired energy range and time period. The type of data is also specified, which is either photon data, or pre-computed spatial maps for extended sources (such as the Galactic diffuse emission model).

NGC 6624 Data Selected

In my analysis I selected all photon and spacecraft data taken during a 13-year period from `2008-08-04 15:43:36 - 2021-08-04 15:43:36` [5] of the *Fermi* mission. I have selected photon events between 100 MeV-100 GeV because *Fermi*-LAT has a poor point spread function (PSF) below 100 MeV and whilst GC emission typically peaks at a few GeV selecting a larger energy range gives a larger spectral 'lever-arm' [40] that is useful when fitting and comparing different spectral models.

I have selected all photons detected as originating within 15° circle (known as the `roiwidth`, or radius of interest (ROI)) which is centred on MSP J1823−3021A [6]. The size of `roiwidth` is determined by the LAT's point spread function for 100 MeV photons as shown in Figure 1.5.

5.2.3 Configuration

`FERMIPY` uses YAML [7] files to read and write its configuration for the analysis in a consistent format. The configuration file specifies the parameters for the analysis in a series of dictionaries:

[2] The *Fermi Science Tools* are described fully here: `https://github.com/fermi-lat/Fermitools-conda/wiki`, accessed .

[3] `https://fermipy.readthedocs.io/en/latest/`, accessed 01/06/22

[4] The data is downloaded here `https://fermi.gsfc.nasa.gov/cgi-bin/ssc/LAT/LATDataQuery.cgi`, accessed 01/06/22 .

[5] a Mission Elapsed Time (MET) period of 244512002 s - 654739206 s

[6] MSP J1823−3021A is listed under the name 4FGL J1823.5-3020 in the *Fermi*-LAT source catalogue

[7] an acronym for Yet Another Markup Language

```
{
data:
    evfile: /home/perseus/new_Pulsar_analysis/ngc6624/13yrdata/events_13yr.txt
    scfile : /home/perseus/new_Pulsar_analysis/ngc6624/13yrdata/
    L21111317252802F843A983_SC00.fits
    ltcube: /home/perseus/fermi-analysis/New_13yr_analysis/ltcube_00.fits

 binning:
    roiwidth: 15.0
    binsz: 0.1
    binsperdec: 5


 selection:
     emin: 100 #100MeV
     emax: 100000 #100GeV
     zmax: 90.0 #zenith angle
     evclass: 128
     evtype: 3
     tmin: 244512002
     tmax:  654739206
     filter: DATA_QUAL>0 && LAT_CONFIG==1 #recomended filter for point source,
    off-Galactic plane
     target: '4FGL J1823.5-3020'


 gtlike:
     edisp : True #energy dispersion correction enabled
     irfs : 'P8R2_SOURCE_V6'
     edisp_disable : ['isodiff', 'galdiff'] #don't use energy-dispersion
    correction on these sources


 model:
     src_roiwidth: 25.0
     galdiff: 'gll_iem_v07.fits'
     isodiff: 'iso_P8R3_SOURCE_V2_v1.txt'
     catalogs: 'gll_psc_v26.xml' # 4FGL-DR2 in .xml format, 13 year Fermi
    catalog of data
}
```

Configuration file for NGC 6624 Analysis

The **data** dictionary contains:

1. **evfile**: Path to the photon event files downloaded
2. **scfile**: Path to the spacecraft file (specifying the position and direction of *Fermi*-LAT every second)
3. **ltcube**: The (optional) path to the livetime cube file.

The **binning** dictionary contains:

1. **roiwidth**: Width of the ROI in degrees [8]
2. **binsz**: Spatial bin size in degrees
3. **binsperdec**: Number of energy bins per decade (i.e here, there will be 5, evenly spaced energy bins between 100 and 1000 MeV

The **selection** dictionary contains information about the photon data we are selecting from the **data**:

1. **emin/emax**: Minimum/ Maximum energy in analysis (MeV)
2. **zmax**: Maximum zenith angle of photons allowed in analysis

[8] The ROI is the radius of interest, which is a circular region centred on the target object being analysed

3. **evclass**: Event class selection, use 128 for photons

4. **tmin/tmax**: Minimum/ Maximum time in analysis (s)

5. **filter**: Filter string for gtmktime selection, ensures good quality photon data selected

6. **target**: Target object

The **gtlike** dictionary contains:

1. **edisp**: Enable the correction for energy dispersion on sources.

2. **irfs**: File containing the instrument response functions

3. **edisp_disable**: Energy dispersion should be disabled on diffuse sources in model

The **model** dictionary contains:

1. **src_roiwidth**: Radius of circular radius in degrees centred on the ROI that selects sources for inclusion in the model

2. **galdiff**: Path to Galactic diffuse emission mapcube

3. **isodiff**: Path to isotropic diffuse emission template

4. **catalogs**: an *xml* file containing all sources in the ROI, their position, and the *Fermi* collaboration best spectral model parameters

The zenith cut of 90° was applied to the data (which is recommended by the FSSC to significantly reduce contamination from gamma-rays originating from the Earth limb). Events were filtered to improve data quality using only 'good time intervals', by specifying a `DATA QUAL > 0 & & LAT CONFIG == 1`.

5.3 Data Analysis for *Fermi*-LAT

5.3.1 Method for *Fermi*-LAT Analysis

A maximum likelihood analysis is a technique to estimate the parameters from a probability distribution, given some observed data. In order to do this, you need a maximum likelihood function that can be maximised so that, under the assumed probability distribution, the observed data is most likely. In this section I am going to outline the mathematics of a maximum likelihood analysis, which is used to analyse *Fermi*-LAT data.

Principles of Maximum Likelihood

The aim of a *Fermi*-LAT fit is to produce an accurate model that describes a set of photon data collected, and also includes any parameters we may want to estimate (e.g the energy flux of a source). By making the assumption that the model chosen is true, it is possible to produce a probability density function (PDF) for the data. This means that you have a measure of how likely your data is for a given input model [93]. The input model is produced by the FSSC and is the distribution of all gamma-ray sources observed with *Fermi*-LAT and contains all measured parameters of each source (such as the position, energy and photon fluxes and predicted spectral model). The probability of obtaining the data given the input model is then maximised in an iterative process

where different parameters are freed in each energy bin independently, and the model is fitted to the data in each pixel.

Fermi-LAT analysis is performed using photon counts, binned by energy and position (or pixels). The photon counts from the data (X) are compared to the counts predicted by the model Θ. This approach is known as Bayes' theorem, it describes the probability of an event occurring (in *Fermi* analysis this is the probability of observing a given photon 'event') , based on prior knowledge of any conditions that might be related to the event (which is contained in the model of gamma-ray sources). Bayes' theorem is based on conditional probability [11], assuming that each photon event is independent then the probability of obtaining X_i photons given there are Θ_i predicted by the model is:

$$P(X_i|\Theta_i) = P(X_i)P(\Theta_i) \tag{5.1}$$

and the overall likelihood $\mathscr{L}(\Theta|X)$ of the model describing the data is the product of the probabilities in each bin:

$$\mathscr{L}(\Theta|X) = \prod_i P(X_i|\Theta_i) \tag{5.2}$$

Photons can be modelled as independent random variables, and the Central Limit Theorem [114] tells us that they can be modelled using the Normal Distribution. The number of photons (overall as well as per energy bin and per pixel) is also very large. and can therefore also be approximated to the Poisson distribution which means that if there are n_i photons detected and m_i predicted in bin i:

$$\mathscr{L}(\Theta|X) = \prod_i \frac{m_i^{n_i} e^{-m_i}}{n_i!} \tag{5.3}$$

we usually find that $\mathscr{L}$ is very large, so it is often more convenient to take the natural log of $\mathscr{L}$. For a large number of photon events n, $\ln(\mathscr{L}(\Theta|X))$ can be approximated to a Poisson distribution with a mean n and standard deviation of $\sqrt{n}$. The different parameters can then be estimated, and the best fit model found by maximising the likelihood (or log likelihood) using calculus. This is what the *fit()* method does in the `GTAnalysis` package. The maximum likelihood for different models can be compared to test the relative goodness of fit for different models. This is known as Wilk's Theorem and called the Test Statistic (TS) [131].

Comparing the Spectral Models

A larger likelihood value $\mathscr{L}$ (or $\ln(\mathscr{L})$) implies that a model more closely fits the data. If we want to compare the relative fits of different spectral models, you can calculate a quantity known as the Test Significance (TS), for instance, in the case of two models with likelihoods $\mathscr{L}_0$ and $\mathscr{L}_1$ then

$$\mathrm{TS} = -2\ln\left(\frac{\mathscr{L}_0}{\mathscr{L}_1}\right) \tag{5.4}$$

as a rule of thumb,

$$\sigma = \sqrt{\mathrm{TS}} \tag{5.5}$$

if your models both have 2 degrees of freedom. However the significance decreases

the more degrees of freedom you have in your model. Indeed, it is not straightforward to account for all the degrees of freedom in the model so it is often best to just compare the TS values [93].

5.3.2 *Fermi* Analysis of NGC 6624

Setup

The analysis is done using the *GTAnalysis* method which is a wrapper over the underlying *PyLikelihood* classes [9]. *GTAnalysis* is invoked with the configuration file shown in Section 5.2.3. The verbosity is chosen to provide the desired level of information given out during the analysis (I have selected a verbosity of 3). Initially the analysis is started using the *setup()* command within *GTAnalysis*. This command performs the data preparation and response calculations needed for the analysis, including selecting the sources within the specified ROI from the catalogue [24], and creating a sky map containing the photon count (for each source) and accounting for the exposure levels of LAT. The *optimize()* method subsequently iterates over all model components in the radius of interest ROI freeing them and fitting their normalisation and spectral shape parameters (which are in the catalogue [24]).

Freeing Source Parameters

The normalisation and spectral shapes of all the sources in the ROI are initially fixed to the values assigned in the optimization step. This is so that the sources that will most influence the fit of the data to the model can be freed. If there are too many free parameters in the model then the fit will not converge.

Specific sources can then be freed manually using the *free_sources()* method. This step is crucial for the maximum likelihood analysis. By freeing different spectral parameters (such as the spectral shape and normalisation) for different sources, the number of photons predicted can vary and produce a probability density function that can be maximised (as described by equation 5.2). Sources are freed based on how much they will affect the final maximum likelihood result. Sources closest to the target object (i.e NGC 6624 in this example), sources with the largest TS [10], and the isotropic and Galactic diffuse emission are all likely to significantly influence the fit. The more free parameters there are, the more accurate the final result is likely to be; however, too many free parameters will result in the fitting methods being unable to converge.

In order to decide which sources to free it is helpful to look at the energy spectrum (shown in Figure 5.1) produced after the *optimize()* method is called. Figure 5.1 demonstrates that there are a lot of bright sources around NGC 6624 and that the isotropic and Galactic diffuse emission sources are most significant (which is not surprising given NGC 6624's Galactic coordinates are $(2.79°, -7.91°)$ [60]).

[9] `https://www.slac.stanford.edu/exp/glast/wb/prod/pages/sciTools_pyLikelihood_tutorial/v02/10_pyLikelihood_Attributes_andMethods.html` accessed 27/07/22

[10] because they have the most statistically significant gamma-ray emission they are likely to be brightest and emit the most photons

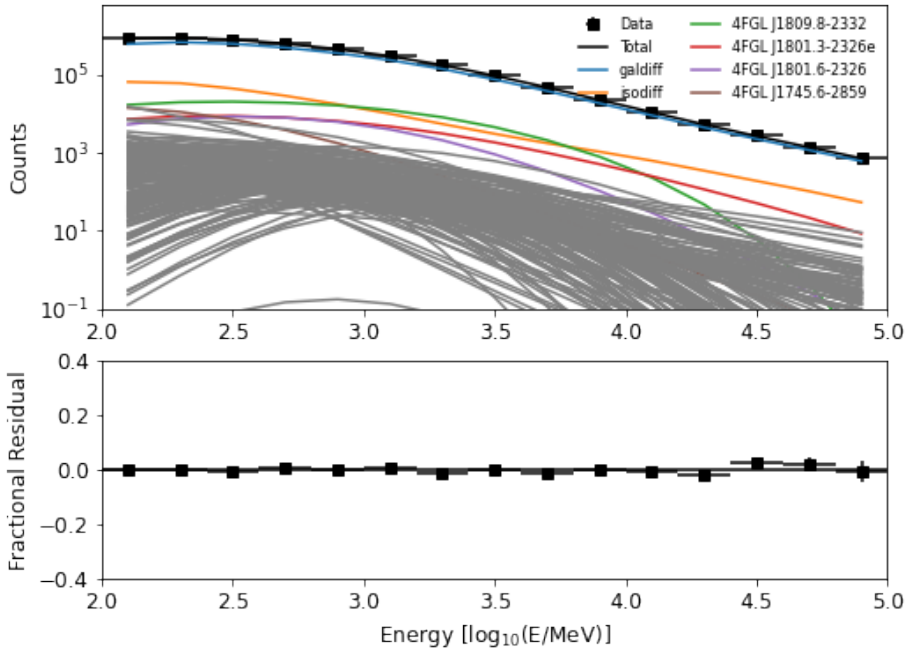

Figure 5.1: Energy spectrum showing number of counts for brightest sources in the ROI, it is clear that emission is dominated by isotropic diffuse (isodiff) and Galactic diffuse emission(galdiff). There are small residuals at all energies, but fewer photons are detected at higher energies and consequently the residuals are slightly larger.

It is also useful to look at the initial TS of sources in the ROI and how they are distributed in the sky relative to NGC 6624. This can be done using the *print_roi()* method, an example of this is shown in Figure 5.2. The source at the centre (with off-set of 0.000 is NGC 6624), but there are a number of sources within a few degrees of the GC (the ROI chosen is 15° and Figure 5.2 is showing only the closest sources), the 'ts' column also shows that the majority of sources have statistically significant gamma-ray emission (defined as $TS > 25$). After making these observations I chose the objects that I wish to free when computing the fit.

```
2022-06-27 14:07:25 INFO    GTAnalysis.optimize(): Finished
2022-06-27 14:07:25 INFO    GTAnalysis.optimize(): LogLike: 11469392.263090 Delta-LogLike: 3111.054954
2022-06-27 14:07:25 INFO    GTAnalysis.optimize(): Execution time: 2995.30 s
2022-06-27 14:07:25 INFO    GTAnalysis.print_roi():
name                SpatialModel   SpectrumType     offset        ts       npred
--------------------------------------------------------------------------------
4FGL J1823.5-3020   PointSource    PLSuperExpCuto    0.000    980.52      3889.3
4FGL J1819.9-2926   PointSource    LogParabola       1.200    100.44      1311.3
4FGL J1817.2-3035   PointSource    PowerLaw          1.385    162.70      3493.3
4FGL J1822.0-3146   PointSource    PowerLaw          1.467     34.97       797.1
4FGL J1825.9-3153   PointSource    PowerLaw          1.627     19.00      1070.9
4FGL J1826.2-2830   PointSource    LogParabola       1.926     27.35       923.9
4FGL J1830.8-3132   PointSource    LogParabola       1.955    232.48       901.9
4FGL J1820.7-3217   PointSource    LogParabola       2.031     79.94       692.1
4FGL J1814.2-3000   PointSource    LogParabola       2.033     47.80       605.8
4FGL J1816.3-2903   PointSource    LogParabola       2.038     67.19      1230.4
4FGL J1818.6-3206   PointSource    LogParabola       2.047    161.93      1660.8
4FGL J1824.7-3243   PointSource    LogParabola       2.381     45.48       488.4
4FGL J1830.7-3219   PointSource    PowerLaw          2.507      8.82       614.2
4FGL J1812.8-3144   PointSource    LogParabola       2.680    133.36       784.4
4FGL J1828.2-3252   PointSource    LogParabola       2.708     42.68       276.6
4FGL J1816.8-2800   PointSource    LogParabola       2.760     40.65      1185.2
4FGL J1817.6-3251   PointSource    LogParabola       2.806     47.94       719.2
4FGL J1810.2-3054   PointSource    LogParabola       2.926     45.15      1044.9
4FGL J1834.9-2819   PointSource    PowerLaw          3.214     78.12      2587.2
4FGL J1816.4-2727   PointSource    LogParabola       3.288     95.30      1077.5
4FGL J1808.2-3005   PointSource    PowerLaw          3.310     50.17      2782.3
4FGL J1837.6-2904   PointSource    LogParabola       3.319    140.39      1484.0
4FGL J1817.9-3334   PointSource    LogParabola       3.438    169.37      1185.1
4FGL J1809.0-2853   PointSource    LogParabola       3.472     52.64      1285.4
4FGL J1830.7-2713   PointSource    PowerLaw          3.498    214.83      3260.4
4FGL J1811.2-2759   PointSource    PowerLaw          3.576     52.58      1037.7
4FGL J1815.2-2715   PointSource    PowerLaw          3.588    119.04      3976.3
4FGL J1820.3-2646   PointSource    LogParabola       3.640     17.45      1300.8
4FGL J1835.7-3258   PointSource    LogParabola       3.688    187.19      1224.0
```

Figure 5.2: A screenshot of a subsection of the terminal output after the command *print_roi()*. The 4FGL source name, spatial model and spectral shape are all assigned from the *Fermi*-LAT catalogue. The TS and photon count (npred) are assigned after each fit.

Freeing Source Parameters - NGC 6624 ROI

The normalisation and spectral shape of all sources within 2° of the object (NGC 6624) are free to vary. I have also allowed the normalisation of the Galactic diffuse, and isotropic diffuse gamma-ray emission [11] to vary. I also free the normalisation of all sources within 5° of NGC 6624. I also free all objects with a TS > 100 within the ROI and the *srcwidth* (which is a circle of radius 25° centred on the GC). These are the objects with the most statistically significant gamma-emission (and are also likely the brightest objects). The detection threshold for a source is a TS $= 25$, however over a 13 year period the vast majority of sources in the ROI will meet this threshold. Freeing the normalisation/ spectral shape of all these sources will result in there being too many free parameters for the fit to converge. The *find_sources()* method is used to search for any additional, unlisted sources, these tend to be discovered only in observations made with the LAT after the catalogue was compiled (i.e AGN and other transient sources) and often have low TS values. Sources detected with a significance $\sigma < 4$ are deleted, as they are statistically insignificant and will not affect the result.

The maximum likelihood model is calculated using the *fit()* method. This method iterates through the free parameters, determining the likelihood for trial sets of parameters (initial conditions which are the initial parameters in the $4FGL$ catalog) and searching for the maximum likelihood (using the derivative of the likelihood function to find a minimum stationary point). The TS and predicted photon count (npred) values of all sources are then updated. In practice the fitting method is called after each set of parameters is freed, to ensure it can converge. I have used the `NEWMINUIT` likelihood

[11] which are background sources of emission and are defined in spatial maps within the configuration file

optimiser, with no errors (corresponding to a quality of 3), a fit quality threshold of 2 and a tolerance of 0.01.

Other higher level analysis methods can be used to determine the likelihood of extended emission from the object and to test the most likely position of the source (if it is different to the position in the *Fermi* catalogue).

Results of Maximum Likelihood Analysis - NGC 6624

A residual map as shown in Figure 5.3 shows how well the final model fits the data. Small scale residuals (mostly less than 1σ), with no large structure indicate a good fit.

The residual plots both indicate there is more significant emission originating around the source than expected by the model and a region (bottom left shown in blue) where the emission has been significantly under-fitted. These findings might suggest that the model is not a good fit to the data.

However, looking at Figure 5.4, a residual plot with the Galactic diffuse emission removed, shows that there is some uncertainty in the Galactic plane emission, which is probably the reason for the under-fitting shown in Figure 5.3. This plot illustrates why I considered the proximity to the Galactic plane in my selection criteria for GC.

Figure 5.5 is a map of the TS of the region of sky around NGC 6624. This figure demonstrates that the most significant source of gamma-ray emission in this region of the sky is the GC, but that there are other significant sources (shown in yellow), in this region.

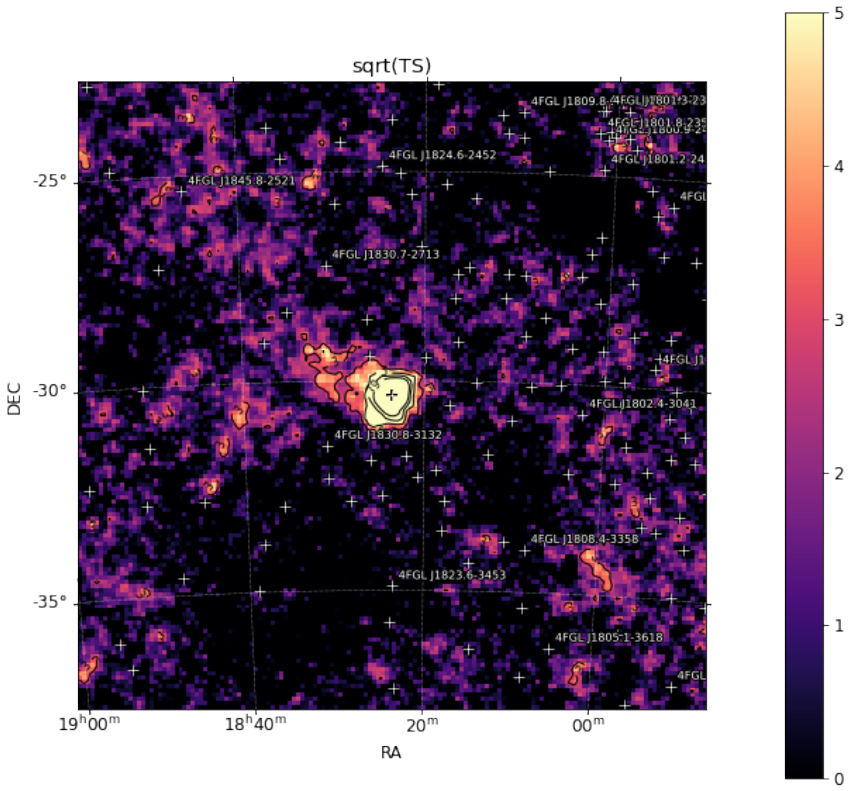

Figure 5.5: TS map of ROI around NGC 6624. The scale used is $\sqrt{\text{TS}}$ which is a measure of the statistical significance of the emission. The figure shows that the most significant source of emission is at the centre (which is where the GC is) this is consistent with a point source.

5.4 Spectral Analysis

Finally a binned, Spectral Energy Distribution (SED) of the source can be computed using the *sed()* method, which performs an independent fit for the flux normalisation of a source in bins of energy (specified by the energy range and bin number in the configuration file). The normalisation in each bin is fitted using a power-law spectral parameterization with a fixed index. A useful output dictionary (in a *numpy* array) with the SED parameters (such as the TS of each energy bin and spectral shape parameters) is produced, along with a plot of the energy spectrum. I will discuss the significance of the SED in more detail in Section 5.4.2.

Once the SED has been calculated for a source, the relative fit of different spectral models can be compared, which can give insight into the likely sources of emission from within the GC.

The different spectral models that are likely for a GC were defined in Section 2.1.3. These are the Log Parabola (which I will refer to as LP), the Power Law with Exponential cut-off (which I will refer to as PLExp) and Power Law spectral shape (which I will refer

to as PL).

5.4.1 Comparing Spectral Models

Method 1 - Comparing TS

One method to compare two models (A and B) is to compare their log likelihoods by calculating the test significance (TS):

$$\mathrm{TS} = 2(\mathscr{L}_A - \mathscr{L}_B) \tag{5.6}$$

Where $\mathscr{L}_A$, $\mathscr{L}_B$ are the log likelihoods of the two models being compared. A positive TS indicates that model A is preferred over model B whereas a negative TS indicates that model B is preferred over model A. As I have mentioned previously, for one degree of freedom the significance (σ) one model is preferred over another is

$$\sigma = \sqrt{TS} \tag{5.7}$$

however, the significance decreases with the number of free parameters in the model. With this in mind, I am also going to use the AIC to draw comparisons between different models.

Method 2 - Akaike Information Criterion (AIC)

The AIC can be used to determine quantitatively if one model fit is significantly better than another and will also penalise a model with more free parameters, which may result in overfitting the data [19].

The AIC statistic is defined as:

$$\mathrm{AIC} = -2\ln(\mathscr{L}) + 2k \tag{5.8}$$

where $\mathscr{L}$ is the likelihood of the model and k is the number of degrees of freedom of the model. The AIC allows you different models to be compared, and the model with the lowest AIC statistic is considered to be preferred.

The difference between the AIC values (ΔAIC) can be used to compare the relative merits of two models (for examples models A and B).:

$$\Delta\mathrm{AIC} = AIC_A - AIC_B \tag{5.9}$$

a difference, $\Delta\mathrm{AIC} > 2$ is generally considered to be a statistically significant difference that shows a statistically significant difference between models [87].

Degrees of Freedom for Different Spectral Models

The LP spectral model (defined in equation 2.2) has three free parameters (k= 3), the normalisation, and the exponents α and β.

The PL model (defined in equation 2.3) has two free parameters (k= 2), the normalisation and index . The PLExp (defined in equation 2.4) has three free parameters (k= 3), the normalisation, spectral index and cutoff energy.

5.4.2 NGC 6624 Spectral Analysis

Table 5.1 outlines some of the key values calculated from the analysis of 13 years of data from NGC 6624.

Parameter	Value
TS	951
Photon count	3550
Energy flux ($\mathrm{MeVcm^{-2}s^{-1}}$)	$(7.87 \pm 0.30) \times 10^{-6}$
Photon flux ($\mathrm{cm^{-2}s^{-1}}$)	$(1.06 \pm 0.01) \times 10^{-8}$

Table 5.1: Table showing final TS, number of photons detected (photon count or 'npred'), energy and photon fluxes detected from NGC 6624 in my 13 year analysis.

Following the computation of the SED the spectrum can be fitted to different spectral models as described in Section 2.1.3 and the relative fit of each model can be compared using the TS and AIC criterion as described in Sections 5.4.1 and 5.4.1.

Model	Log-likelihood	AIC	Δ AIC
PLExp	11469502.646	-11469496.646	0
LP	11469501.467	-11469495.467	1.18
PL	11469448.568	-11469444.568	52.0

Table 5.2: Table comparing the AIC for different spectral models to NGC 6624's spectrum. The AIC is used to determine the relative likelihood that the data came from a given model and the difference in AIC indicates the relative likelihood the data came from different models. In this table Δ AIC is defined as the difference between the AIC of the PLExp model and another model. The AIC indicates that the models are ranked (best to worst) as PLExp, LP, PL. The column labelled Δ AIC indicates that the PLExp and LP models are equally good models to NGC 6624's spectrum, and that the PL model is a worse fit.

Table 5.2 ranks the models (from best to worst) as PLExp, LP, PL. It is clear that the data is not well-fitted by a power law. However, the difference in AIC between the PLExp and LP of 1.18 suggests that we cannot statistically distinguish which model is a better fit to the data.

Spectral models being compared	TS
PLExp vs. LP	2.36
PLExp vs. PL	108
LP vs. PL	106

Table 5.3: A comparison of the fit of the spectral models to NGC 6224's spectrum. The TS is the statistical significance that a model is preferred over the other (as defined in equation 5.6). The TS values indicate that the PLExp and LP are both significantly preferred over the PL.

The TS values given in Table 5.3 also show that it is not possible to statistically distinguish between the PLExp and LP models and that both the PLExp and LP are significantly preferred over a PL fit.

This can be observed by visually comparing the fit of the PLExp and LP to NGC 6624's spectrum in Figure 5.6. As can be seen, the PLExp and LP appear to be a very similar shape. The upper limits show that there is no significant emission below 500 MeV or above 10 000 MeV, which is likely the reason that the PLExp and LP models cannot

be distinguished statistically. There is tension between the PLExp and LP models and the data in the second and third lowest energy bins, where the energy flux is an upper limit, below the 1σ uncertainty on the fit.

Previous studies of NGC 6624 in [60] had shown the GC fitted with a PLExp model, however no comparison with the LP was made. As the GC has been listed as an associated source with a MSP, it may be surprising that the PLExp model (expected for MSPs) and the LP fit equally well. One possible reason could be because of gamma-ray emission from other sources within the GC. Whilst any such objects may be faint compared to the observed MSP, over 13 years this becomes significant in the observed shape of the integrated energy spectrum.

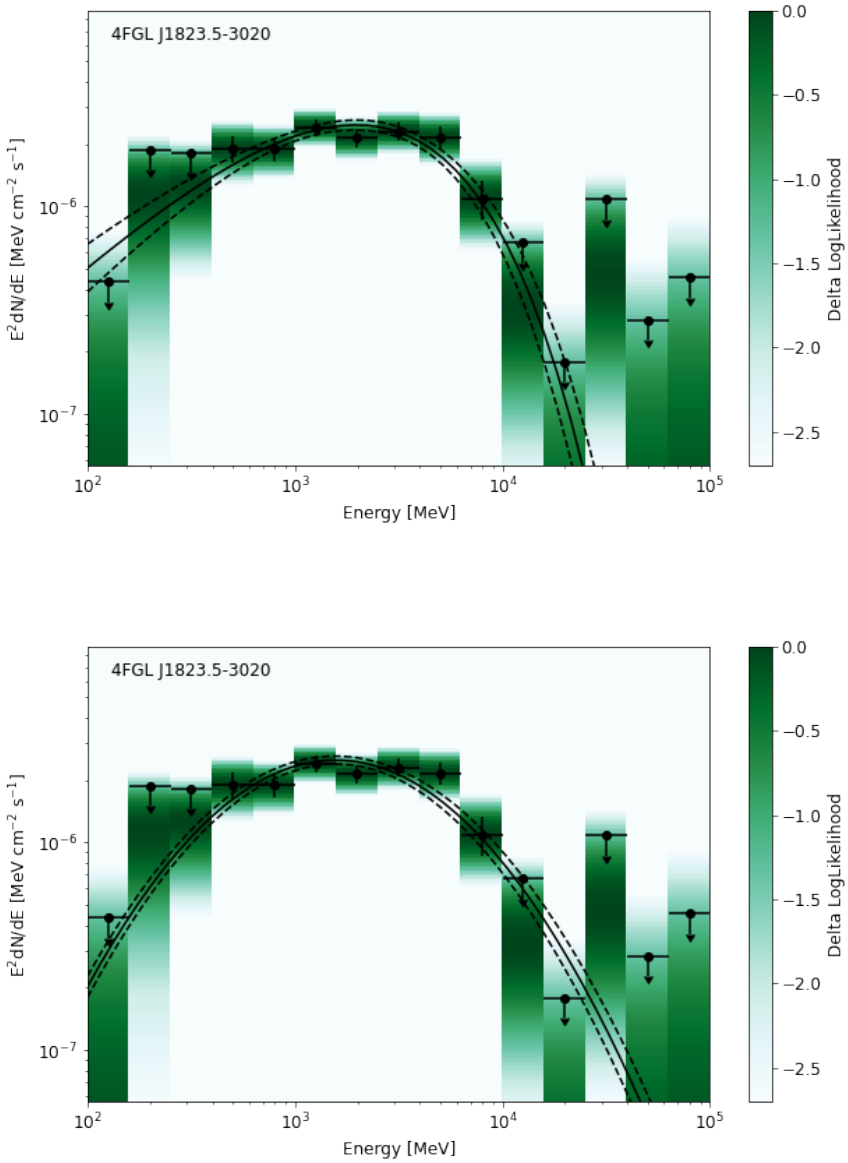

Figure 5.6: NGC 6624 (4FGL J1823.5-3020) spectrum fitted with PLExp (top) and LP (bottom) models. The error bars show 1σ uncertainty on $E^2 \frac{dN}{dE}$ from the likelihood curvature. The upper limits are 95% confidence limits evaluated from the profile likelihood. Bins with a TS < 16 have been shown as upper limits.

Parameters	Value
N_0 ($\mathrm{MeV}^{-1}\mathrm{cm}^{-2}\mathrm{s}^{-1}$)	$(1.01 \pm 0.14) \times 10^{-11}$
γ_1	-1.06 ± 0.29
E_0 (MeV)	533
E_c (MeV)	1172 ± 508
γ_2	0.667

Table 5.4: The parameters for the best fit PLExp to NGC 6624's spectrum (shown in Figure 5.6). The functional form is described in equation 2.4.

Parameter	Value
N_0 ($\mathrm{MeV}^{-1}\mathrm{cm}^{-2}\mathrm{s}^{-1}$)	$(1.11 \pm 0.16) \times 10^{-11}$
α	0.903 ± 0.146
β	0.331 ± 0.037
E_b (MeV)	300

Table 5.5: The parameters for the best fit LP to NGC 6624's spectrum (shown in Figure 5.6). The functional form is described in equation 2.2.

5.5 Searching for Evidence of Pulsed Emission in NGC 6624

5.5.1 Ephemeris for MSP J1823-3021 A

The MSP ephemeris was obtained from the *Fermi*-LAT gamma-ray pulsar catalogue [12] because it has already been detected by *Fermi*-LAT [60]. The ephemeris is shown in Figure 5.7 and the parameters in the ephemeris are defined in Chapter 4.4.1.

```
PSRJ           J1823-3021A
RAJ            18:23:40.48        0.00
DECJ           -30:21:39.99           0.00
F0             183.82         0.00
F1             -1.14135e-13   4e-19
F2             5.79204e-25   1.37054e-26
PEPOCH         54939.00
POSEPOCH       50637.03
DMEPOCH        54939
DM             86.8628     0.0093
START          53773.35
FINISH         55483.67
TZRMJD         54635.03
TZRFRQ         1402
TZRSITE        8
```

Figure 5.7: Radio ephemerides for MSP J1823-3021A [60]. The parameter names are given in the first column, the values, and the error (if known) on each measurement are given in the middle and right-hand columns.

5.5.2 Phase-folding Photon Data

The photon events in the final *.fits* data cube file produced in my analysis are phase folded using the ephemeris with the `TEMPO2` plugin. The radio pulse profile produced by [60] is shown in Figure 5.9. Initially, I tried phase folding without adding any weighting as shown in Figure 5.8. No pulsed emission can be seen in this light-curve.

[12] https://fermi.gsfc.nasa.gov/ssc/data/access/lat/2nd_PSR_catalog/, accessed on 13/02/22

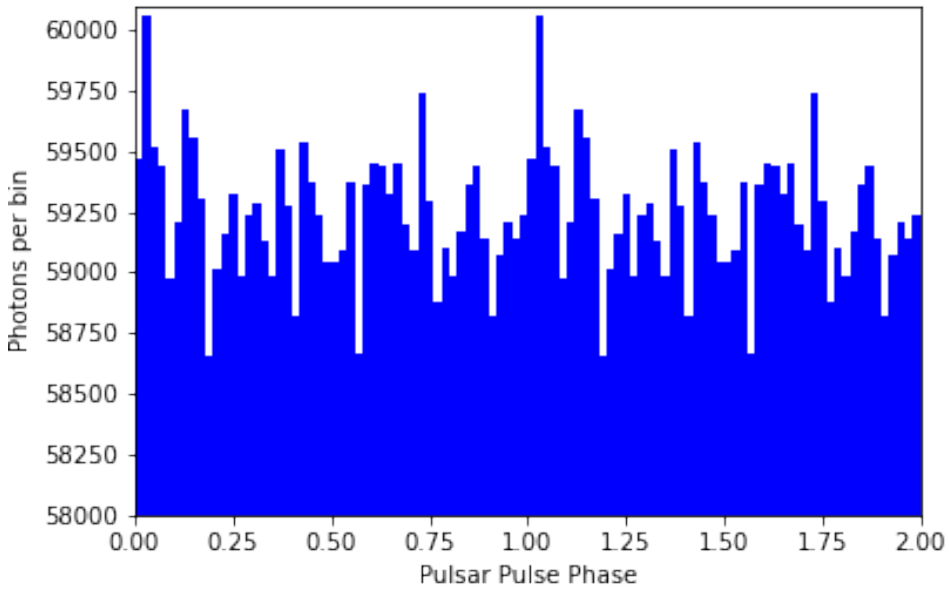

Figure 5.8: Phase folded light-curve of NGC 6624, using no weighting. The bins each have a width of $0\,2\phi$. There is no visible pulsation and a large number of counts in each bin.

However, each photon can be weighted according to the probability it originated from the GC. This weighting is described in more detail in Chapter 4.6, and is calculated using the *compute_srcprob* method in *GTAnalysis*. This calculates the response of each diffuse source in the ROI and the probability each photon originated from the GC and reduces the number of background photons. I chose to use 50 bins per period in the light-curve after examining the width of the radio pulses and then used the calculated photon probabilities to produce a weighted histogram of the number of photons in each bin.

Figure 5.9 shows a comparison between the radio pulse profile and the weighted (gamma-ray) light-curve of NGC 6624 over the 13 year observation period. It is clear that the MSP J1823-3021A has been detected in the 'on-pulse' regions of $0.9 < \phi < 1.01$ and $0.6 < \phi < 0.67$, which is consistent with the radio pulse profile. MSP J1823−3021A has never been timed over a thirteen year period using gamma-rays before and demonstrates just how stable MSPs can be. Young gamma-ray pulsars, such as the famous Vela pulsar tend to 'glitch' and it is difficult to produce an ephemeris that is valid over such a long period [103]. By comparing the radio pulse profile and phase folded gamma-ray light-curve you can see that the relative heights of the main pulse (between $0.9 < \phi < 1.01$) and the inter-pulse (between $0.6 < \phi < 0.67$) are different. At radio wavelengths the main pulse is observed to be around 8 times stronger than the inter-pulse, but in the gamma-ray light-curve the main pulse is only around 1.5 times stronger than the inter-pulse. Additionally in the gamma-ray light-curve the main pulse is less symmetric than in the radio profile. These features are very typical of MSPs and have been observed in other similar studies [109, 67] .

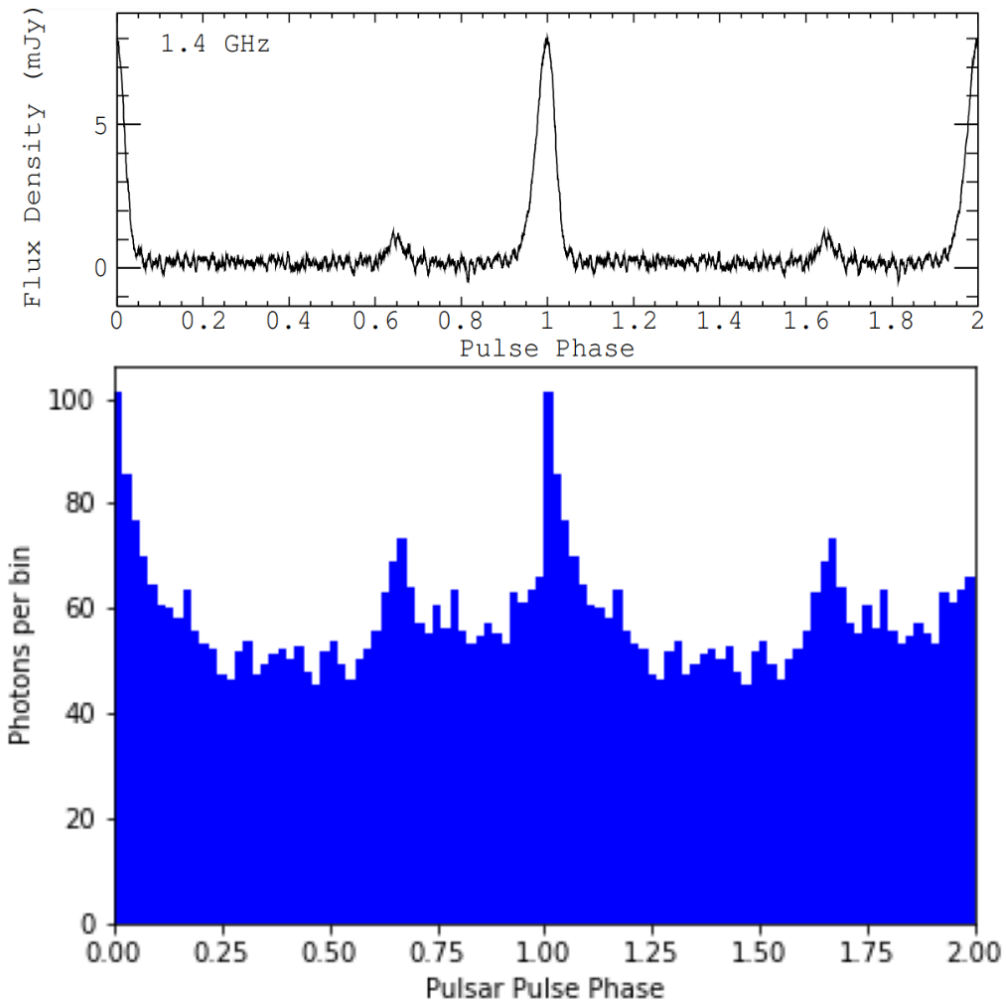

Figure 5.9: A weighted phase-folded light-curve with bin width of 0.02ϕ, this binning has been chosen because of the width of the radio pulses. Note the ratio in amplitude between the inter-pulse and main pulse is smaller in gamma-rays compared to radio wavelengths. Radio pulse profile of MSP J1823−3021A, taken from [60]. Note the main pulse is around 8 times stronger than the inter-pulse at radio wavelengths.

The area under the light-curve is 2904 photons, which supports the observations made by [60] that the MSP contributes most of the emission.

Conducting an H-test (Section 4.5.3) demonstrates emission has been detected between 300 MeV and 40 GeV with a significance over 5σ. The Gaussian profile of the H-test results plotted vs. energy (Figure 5.10)is typical of gamma-ray pulsars [16]. The maximum pulsation is detected at an energy of 6300 MeV with an H-test of 122 (11σ). These findings support the previous observations that MSP J1823−3021A is a very bright, energetic gamma-ray pulsar and is perhaps atypical of other MSP, given that this MSP seems to account for nearly all of the GC emission.

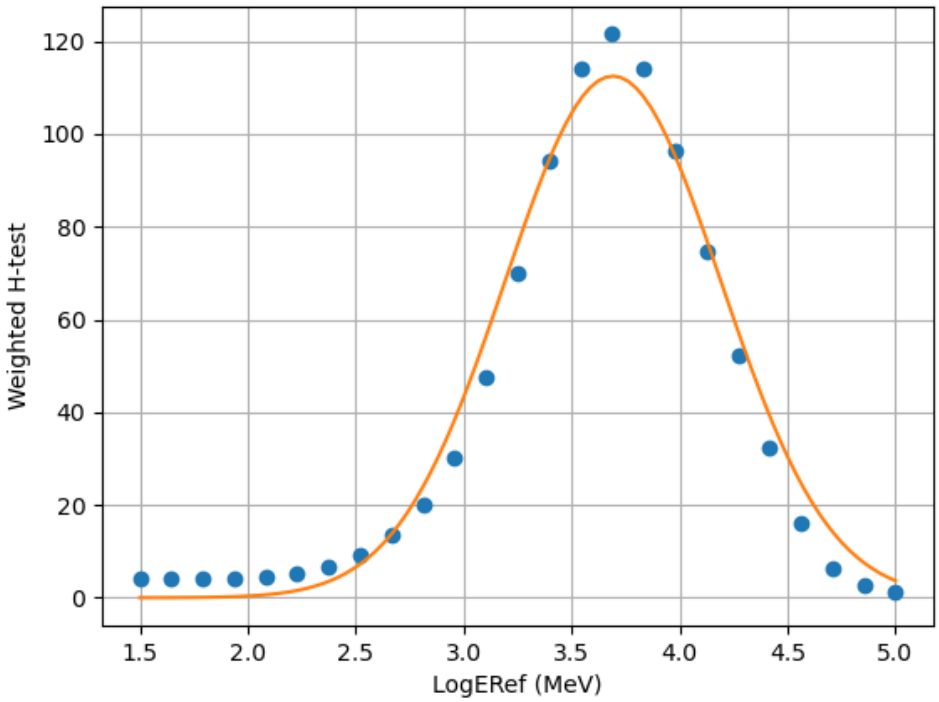

Figure 5.10: Plot of H-test, the significance of pulsation against energy for MSP J1823−3021A. The bell-curve shape is typical of gamma-ray pulsars.

5.5.3 Conclusions

I have demonstrated an analysis of GC NGC 6624 using the `FERMIPY` analysis package, and have compared the relative fits of different possible spectral shapes to NGC 6624's binned energy spectrum. I have then searched for evidence of pulsed emission from the MSP that has already been detected in the GC, and have found that the photon count implies that MSP J1823-3021 A does indeed seem to account for nearly 100% of the gamma-ray emission from NGC 6624.

Now that I have confirmed that my analysis methods are valid I will use these techniques to search for gamma-ray emission in the other GC I have selected for study.

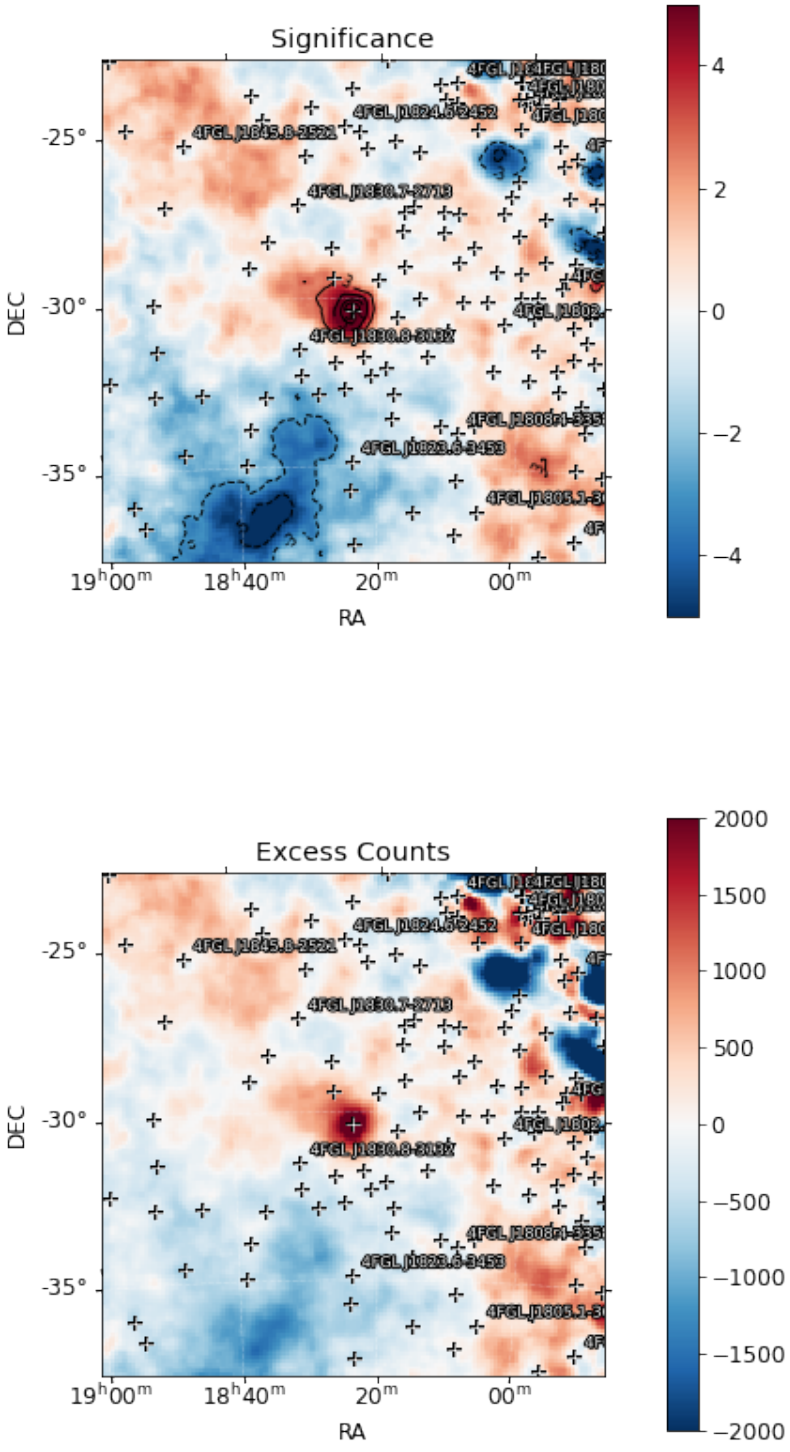

Figure 5.3: Residual plots (difference between best fit model and data) with the gamma-ray source NGC 6624 removed from the model. The first plot shows the residuals in terms of significance (σ) and the second plot shows the residuals in terms of the photon counts. Sources with a TS < 200 are labelled as crosses, sources with TS > 200 are labelled with their 4FGL name. The large photon count excess and high significance region at the centre of both residual plots show clearly how significant the gamma-ray emission is in NGC 6624 compared to the surrounding sky.

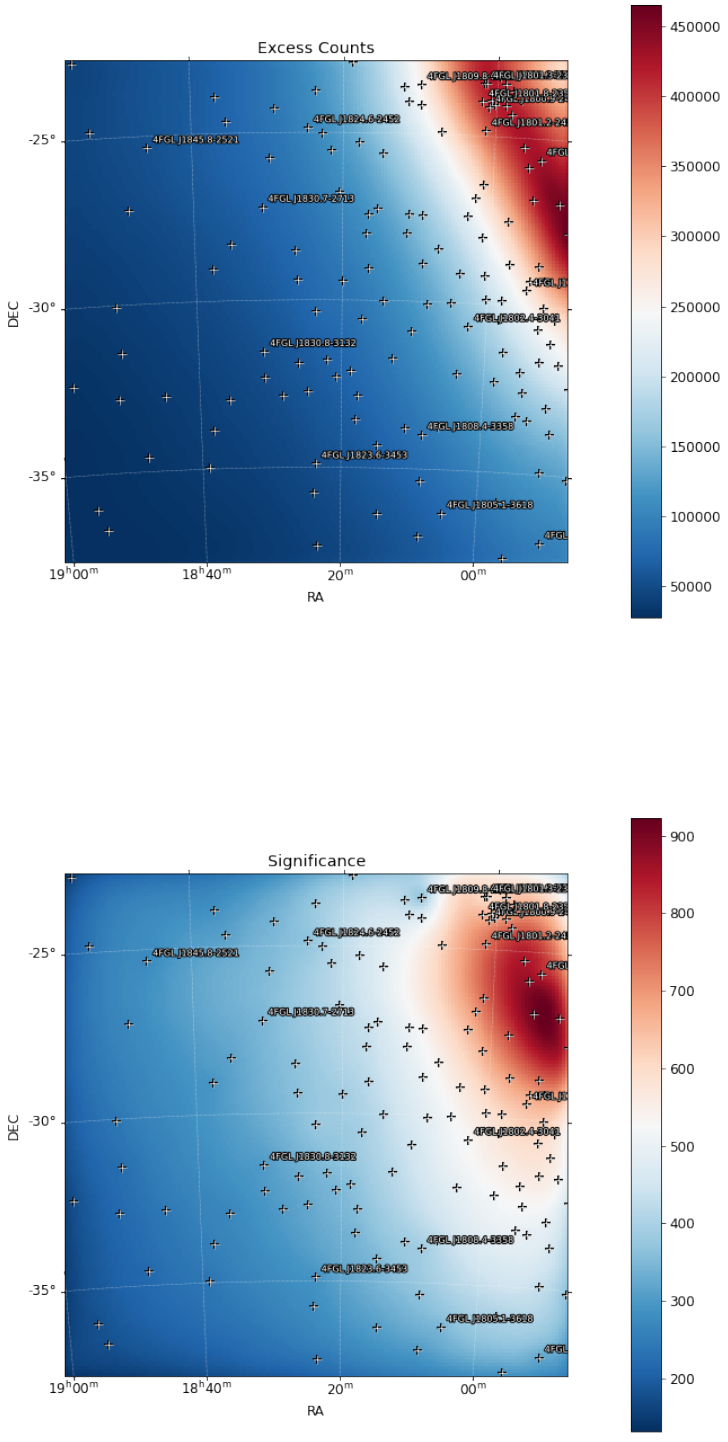

Figure 5.4: Residual plots (difference between best fit model and data) for NGC 6624 shown in terms of photon counts (top) and in terms of significance (σ) (bottom) the Galactic diffuse emission has been removed from the model. Sources with a TS < 200 are labelled as crosses, sources with a TS < 200 are labelled with their 4FGL name. These residual plots indicate that the gamma-ray emission from NGC 6624 has been fully accounted for.

Chapter 6

Globular Cluster Analysis

6.1 Introduction

In this chapter I present the results of my analysis for the GC I have selected to study using 13 years of `PASS 8` *Fermi*-LAT data in the energy range of 100 MeV - 100 GeV. I produce refined spectral fits for each GC and will also compare the relative quality of the fit of different spectral models.

6.2 Analysis Method

I am using the same analysis routine as for NGC 6624 (Chapter 5) but with some modifications to the exact parameters used in my analysis based on the GC's brightness, TS and proximity to the Galactic plane [1], primarily to ensure that there were not too many free parameters in the ROI. The exact parameters used for each GC are outlined in Table 6.1.

6.2.1 Parameters used in Analysis

GC	`binsperdec`	TS threshold	*free_sources (d=, 'norm')*	*free_sources (d=,)*
ω Centauri	5	25	4.0	1.0
47 Tuc	8	100	5.0	3.0
NGC 6752	5	25	4.0	1.0
NGC 6641	5	100	3.0	1.0
Terzan 5	8	100	3.0	1.0
NGC 7078	5	25	4.0	1.0

Table 6.1: Table showing the parameters used in analysis for each GC. The parameter `d` is the angular radius (°) in which sources are freed. The meanings of the columns are described in the text.

The column labelled '`binsperdec`' indicates the number of energy bins used per decade in energy (measured in MeV), I have used more bins per decade for the GC that have the highest energy flux and TS because they have better photon statistics and therefore it is possible to produce a more finely binned energy spectrum for each bin.

[1] because objects closer to the Galactic plane tend to have far more sources within their ROI

The column labelled 'TS' threshold gives the TS for each source in the ROI above which I freed the spectral shape and normalisation [2] . I chose different thresholds for different sources depending on how many bright objects there were in the ROI around the GC. Sources detected with a TS $>$ 25 are included in the 4FGL-DR2 catalogue [24]. Analysing over a 13 year analysis period means that a considerable number of sources above this threshold now exist and freeing too many sources will result in the *fit()* methods not converging. NGC 6441 and Terzan 5 are close to the Galactic plane and are therefore surrounded by more bright sources so only sources with TS $>$ 100 are freed. In contrast, NGC 6752 and NGC 7078 are off the Galactic plane but are also fainter and so I have therefore set the TS threshold lower. ω Centauri does not have many bright sources close by so all sources with TS $>$ 25 are freed. However, 47 Tuc is surrounded by many more point sources than ω Centauri and consequently only sources with TS $>$ 100 are freed.

The column labelled *free_sources(d=, 'norm')* is the inner radius (measured in degrees, °) in which I free the normalisation of all sources within it and the column labelled *free_sources(d=)*to allow for the Point Spread Function of front and back converting photon events down to 100 MeV. I have chosen these radii based on the number of objects close by to the GC because sources closest to the GC are likely to significantly influence the overall fit.

6.3 Spectral Analysis of each GC

6.3.1 Producing a Spectral Energy Distribution

The *sed()* method by default fits the overall spectral shape defined in the model file (from the *Fermi* 4FGL-DR2 catalogue [24]), this provides a good indication of spectral shape but is not precise enough for a full analysis. I will therefore follow the same procedure I described in Chapter 5, I will then fit the GC spectrum (integrated over 13 years) using the different spectral models listed in Section 2.1.3. In each SED, I have chosen to include all bins with a TS $>$ 16 and bins with a TS $<$ 16 are shown as 95% confidence level upper limits.

6.4 Results

6.4.1 ω Centauri

Figure 6.1a shows ω Centauri's spectrum integrated over 13 years. ω Centauri's can be seen to have significant curvature at around 1000 MeV so a PL is not going to be a good fit. ω Centauri is not only a bright GC in gamma-rays but is also one of the largest Galactic GC and was first discovered optically in 1677, it also appears to have a different chemical composition and unusual stellar velocity dispersion compared to other GC [100].

[2] As mentioned previously the TS value (test significance) is the difference in log-likelihoods between two different models:

$$TS = 2\log\left(\frac{L_1}{L_0}\right)$$

in this case, L_1 is the maximum likelihood of the model with a particular source and L_0 is the maximum likelihood of the model *without* that source. For one degree of freedom $\sigma = \sqrt{TS}$. In short, it is a way of quantifying how likely it is that the gamma-ray emission is emitted from a particular source.

Parameters and SED's for Different Spectral Models

Tables 6.2 and 6.3 give the parameters for the best spectral fit of the LP and PLExp models to ω Centauri's spectrum. The parameters for both models are described in Section 2.1.3. Figure 6.1 shows ω Centauri's spectrum fitted with each of the models.

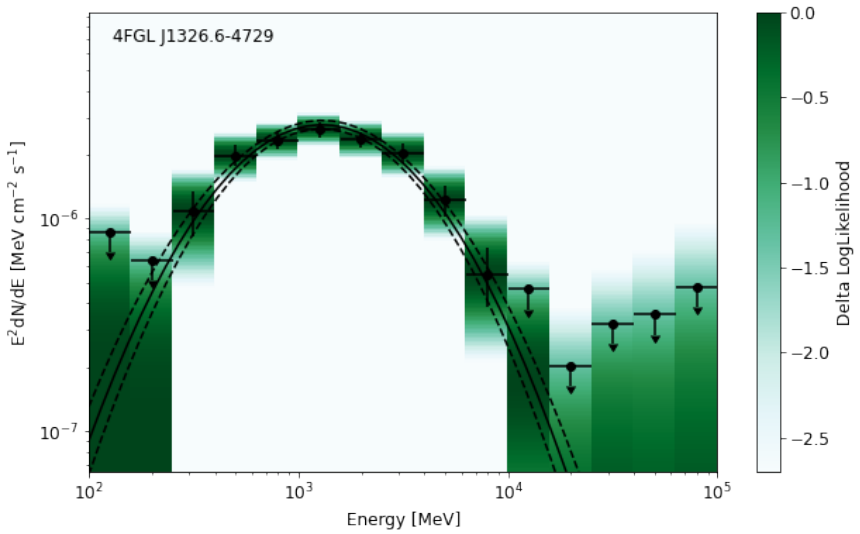

(a) ω Centauri's spectrum fitted with a LP model, the parameters for this spectral shape are given in Table 6.2.

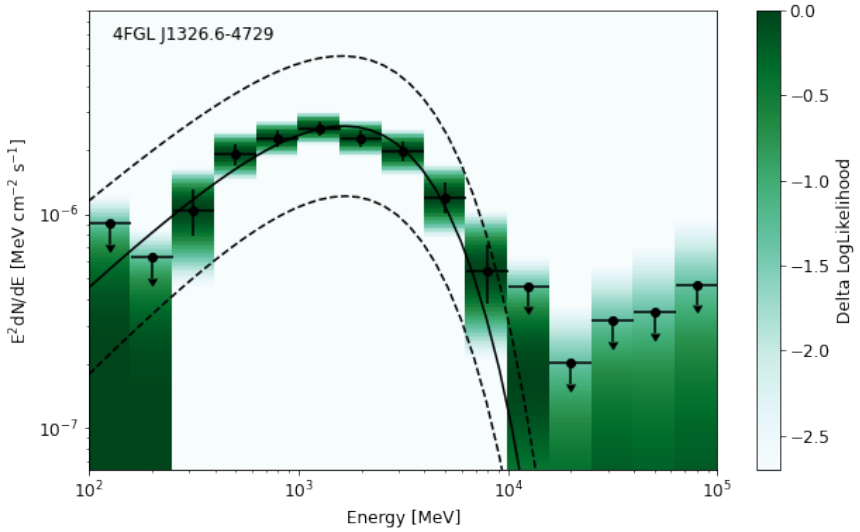

(b) ω Centauri's spectrum fitted with a PLExp model, the parameters for this spectral shape are given in Table 6.3.

Figure 6.1: The error bars on both plots show 1σ uncertainty on $E^2 \frac{dN}{dE}$ and are evaluated from the likelihood curvature. Spectral bins with a $TS < 16$ are marked as 95% confidence level upper limits which are evaluated from the profile likelihood.

Parameter	Value
N_0 ($\mathrm{MeV}^{-1}\mathrm{cm}^{-2}\mathrm{s}^{-1}$)	$(9.73 \pm 0.48) \times 10^{-13}$
α	2.26 ± 0.07
β	0.522 ± 0.063
E_b (MeV)	1660

Table 6.2: The parameters for the best fit LP to ω Centauri's spectrum. The functional form is described in equation 2.2.

Parameters	Value
N_0 ($\mathrm{MeV}^{-1}\mathrm{cm}^{-2}\mathrm{s}^{-1}$)	$(2.87 \pm 2.81) \times 10^{-11}$
γ_1	-1.26 ± 0.04
E_0 (MeV)	1.0×10^4
E_c (MeV)	15.2 ± 0.1
γ_2	1

Table 6.3: The parameters for the best fit PLExp to ω Centauri's spectrum. The functional form is described in equation 2.4.

Statistical Comparison of the Different Spectral Models

Model	Log-likelihood	AIC	ΔAIC
LP	1598142.221	-1598136.221	0
PLExp	1598139.100	-1598133.100	3.121

Table 6.4: Comparison of different spectral models for ω Centauri, ranked from best to worst (ordered by ascending AIC statistic). Δ AIC is the difference between the best fit model and the AIC of that model. The AIC indicates that the LP is a better model than the PLExp to ω Centauri's spectrum.

Spectral models being compared	TS
LP vs. PLExp	6.24

Table 6.5: A comparison of the fit of the LP and PLExp models to ω Centauri's spectrum. The TS is the statistical significance that a model is preferred over the other (as defined in equation 5.6). The TS indicates that it is not possible to distinguish statistically between the LP and PLExp models.

Discussion of Findings

The LP is preferred over the PLExp with a TS = 6.24, which indicates that it is not possible to distinguish statistically which model is preferred over the other. However, the AIC suggests that the LP is a better model of the spectrum than PLExp with a difference (ΔAIC = 3.12) which is deemed significant. This difference in findings between the TS and AIC is because the AIC also accounts for the number of degrees of freedom in each model. I note that the PLExp fit shown in Figure 6.1b is not consistent with the upper limit given in the lowest energy bin and the 1σ uncertainty on the PLExp is significantly wider than the 1σ uncertainty on the LP (shown as the dotted lines). These observations would suggest that the LP model better describes ω Centauri's spectrum. Each spectral bin between 500 MeV and 5000 MeV in Figure 6.1 has a TS > 85 which demonstrates that the majority of the emission is in this energy range (and confirms again that ω Centauri is a bright GC), this is important because it tells us that understanding the

emission outside of this energy range is crucial to determining the preferred spectral shape, and better measurements are needed to do this.

Previous studies of ω Centauri with *Fermi*-LAT in [39] detected the GC with a TS = 944 whereas I detected ω Centauri with a TS = 1215, the higher TS in my analysis is likely due to the longer exposure period of 13 (rather than 10) years. The previous study in [39] fitted the spectrum using a LP model but did not compare to a PLExp. It is possible that the fit in my analysis is better because of the greater detection significance.

ω Centauri has also been studied at other wavelengths. Radio observations have led to the discovery of (at the time of writing) 15 MSP [51, 55] within the GC. Given that my analysis suggests the LP model appears a better fit than the PLExp, this could indicate that ω Centuari's emission may not be entirely due to MSPs, and there may well be several sources of gamma-ray emission in this GC. There have been several studies investigating the possibility that ω Centuari may have contain a significant dark matter component (such as [39] investigating the gamma-ray emission and [120] investigating at radio wavelengths).

6.4.2 47 Tuc

Every bin in 47 Tuc's spectrum (shown in Figure 6.2) that is not labelled as an upper limit had a TS > 21. This demonstrates that there is significant emission over a larger energy range (between 100 MeV and 9000 MeV) than ω Centauri and also that 47 Tuc is much brighter than ω Centauri).

Parameters and SED's for Preferred Spectral Model

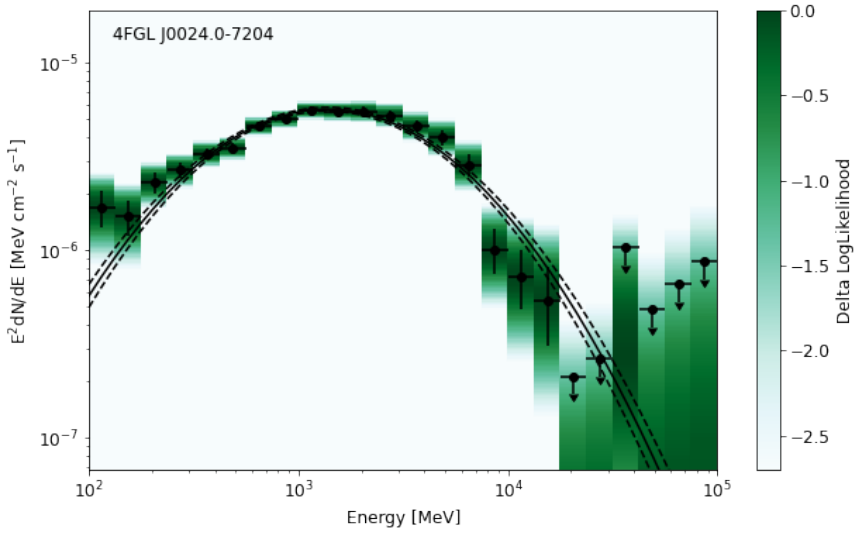

Figure 6.2: 47 Tuc's spectrum fitted with a power law with exponential cut-off. The parameters for the shape are given in Table 6.6. The error bars on both plots show 1σ uncertainty on $E^2 \frac{dN}{dE}$ and are evaluated from the likelihood curvature. Spectral bins with a $TS < 16$ are marked as 95% confidence level upper limits which are evaluated from the profile likelihood.

Parameter	Value
N_0 ($\mathrm{MeV}^{-1}\mathrm{cm}^{-2}\mathrm{s}^{-1}$)	$(3.40 \pm 0.47) \times 10^{-13}$
γ_1	-1.32 ± 0.05
E_0 (MeV)	1000
γ_2	1
E_c (MeV)	2760 ± 200

Table 6.6: Parameters for best fit power law with PLExp for 47 Tuc

Statistical Comparison of the Different Spectral Models

Model	Log-likelihood	AIC	Δ AIC
PLExp	-116787.111	116793.111	0
LP	-116799.802	116805.802	12.691

Table 6.7: Table of log-likelihood values when fitting different spectral forms for 47 Tuc. The models have been listed in order of ascending AIC, this order indicates how well the models fit the data (from best to worst). The AIC indicates that the PLExp is a better model than the LP to 47 Tuc's spectrum.

Spectral models being compared	TS
PLExp vs. LP	25.4

Table 6.8: A comparison of the fit of the PLExp and LP models to 47 Tuc's spectrum. The TS is the statistical significance that a model is preferred over the other (as defined in equation 5.6). The TS indicates that the PLExp is preferred over the LP with some significance.

Discussion of Findings

Overall, the PLExp is preferred over the LP, with a TS = 25. Both models have three free parameters and consequently the AIC also indicates that the PLExp is a better model. This is in contrast with findings by Brown et al. in [40] where the spectrum was found to be best described by a LP (using 7.5 years of data). However the best fitting PLExp had a $\gamma_1 = -1.21 \pm 0.06$ and a cut-off energy, $E_c = 2400 \pm 200$ MeV which is consistent with the uncertainties on the parameters shown in Table 6.6. The difference in findings may well be due to the more refined binning used in my analysis (which is possible over a longer analysis period, as the better photon statistics enable smaller energy binning). However, other studies such as [4] also found a PLExp was the best fit model, which led to the assumption that the observed emission from 47 Tuc was due to MSPs.

Unlike ω Centauri, 47 Tuc has statistically significant emission below 200 MeV. Whilst this finding might be partly because ω Centauri has a smaller overall detection significance and is fainter than 47 Tuc, it could also suggest there are some fundamental differences between these GC. They could well have evolved differently: there is substantial evidence that ω Centauri evolved from a dwarf galaxy [27, 32]. There is also possible evidence of an intermediate mass black hole in 47 Tuc [79]. To determine whether there is any significant emission below 200 MeV, observations would be needed using a different instrument to *Fermi*-LAT [3].

[3] Whilst *Fermi*-LAT can in principle detect photons of energies as low as 20 MeV, the energy resolution is poor at low energies and more sensitive instruments would be needed to significantly detect this lower energy emission

6.4.3 NGC 7078

NGC 7078 is a much fainter GC compared to 47 Tuc and ω Centauri and consequently there are fewer statistically significant energy bins in the spectrum (Figure 6.3). The smaller number of bins means it is more difficult to determine whether or not the spectrum has curvature and I have therefore compared the PL as well as PLExp and LP spectral models.

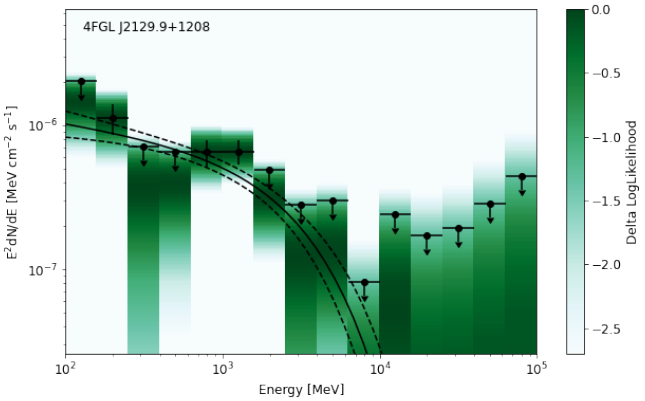

(a) Best PLExp fit to NGC 7078's spectrum. The parameters for the fit are given in Table 6.11.

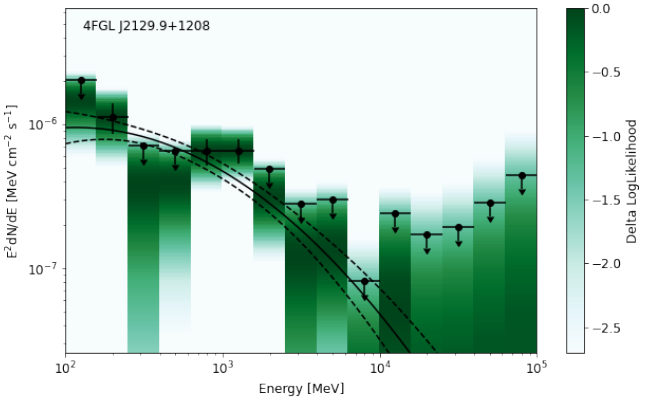

(b) Best LP fit to NGC 7078's spectrum. The parameters for the fit are given in Table 6.10.

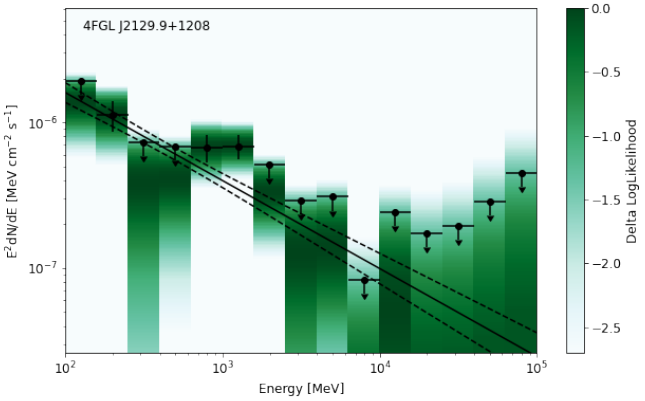

(c) Best PL fit to NGC 7078's spectrum, parameters listed in Table 6.9.

Figure 6.3: Comparison of different spectral models to NGC 7078's spectrum. The error bars on both plots show 1σ uncertainty on $E^2 \frac{dN}{dE}$ and are evaluated from the likelihood curvature. Spectral bins with a $TS < 16$ are marked as 95% confidence level upper limits which are evaluated from the profile likelihood.

Parameter	Value
N_0 ($\mathrm{MeV}^{-1}\mathrm{cm}^{-2}\mathrm{s}^{-1}$)'	$(1.33 \pm 0.14) \times 10^{-12}$
γ_1	-2.60 ± 0.09
E_0 (MeV)	630 ± 11

Table 6.9: The parameters for the best fit PL to NGC 7078's spectrum.

Parameter	Value
N_0 ($\mathrm{MeV}^{-1}\mathrm{cm}^{-2}\mathrm{s}^{-1}$)	$(9.20 \pm 1.25) \times 10^{-12}$
α	2.28 ± 0.22
β	0.420 ± 0.088
E_b (MeV)	300

Table 6.10: Parameters for best fit LP to NGC 7078's spectrum.

Parameter	Value
N_0 ($\mathrm{MeV}^{-1}\mathrm{cm}^{-2}$)	$(7.16 \pm 2.40) \times 10^{-13}$
γ_1	-2.17 ± 0.25
E_0 (MeV)	1000
E_c (MeV)	2840 ± 1790
γ_2	1

Table 6.11: Parameters for best fit PLExp to NGC 7078's spectrum

Statistical Comparison of the Different Spectral Models

Model	Log-likelihood	AIC	Δ AIC
PLExp	287883.124	-287877.124	0
LP	287881.648	-287875.648	1.476
PL	287879.711	-287875.711	1.413

Table 6.12: Table of log-likelihood values when fitting different spectral forms for NGC 7078. A larger log-likelihood value indicates a better fit. A lower AIC indicates which model is best overall. The ΔAIC is the difference between the AIC of the 'best' model and a given model. The AIC indicates that it is not possible to determine which of the models being compared here is preferred.

Spectral models being compared	TS
PLExp vs. PL	6.83
PLExp vs. LP	2.95
LP vs. PL	3.87

Table 6.13: A comparison of the fit of the PLExp, LP and PL models to NGC 7078' spectrum. The TS is the statistical significance that a model is preferred over the other (as defined in equation 5.6). The TS values indicate that the three models are very similar.

Discussion of Findings

The TS values in Table 8.6 demonstrate that the PL, PLExp, LP models cannot be statistically distinguished. The AIC values in Table 6.12 also imply that none of the models being compared are a significantly better fit to the spectrum. Previous studies of NGC 7078 in [88] (8 years of data) and [133] (over a 12 year period) found a PL to be the

best spectral model for NGC 7078. The statistical indistinguishability between the PL and curved (LP/PLExp) spectral models in my analysis could suggest that there may be some curvature in NGC 7078's spectrum which has only become apparent because I have a longer analysis period and therefore better photon statistics. On the other hand, I note that there are only 3 spectral bins that are statistically significant (bins that are not labelled as upper limits) and only two energy bins have a TS > 25 [4]. For these reasons it is not surprising that none of the spectral models are good descriptions of NGC 7078's spectrum. NGC 7078 was detected with significance (TS) of 112, the lowest significance of all the GC I have analysed.[5] NGC 7078 is the most distant (10.4 kpc) and faintest GC I have analysed so this is not surprising, however the fact that significant emission only appears in 3 spectral bins suggests that this GC is very different to the other GC I have studied. This may indicate that there are some fundamental differences in the origin of the emission from these GC and they may have evolved differently. Further studies at lower energies would be needed to better understand the origin of this emission.

We know that there are MSPs within NGC 7078 (8 MSPs have so far been detected within the GC [75]). If MSPs are the dominant emitters in NGC 7078, we would expect to see some evidence of spectral cut off. We observe a lack of significant emission above 500 MeV where all the bins are upper limits, this could suggest spectral cut-off but it is not conclusive and no gamma-ray emission has currently been detected from any individual MSP. Further studies are needed to improve our understanding of NGC 7078's gamma-ray emission.

[4] which corresponds to a significance of 5σ because the emission in each bin has one degree of freedom
[5] The detection significance that each GC has been detected with (TS) is given in Table 6.25.

6.4.4 NGC 6752

NGC 6752 has a similar energy flux to NGC 7078 however it is much closer (only 4 kpc away compared to 10.8 kpc). NGC 6752's spectrum also has a definite curvature (this curvature is also observed for 47 Tuc and ω Centauri)and therefore the PL model is not going to be a good fit to the spectrum.

Parameters and SED's for Different Spectral Models

Parameter	Value
N_0 ($\mathrm{MeV}^{-1}\mathrm{cm}^{-2}\mathrm{s}^{-1}$)	$(6.38 \pm 0.62) \times 10^{-13}$
α	2.03 ± 0.15
β	0.731 ± 0.176
E_b (MeV)	1250

Table 6.14: Parameters for best fit LP to NGC 6752's spectrum.

Parameter	Value
N_0 ($\mathrm{MeV}^{-1}\mathrm{cm}^{-2}\mathrm{s}^{-1}$)	$(2.09 \pm 0.62) \times 10^{-12}$
γ_1	-0.740 ± 0.365
E_0 (MeV)	1000
E_c (MeV)	1130 ± 307
γ_2	1

Table 6.15: Parameters for best fit PLExp to NGC 6752's spectrum.

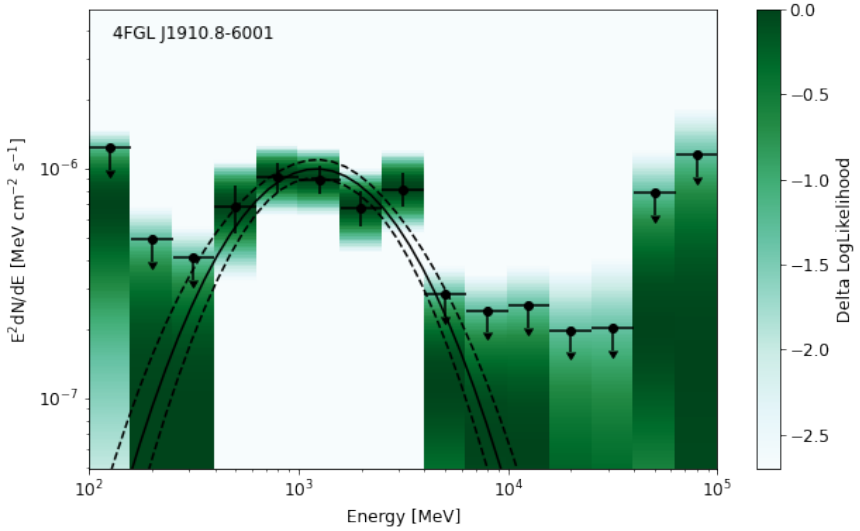

(a) LP best fit to NGC 6752's spectrum,parameters listed in Table 6.14.

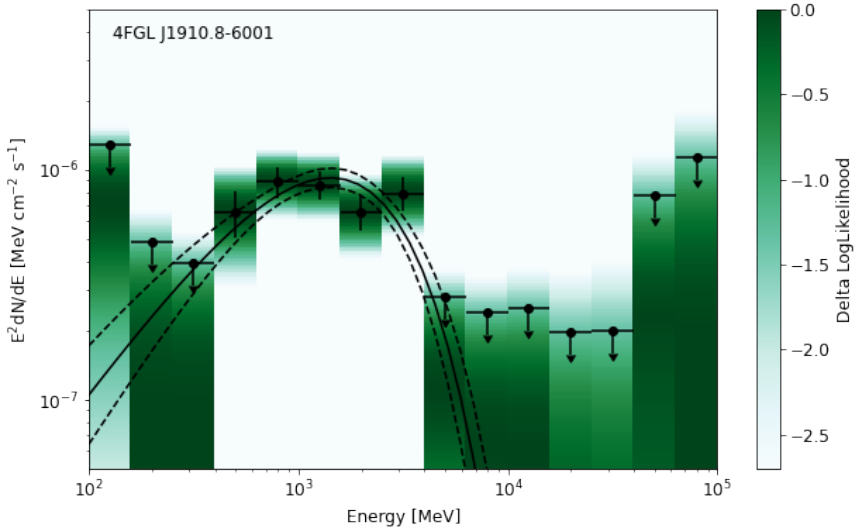

(b) PLExp fit to NGC 6752's spectrum, parameters listed in Table 6.15.

Figure 6.4: Comparison of different spectral models to NGC 6752's spectrum. The error bars on both plots show 1σ uncertainty on $E^2 \frac{dN}{dE}$ and are evaluated from the likelihood curvature. Spectral bins with a $TS < 16$ are marked as 95% confidence level upper limits which are evaluated from the profile likelihood.

Statistical Comparison of the Different Spectral Models

Model	Log-likelihood	AIC	Δ AIC
LP	201764.713	-201758.713	0
PLExp	201764.489	-201758.489	0.224
PL	201739.447	-201735.447	23.266

Table 6.16: Table of log-likelihood values when fitting different spectral forms for NGC 6752. A larger log-likelihood value indicates a better fit, whereas a lower AIC indicates a better fitting model. The column Δ AIC is the difference between the model with the lowest AIC statistic and that model. The AIC indicates that the LP and PLExp are better models than the PL to NGC 6752's spectrum and that the LP and PLExp are equally good fits.

Spectral models being compared	TS
PLExp vs. PL	50.1
LP vs. PLExp	0.4
LP vs. PL	50.5

Table 6.17: A comparison of the fit of the PLExp, LP and PL models to NGC 6752's spectrum. The TS is the statistical significance that a model is preferred over the other (as defined in equation 5.6). The TS values indicate that the PLExp and LP are preferred significantly over the PL.

Discussion of Findings

Tables 8.8 and 6.16 show the LP and PLExp models cannot be statistically distinguished. This is likely because these models have a similar shape, and the photon statistics for this GC are not sufficient to distinguish them. NGC 6752 was first detected with a PL spectrum [124] and studies by [88] also fitted NGC 6752's spectrum with a PL (as defined in equation 2.3) (using 8 years of data). My analysis of 13 years of observations indicates that NGC 6752 has distinct curvature and that a spectral model with curvature is preferred: the LP and PLExp are both preferred significantly over the PL with a TS > 50 .

Figure 6.4 shows there is no significant detection below 200 MeV. More observations at below 200 MeV and X-ray observations would be needed to determine the existence and the profile of this lower energy emission.

The lack of significant emission above 4 GeV has been observed in previous studies [88]). These upper limits could hint at there being spectral cut-off (but the photon statistics are not large enough to observe it).

6.4.5 NGC 6441

A previous study of NGC 6441 with *Fermi*-LAT [124] found a gamma-ray source next to the NGC 6441 (a source which was outside the tidal radius, meaning that the emission could not be confirmed to be originating from the GC). However, subsequent studies have confirmed that there is indeed emission within the tidal radius of NGC 6441 and the GC is a significant source [14]. The spectrum of NGC 6441 has significant curvature and I have therefore chosen to compare the LP and PLExp spectral models.

Parameters and SED's for preferred model(s)

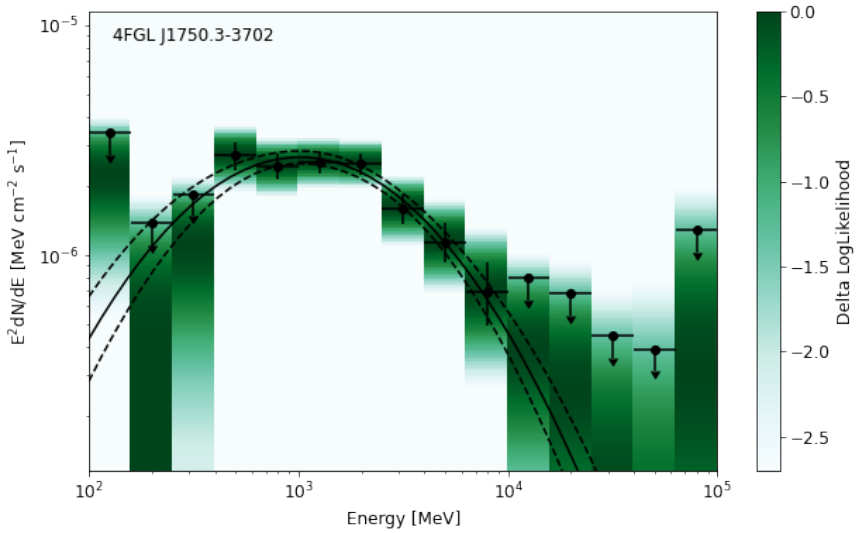

(a) Best LP fit to NGC 6441's spectrum. The error bars on both plots show 1σ uncertainty on $E^2 \frac{dN}{dE}$ and are evaluated from the likelihood curvature. Spectral bins with a $TS < 16$ are marked as 95% confidence level upper limits which are evaluated from the profile likelihood.The parameters for the fit are given in Table 6.18.

Parameter	Value
N_0 (MeV^{-1}cm^{-2}s^{-1})	$(1.83 \pm 0.04) \times 10^{-12}$
α	2.11 ± 0.03
β	0.337 ± 0.021
E_b (MeV)	1204

Table 6.18: The parameters for the LP fit to NGC 6441's spectrum.

Statistical Comparison of the Different Spectral Models

Model	Log-likelihood	AIC	Δ AIC
LP	7224556.261	-7224550.261	0
PLExp	7224545.320	-7224539.320	10.941

Table 6.19: Table of log likelihood values when fitting different spectral forms for NGC 6441. A larger log likelihood value indicates a better fit, whereas a lower AIC indicates a better fitting model. The AIC implies that the LP is a better model than the PLExp to NGC 6441's spectrum.

Spectral models being compared	TS
LP vs. PLExp	21.9

Table 6.20: A comparison of the fit of the PLExp, LP models to NGC 6441's spectrum. The TS is the statistical significance that a model is preferred over the other (as defined in equation 5.6). The TS value implies the LP is preferred over the PLExp.

Discussion of Findings

A LP model is preferred over PLExp with a TS = 22 and a ΔAIC = 11 and I therefore conclude that the LP is the best fit model to NGC 6441's spectrum. A previous study of NGC 6441 in [124] (with 2 years of data and consequently less refined energy binning) found a PLExp model was preferred over a PL model. The difference in preferred spectral model found in [124] and my analysis may well be because of the improved photon statistics using 13 (rather than 2) years of data.

6.4.6 Terzan 5

Terzan 5 is the brightest GC detected with *Fermi*-LAT and has an energy flux around 4 times larger than 47 Tuc (the next brightest). However unlike 47 Tuc, Terzan 5 is much closer to the Galactic Plane.

Parameters and SED's for Different Spectral Models

Parameter	Value
N_0 ($\mathrm{MeV}^{-1}\mathrm{cm}^{-2}\mathrm{s}^{-1}$)	$(7.460 \pm 0.151) \times 10^{-12}$
α	2.19 ± 0.02
β	0.286 ± 0.016
E_b (MeV)	1460

Table 6.21: The parameters for the best fit LP model to Terzan 5's spectrum.

Parameter	Value
N_0 ($\mathrm{MeV}^{-1}\mathrm{cm}^{-2}\mathrm{s}^{-1}$)	$(4.676 \pm 1.169) \times 10^{-13}$
γ_1	-1.61 ± 0.09
E_0 (MeV)	10000
E_c (MeV)	3620 ± 546
γ_2	1

Table 6.22: The parameters for the best fit PLExp model to Terzan 5's spectrum.

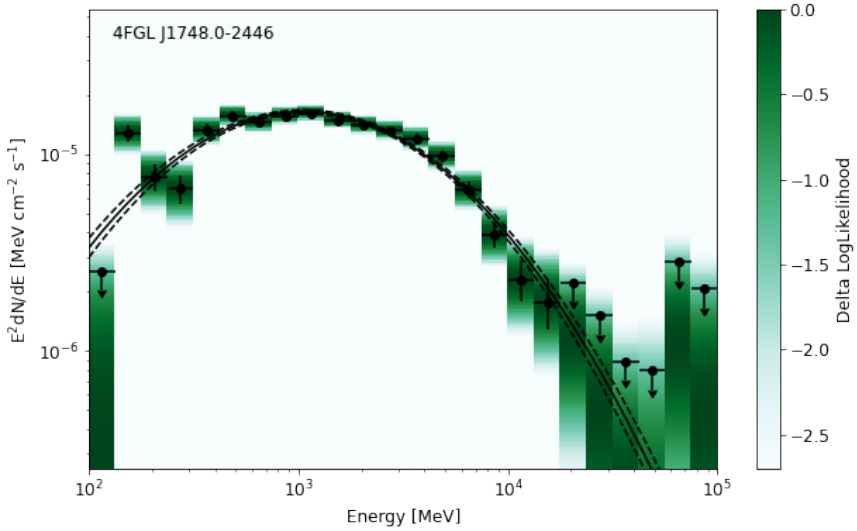

(a) LP fit of SED for Terzan 5, with parameters shown in Table 6.21.

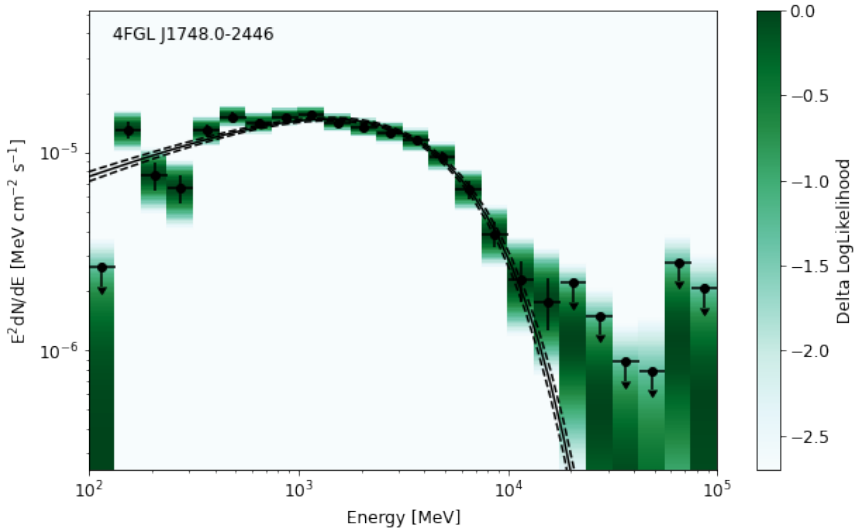

(b) PLExp fit of SED for Terzan 5, with parameters are in Table 6.22.

Figure 6.6: Comparison of Log Parabola and Power Law with exponential cut-off to Terzan 5's spectrum. The error bars show 1σ uncertainty on $E^2 \frac{dN}{dE}$ from the likelihood curvature. Spectral bins with a $TS < 16$ are marked as 95% confidence level upper limits which are evaluated from the profile likelihood.

Statistical Comparison of the Different Spectral Models

Model	Log likelihood	AIC	Δ AIC
LP	24527991.958	-24527985.958	0
PLExp	24527982.378	-24527976.378	9.580

Table 6.23: Table of log likelihood values and AIC for LP and PLExp found when fitting these different models to Terzan 5's spectrum. A larger log likelihood value indicates a better fit, whereas a lower AIC indicates a better fitting model. The column Δ AIC is the difference between the model with the lowest AIC statistic and that model. The AIC implies that the LP is a better model than the PLExp to Terzan 5's spectrum.

Spectral models being compared	TS
LP vs. PLExp	19.2

Table 6.24: A comparison of the fit of the PLExp, LP models to Terzan 5's spectrum. The TS is the statistical significance that a model is preferred over the other (as defined in equation 5.6). The TS values indicate the LP is preferred over the PLExp.

Discussion of Findings

The LP model is preferred over PLExp with a TS = 19 and a ΔAIC = 9.58. There is tension between the LP model and the spectrum at lower energies with emission between 150 MeV-300 MeV not being consistent with either the LP or PL models. Additionally, the second lowest energy bin (with median energy 154 MeV), which has a considerably higher flux than either the LP or PLExp models allow for, and this bin has high significance (TS> 97). This discrepancy may be due to the fact that Terzan 5 has a low Galactic latitude compared to other GC in my sample. Previous analysis of Terzan 5 in [80] and [2] had found that the energy spectrum is best described using a PLExp model with a cut off energy of 3.8 GeV and index of 1.9, both of which are within the uncertainties of the best fit PLExp model found in my analysis (for this reason, I have included the SED of Terzan 5 fitted with a PLExp model in Figure 6.6b as well as the LP, even though it is a poorer model). The authors of [80] concluded that the gamma-ray emission was most likely caused by the population of MSPs, however if a LP is indeed a better fit to Terzan 5's spectrum then this might imply that there are significant other sources of gamma-ray emission within Terzan 5.

Studies of the MSP population in [108] have concluded that Terzan 5 is unlikely to have evolved from a Dwarf Galaxy unlike 47 Tuc. Lower energy flux has been observed to be higher close to the Galactic plane. On the other hand, *Fermi*-LAT (and other current gamma-ray telescopes are far less sensitive to emission between 0.1 MeV-100 MeV [36]. It may be that this lower energy emission is being observed here.

Terzan 5 is also the only GC from which emission above 1 TeV has been detected in its vicinity using the ground-based HESS gamma-ray telescope in Namibia in 2011 [12], and a chance coincidence detection is unlikely (since no other likely coincidences for the VHE emission are known in the vicinity of Terzan 5), so it is most likely that this emission originates from the GC. A comparison of the VHE emission detected by HESS and the differential flux ($\frac{dN}{dE}$, photons per MeV) found in my *Fermi*-LAT analysis is shown in Figure 6.7. The VHE emission detected by HESS is fitted using a power law (equation 2.3), and my *Fermi*-LAT spectrum is fitted with a Log Parabola (equation 2.2). It is clear from Figure 6.7 that the power-law spectral model suggested by HESS in [12] is not consistent with the spectral points found to have upper limits in my *Fermi*-LAT analysis. Additionally, the VHE emission detected by HESS is not consistent with the Log Parabola spectral model. These discrepancies would imply that more than one source may be responsible for the gamma-ray emission observed from Terzan 5, and this is supported by findings in [12] because the VHE appears to be extended and off-set from the core of Terzan 5. Whilst a MSP is capable of emitting at these energies, it would not be an extended source and notably no high energy emission has been detected from any other GC. This would suggest that there may well be some additional processes occurring in Terzan 5 that are not present in other GC. Most GC are gas poor, but one hypothesis for the VHE emission is some shot-up gas in Terzan 5.

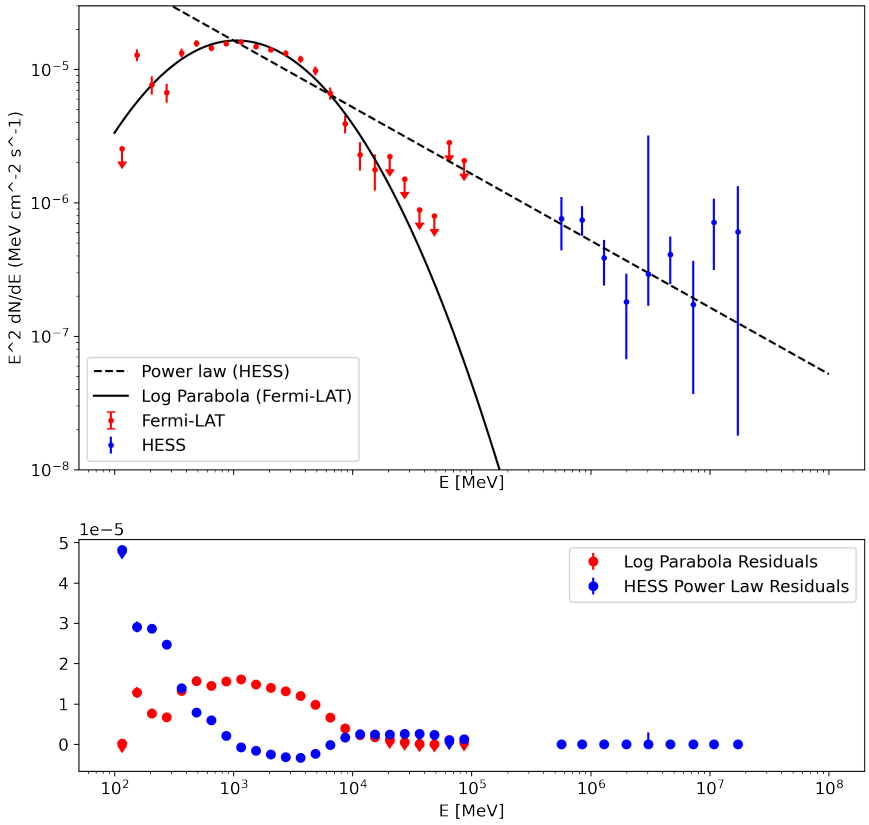

Figure 6.7: A comparison of the gamma-ray flux detected by *Fermi*-LAT (shown in red) and HESS (shown in blue from [12]) above 10 GeV. The error bars on the HESS points are 1σ error bars and fitted with a Power Law model. The error bars on the *Fermi*-LAT points are the 1σ errors on each spectral band. The LP model is characterised by the parameters shown in Table 6.23. The Power Law model (as defined in equation 2.3) has a normalisation $(5.2 \pm 1.1) \times 10^{-13}$ cm^{-2}s^{-1}TeV^{-1}, spectral index of $2.5 \pm 0.3 \pm 0.2$ (the statistical and systematic uncertainties) and a scale energy of 1 TeV. The residual plot shows the difference between the spectral points (measured by *Fermi*-LAT and HESS) and the Log Parabola best fit model (from my analysis, shown as the red residuals) and the Power Law model (from [12] shown as the blue residuals). The Log Parabola model predicts significantly lower energy fluxes at high energies, and therefore the residuals are small for the HESS spectral points.

6.4.7 Overall Analysis

In Table 6.25 I present the detected positions, test significance (TS), energy and photon fluxes for each GC in my selection derived from a full thirteen year analysis. NGC 7078 is anomalous in my sample of GC in that its spectrum cannot be modelled well by the PL, PLExp or LP models however this GC is by the faintest I have analysed and also has the fewest significant spectral bins.

GC	4FGL Name	Galactic Longitude (°)	Galactic Latitude (°)	TS	Npred	Photon Flux Model ($\times 10^{-9}$cm^{-2} s^{-1})	Energy Flux ($\times 10^{-6}$MeV cm^{-2} s^{-1})	Preferred Spectral shape
ω Cen	J1326.6-4729	309.078	-14.958	1215	3068	8.033 ± 0.808	6.765 ± 0.331	LP
47 Tuc	J0024.0-7204	305.902	-44.891	9217	7403	21.80 ± 1.08	17.0 ± 0.4	PLExp
NGC 6752	1910.8-6001	336.453	-25.636	299.2	904.8	2.347 ± 0.488	2.063 ± 0.200	LP
NGC 7078	J2129.9+1208	64.985	-27.319	112.2	2213	1.000 ± 0.129	2.613 ± 0.268	PL/PLExp/LP
NGC 6441	J1750-3702	353.547	-5.019	555.4	4081	1.265 ± 0.243	7.920 ± 0.648	LP
Terzan 5	J1748.0-2446	3.845	1.692	6347	27320	83.63 ± 3.76	52.48 ± 1.11	LP

Table 6.25: The detected Galactic longitudes (GLon) and latitudes (GLat), test significance's (TS), total photon count (Npred), photon fluxes and energy fluxes for each GC derived over thirteen year analysis. The analysis period is between (239557417 − 649784621MET) and the energy range of the analysis is 100 MeV - 100 GeV. Note that the Galactic latitude/longitude are the best fitted position following my analysis and may therefore differ slightly from those in the *Fermi* 4FGL catalogue, listed in Table 3.1. Note that the fitted values will depend on the spectral model used, the values in this table are for the preferred spectral model. Where two models cannot be statistically distinguished I have used the values for the model listed in the 4FGL Catalogue (which can be found in Table 3.1).

Chapter 7

Millisecond Pulsar Analysis

In this chapter I present the results of my analysis for evidence of pulsed emission from the GC I analysed in Chapter 6. Just like I did for NGC 6624 in Chapter 5, I produce phase-folded light-curves and conduct the H-test using ephemerides for MSP within each GC. I have obtained ephemerides from the discovery papers listed in [46] and also from the Australian Telescope National Facility (ATFN) pulsar catalog [1].

7.0.1 ω Centauri

There have been 15 MSP detected in ω Centauri, however 10 of these were discovered very recently and a full ephemerides is yet to be published [46]. The integrated radio pulse profiles of the 5 MSP found in [51] are shown in Figure 7.1, and I am able to look for evidence of pulsed emission using the ephemerides from these MSP.

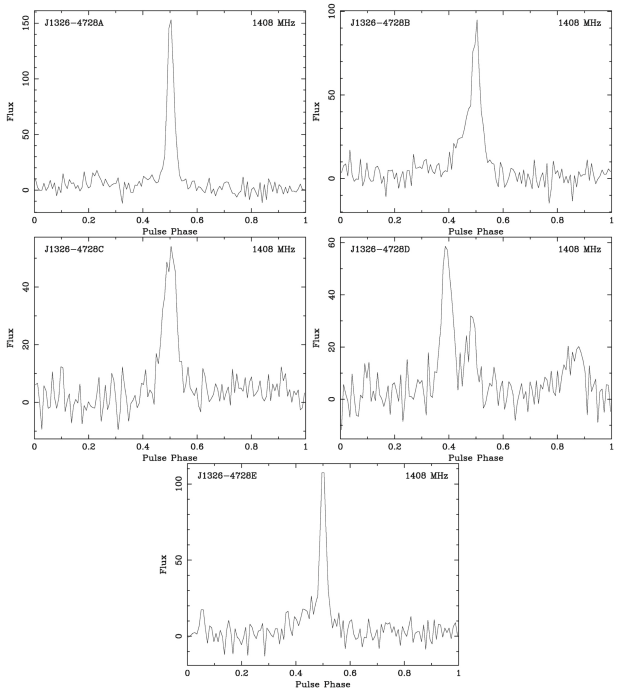

Figure 7.1: The integrated radio pulse profiles of 5 MSP detected within ω Centauri [51]. Each MSP has a large main pulse at around 0.5ϕ apart from MSP J1326-4728D which has a main pulse at 0.4ϕ and a weaker inter-pulse at 0.6ϕ.

[1] `https://www.atnf.csiro.au/research/pulsar/psrcat/`, accessed 25/06/22

Phase-Folded Light-Curves

By comparing the radio pulse profiles in Figure 7.1 and the gamma-ray phase-folded light-curves of each MSP in Figure 7.2 it is clear that there is no observable main pulse in the gamma-ray light-curve. This would suggest that no statistically significant pulsed emission is being detected from any of the MSPs (that can be seen above the background emission from the GC). In order to see if background emission is preventing the detection of pulsed emission from the light-curves, I tried removing background photons by cutting out photons with a probability $p < 0.66$ likelihood of originating from ω Centauri. Using a probability higher cut left insufficient photons to produce a light-curve. The light-curves containing photons with probability $p > 0.66$ are shown in Figure 7.3, however there is still no obvious pulsed emission.

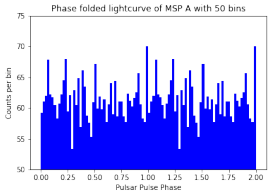

(a) MSP J1326-4728A

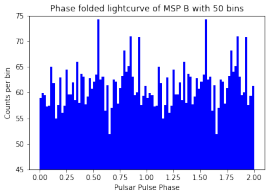

(b) MSP J1326-4728B

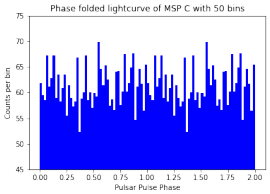

(c) MSP J1326-4728C

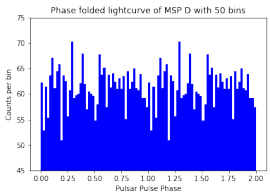

(d) MSP J1326-4728D

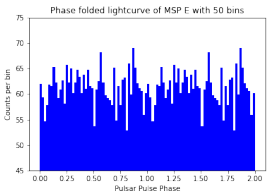

(e) MSP J1326-4728E

Figure 7.2: Phase-folded light-curves for MSP in ω Centauri. Light-curves have a bin width of 0.02ϕ which is the width of the pulse in the radio profile in [52].

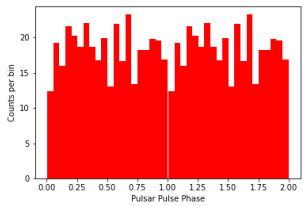

(a) MSP J1326-4728A

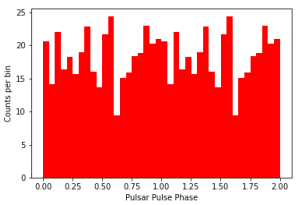

(b) MSP J1326-4728B

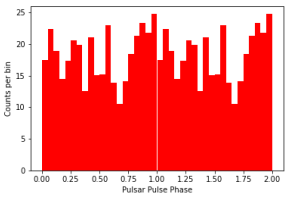

(c) MSP J1326-4728C

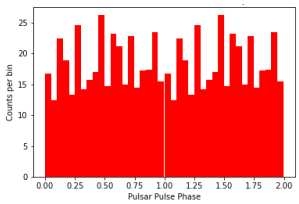

(d) MSP J1326-4728D

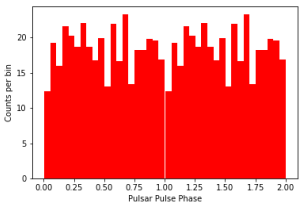

(e) MSP J1326-4728E

Figure 7.3: Phase folded light-curves for all detected MSPs in ω Centauri with a bin width of 0.02ϕ. The light-curve is produced using photon weights, and has had photons with $p < 0.66$ removed.

H-test

I also conducted the H-test as described in Section 4.5.2 and demonstrated for NGC 6624 in Chapter 5. Figure 7.4 shows the H-test over the energy range of 100 MeV- 100 MeV for each MSP in ω Centauri.

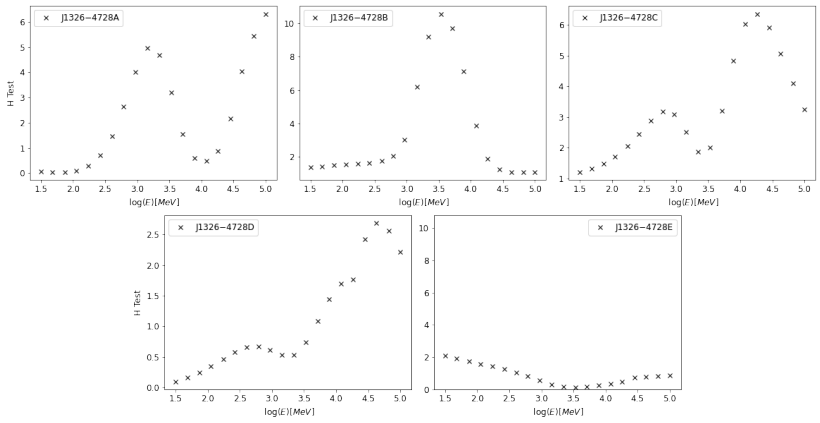

Figure 7.4: The H-test for 20 trial values of $\log(E_{ref})$ forfive MSP in ω Centauri. A bell-shaped curve and an $H > 25$ is expected from a gamma-ray MSP [16].

In the H-test result shown in Figure 7.4, MSP J1326-4728B is detected with the highest significance with a H-Test statistic (HTS) of 10.6 at an energy of 3.4 GeV (which is a typical energy for MSP emission to peak at and can be seen in the energy spectrum in the Xing+Wang MSP model shown in Figure 2.6), showing some evidence of pulsed gamma-ray emission at 3σ significance. All the other MSPs have been detected with a smaller HTS, which means there is insufficient evidence to suggest detected gamma-ray emission from any other MSP. It should be noted that MSP J1326-4728C, J1326-4728D, J1326-4728E do not yet have a full timing solution and therefore their position is the radio observatory pointing centre [52]. Figure 7.4 also shows that only MSP has a shape typical of a gamma-ray MSP, which could suggest that the other four MSPs may not be significant gamma-emitters. As no individual MSP can be detected in gamma-rays with high significance, this supports the hypothesis from [39] that the gamma-ray emission detected from ω Centauri cannot be explained solely by an ensemble of MSP.

7.0.2 47 Tuc

Phase-Folded Light-curves

Figure 7.5 show phase-folded light-curves for a subset of MSP in 47 Tuc. The photons have been weighted by their probability of originating from the GC. I have chosen a binning of 0.02ϕ after examining the radio pulse profiles in [61].

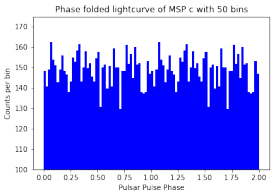

(a) J0023−7204C

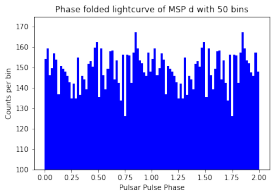

(b) J0023−7204D

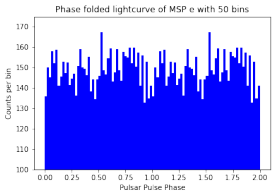

(c) J0023−7204E

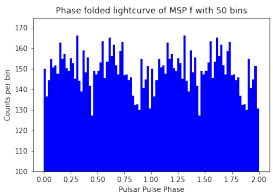

(d) J0023−7204F

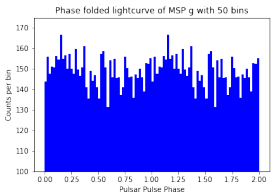

(e) J0023−7204G

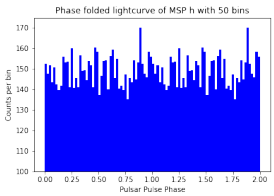

(f) J0023−7204H

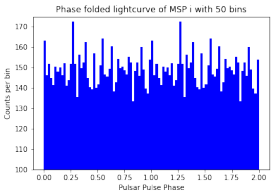

(g) J0023−7204I

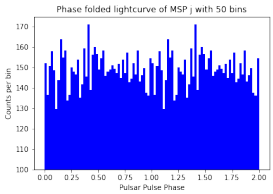

(h) J0023−7204J

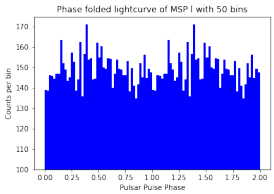

(i) J0023−7204L

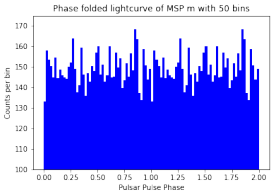

(j) J0023−7204M

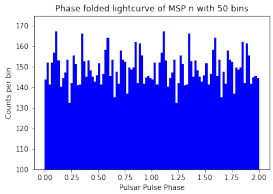

(k) J0023−7204N

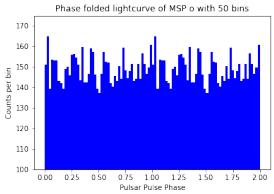

(l) J0023−7204O

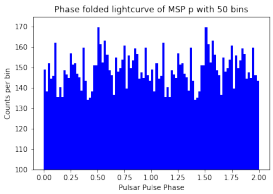

(m) J0023−7204Q

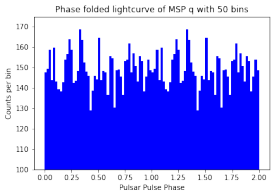

(n) J0023−7204R

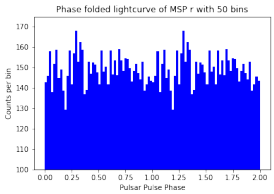

(o) J0023−7204S

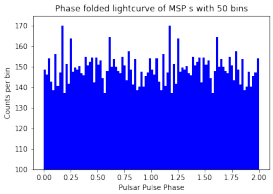

(p) J0023−7204T

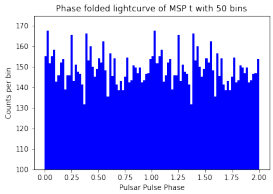

(q) J0023−7204U

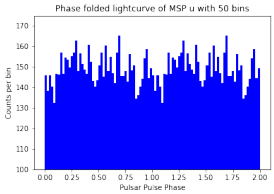

(r) J0023−7204W

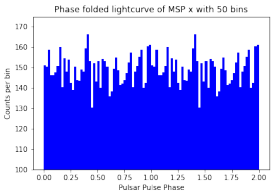

(s) J0023−7204X

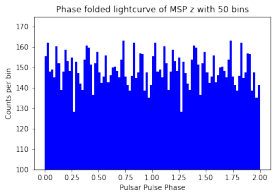

(t) J0023−7204Z

Figure 7.5: Phase folded light-curves for MSP detected in 47 Tuc. The weighted light-curves have a bin width of 0.02ϕ which is the width of the pulse in the radio profile in [52].

H-test

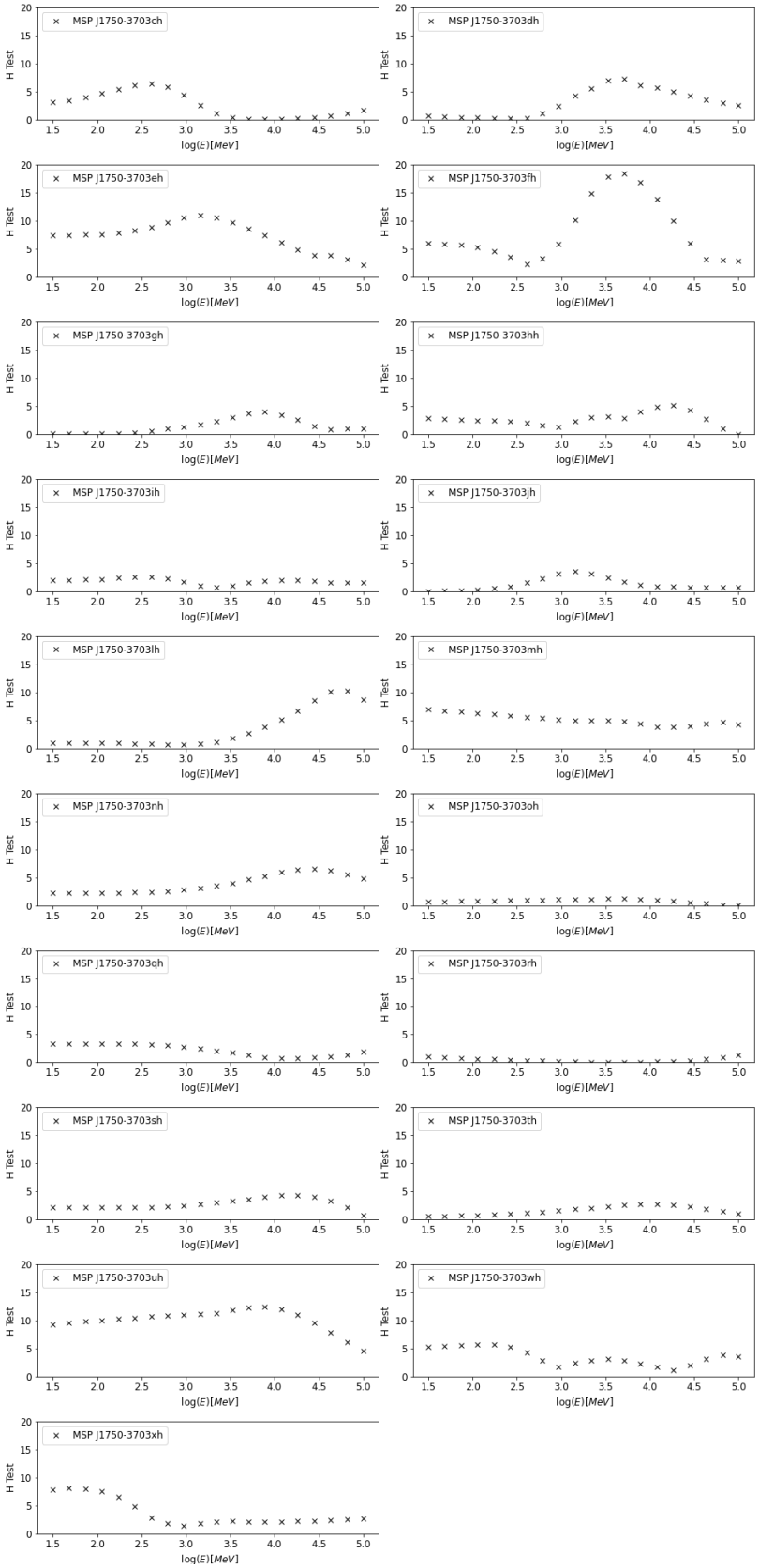

Figure 7.6: The H-test for 20 trial values of $\log(E_{ref})$ for some of the MSP in 47 Tuc. A bell-shaped curve and an $H > 25$ is expected from a gamma-ray MSP [16].

No significant pulsed emission can be observed from any of the MSP light-curves in 47 Tuc. Figure 7.6 shows evidence of pulsed emission with a HTS= 17.8 from one MSP and pulsed emission with a HTS > 10 for 2 other MSPs. However, this is not sufficient evidence for pulsed emission. Figure 7.6 also shows that many of the MSPs do not have the typical 'bell-shape' expected for gamma-ray MSPs, which may also suggest that many of the MSP in 47 Tuc are not strong gamma-ray emitters. These findings imply that individual MSP in 47 Tuc are too faint to detect and may be evidence that not all of 47 Tuc's emission is from MSP, or perhaps that there is just no single MSP that is bright enough to be resolved individually (unlike in NGC 6624).

7.0.3 NGC 7078

Phase-Folded Light-curves

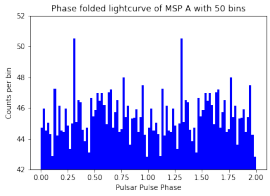

(a) B2127+11A

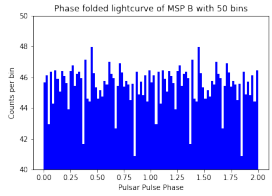

(b) B2127+11B

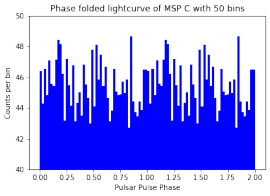

(c) B2127+11C

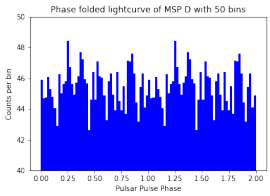

(d) B2127+11D

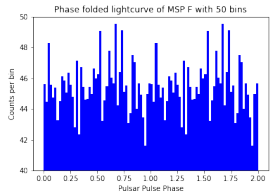

(e) B2127+11E

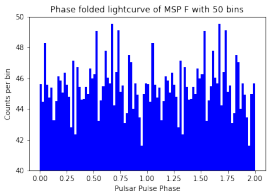

(f) B2127+11F

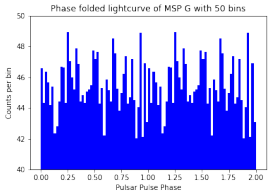

(g) B2127+11G

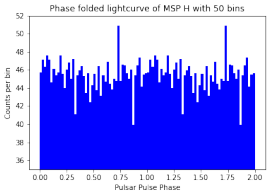

(h) B2127+11H

Figure 7.7: Phase folded light-curves for MSP detected in NGC 7078. The weighted light-curves have a bin width of 0.02ϕ which is the width of the pulse in the radio profile in [52].

Figure 7.7 shows one bin that appears to have more photons at around 0.4ϕ (in the light-curve of MSP B2127+11A) however, this is still not significant compared to the other bins. I also tried using a cut (using the probability from the GC as I did from ω Centauri) however this did not leave sufficient photons to produce a light-curve. This could imply that these MSP are faint gamma-ray emitters compared to NGC 7078 and are therefore not the dominant source of emission from this GC.

H-test

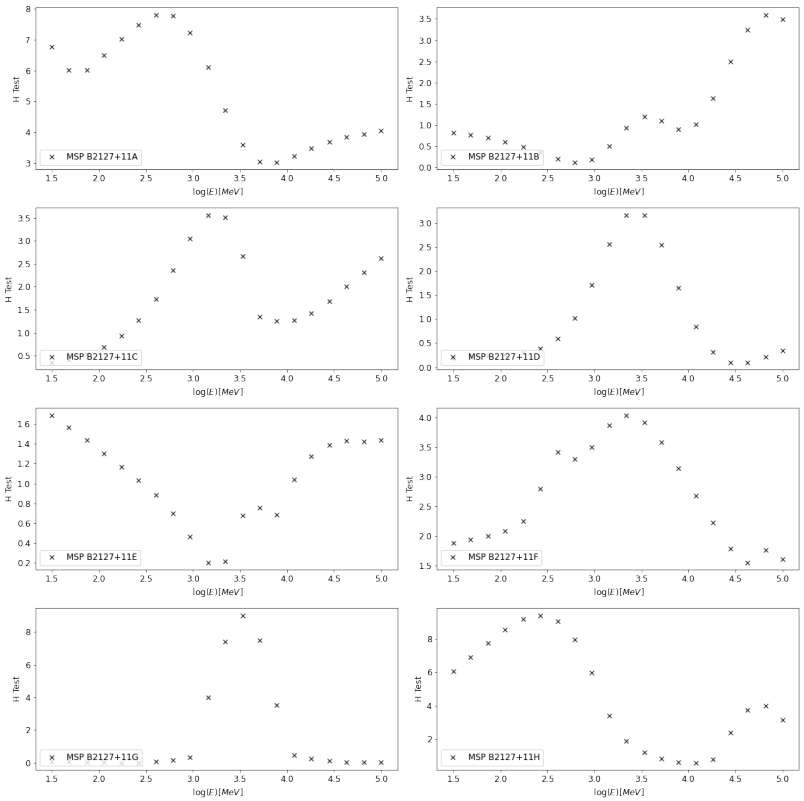

Figure 7.8: The H-test for 20 trial values of $\log(E_{ref})$ for all five detected MSPs in NGC 7078. A bell-shaped curve and an $H > 25$ is expected from a gamma-ray MSP [16].

No MSP was detected with an HTS > 10, which means there is no evidence of pulsed emission from any of the MSP in NGC 7078. This would suggest that the gamma-ray emission from the MSP in this GC is too faint to detect. Figure 7.8 demonstrates that some of the MSPs have the typical 'bell-curve' expected for a gamma-ray MSPs [41] but some of them do not, which could suggest that the gamma-ray emission is not only too faint to detect, but also that the gamma-ray emission from many of the MSP in this GC is different to the gamma-ray emission from MSP in the local Galactic neighbourhood.

7.0.4 NGC 6752

Phase-Folded Light-curves

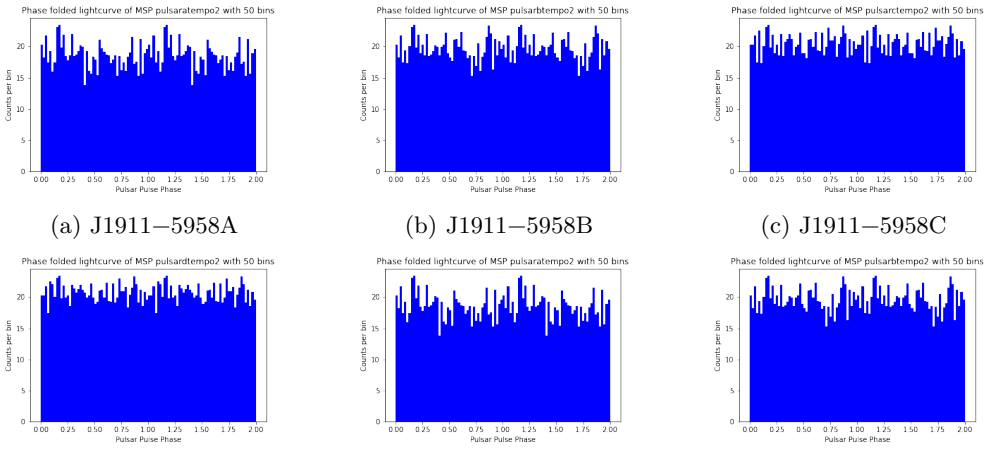

(a) J1911−5958A (b) J1911−5958B (c) J1911−5958C

(d) J1911−5958D (e) J1911−5958E (f) J1911−5958F

Figure 7.9: Phase folded light-curves for detected MSPs in NGC 6752. Light-curves have a bin width of 0.02ϕ which is the width of the pulse in the radio profile in [52]. The light-curve is produced using photon weights.

H-test

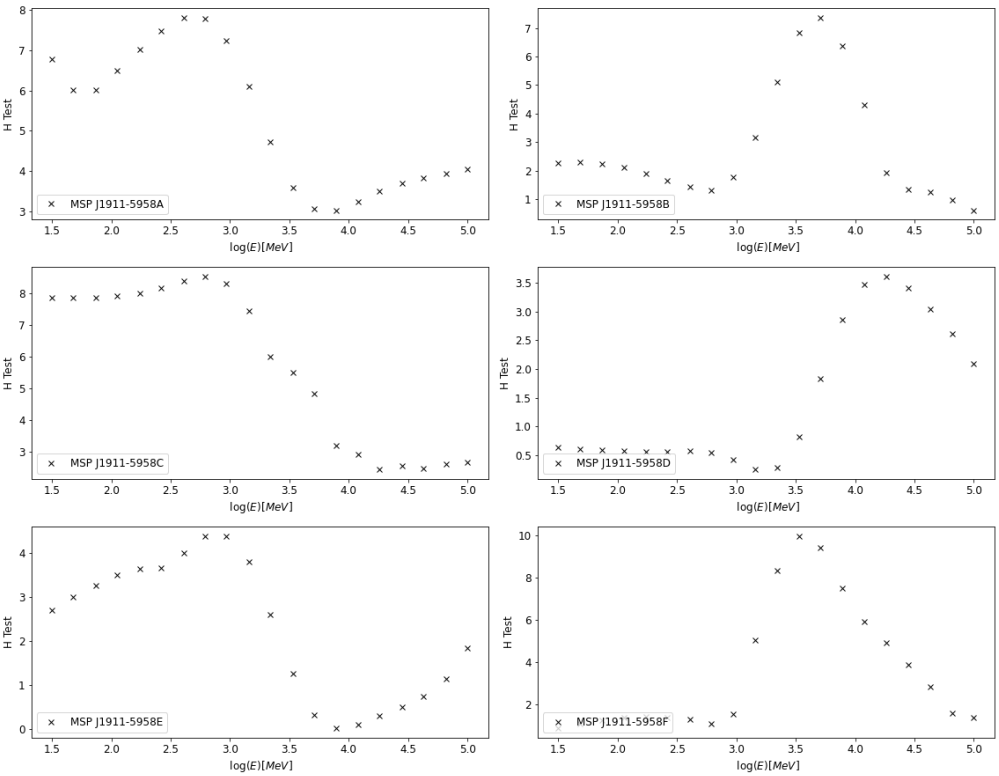

Figure 7.10: The H-test for 20 trial values of $\log(E_{ref})$ for all five detected MSPs in NGC 6752. A bell-shaped curve and an $H > 25$ is expected from a gamma-ray MSP [16].

Figure 7.10 shows no MSP was detected with an HTS > 9, which means there is insufficient evidence to confirm pulsed emission from any of the MSP I have been able to phase-fold in NGC 6752. This suggests that the MSP in this GC are too faint to detect in gamma-rays. Most of the MSPs have the typical 'bell-curve' expected for gamma-ray MSPs [41] which could suggest that these MSPs are more typical to these observed in the Galactic neighbourhood, however there is currently no evidence to suggest that the MSP in GCs are any different to isolated MSPs [88].

7.0.5 NGC 6641

NGC 6641 is closer to the Galactic plane than ω Centauri, 47 Tuc, NGC 7078 and NGC 6752. There is consequently more background gamma-ray emission and for this reason it is not possible to calculate the diffuse response in order to produce weighted light-curves. Instead I have relied on the H-test to test for pulsed emission.

H-test

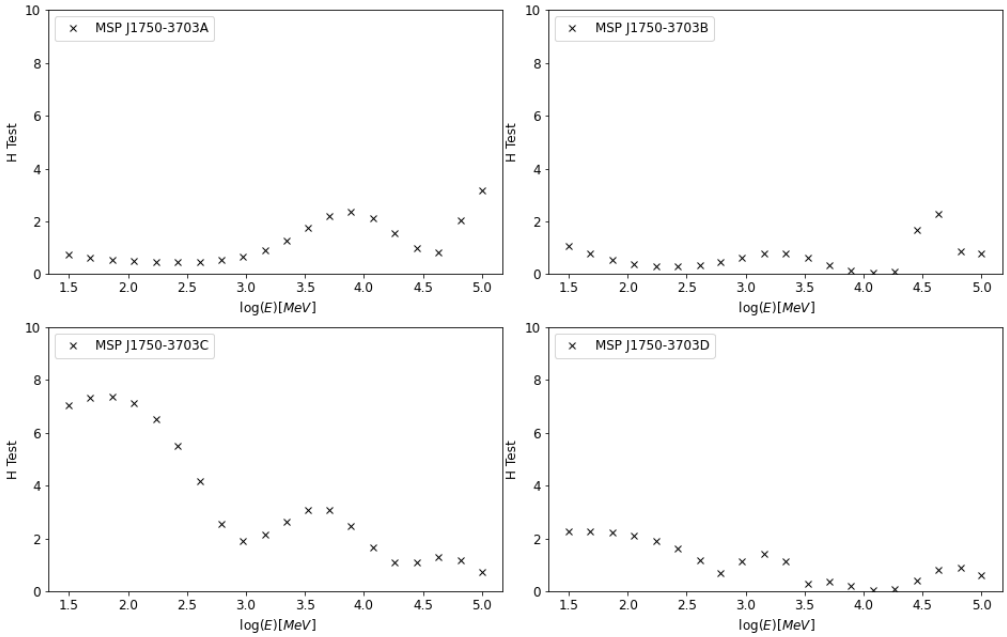

Figure 7.11: H-test statistic for MSPs in NGC 6441. . A bell-shaped curve and an $H > 25$ is expected from a gamma-ray MSP [16].

I conducted the H-test over the full 13 year period, as well as over a smaller time period close to when the MSP were timed and the errors in the ephemerides are less significant. I have found no evidence for pulsation above 3σ from any the MSP I have valid ephemerides for. This would suggest that there is no single, strong MSP in this GC. As NGC 6441 is a bright GC with a high TS this could be evidence that there are other sources of gamma-rays in this GC.

7.0.6 Terzan 5

Like NGC 6441, Terzan 5 is also closer to Galactic plane (meaning there is more background emission) and I am therefore only using the H-test to test for pulsed emission.

H-Test

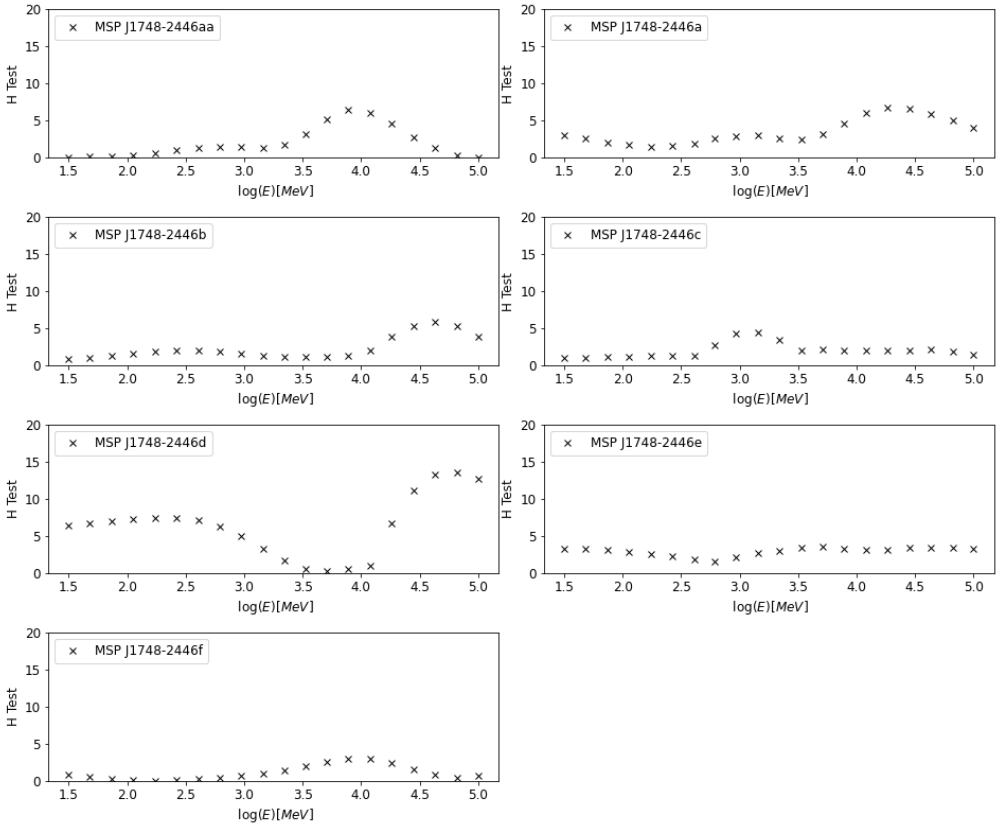

Figure 7.12: H-test statistic shown for a subset of MSP in Terzan 5. A bell-shaped curve and an $H > 25$ is expected from a gamma-ray MSP [16]. No statistically significant pulsed emission has been detected.

I have found no evidence of significant pulsed emission from any MSP I have an ephemerides for in Terzan 5. A previous study of Terzan 5 also applied the H-test and found no evidence above 2.2σ for pulsed emission from any MSP that had been detected in Terzan 5 [99] .

Chapter 8

Evidence for Dark Matter in Globular Clusters

8.1 Introduction

If no pulsed emission from MSP can be detected, it is necessary to consider the other possible origins for the gamma-ray emission. It is important to note that we are placing an upper limit on the contribution of MSP to the overall emission from the GC. In Chapter 9, I will calculate a statistical upper limit on the MSP emission, given that no pulsed emission had been detected (above the 3σ level of significance).

In this chapter, I am going to review the evidence for Dark Matter (DM) in GC and the mechanisms by which DM could contribute to the gamma-ray emission. I am then going to investigate the possibility that the GC emission could be explained by some combination of DM and MSPs. I will do this by comparing the statistical likelihoods of DM only, MSP only, and a combined 'DM+MSP' models. Finally, I will attempt to estimate an upper limit on the MSP emission based on the spectrum of the GC and the combined DM+MSP model.

8.2 Dark Matter

8.2.1 A Brief Introduction to Dark Matter

Dark matter (DM) is a form of matter that astrophysical observations imply constitutes 27% of the universe. DM does not seem to interact with electromagnetic radiation, which makes it difficult to study. Ordinary (baryonic) matter (which makes up the observable universe) is thought to be only 5% of the total matter in the universe [105]. Despite its believed abundance, evidence for DM has only been found via its gravitational effects, such as galaxy rotation curves and gravitational lensing (which are only consistent with currently accepted theories of gravity if there is missing, invisible matter). The precise constituents of DM remain unknown, but current observations suggest it must have mass (due to the gravitational effects observed), and be weakly interacting, which is why DM has not been observed interacting with visible matter.

One primary candidate for DM is a Weakly Interacting, Massive Particle (often referred to as a WIMP) that is beyond the current Standard Model of particle physics. DM is

currently being searched for in particle physics collider experiments (notably the Large Hadron Collider at CERN), and by searching for DM interactions with baryonic matter in cryogenic experiments deep underground (to minimise background radiation) these approaches are known as direct detection experiments [115].
DM is also being searched for indirectly. If DM really makes up 27% of the universe, then we would expect to be able to observe it annihilating or decaying in astrophysical observations. Annihilating or decaying DM would likely produce an excess of a Standard Model particle (or antiparticle), it is common to look for an excess of photons (as *Fermi*-LAT does) or neutrinos [85].

8.2.2 Searching for DM - Indirect Detection

How DM Produces a Signal

If DM is indeed composed of WIMPs and have a mass between 1 GeV-1 TeV, then they could self-annihilate (as shown in Figure 8.1) into a particle-antiparticle pair (such as a pair of leptons $\mu^+\mu^-$ or a pair of hadrons such as $b\bar{b}$), these would have short lifetimes and decay into longer lived particles, which could then collide with matter and produce (gamma-ray) photons. Alternatively, DM may decay into baryonic matter (pairs of particles already within the Standard Model) (as shown in Figure 8.2) which would then annihilate to produce gamma-rays [33] that instruments like Fermi-LAT would be sensitive to.

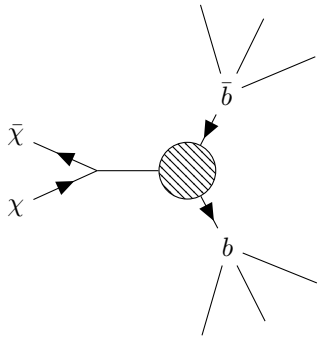

Figure 8.1: Feynman Diagram showing how a pair of DM particles ($\chi\bar{\chi}$) could self-annihilate to a pair of $b\bar{b}$ quarks. The circle indicates a process involving some potential new physics that would allow DM to transform into baryonic matter. The b or $\bar{b}$ quarks could then promptly decay, producing hadronic showers and gamma-ray photons.

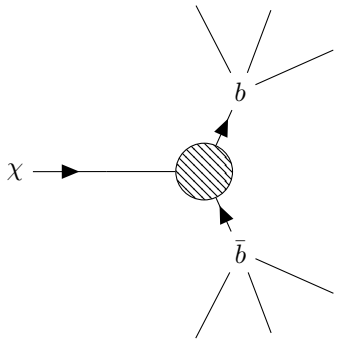

Figure 8.2: Feynman Diagram showing how a DM particle (χ) may decay into a pair of $b\bar{b}$ quarks. The circle indicates a process involving some potential new physics. The b or $\bar{b}$ quarks could then promptly decay, producing hadronic showers and gamma-ray photons.

Expected Features of a DM Signal

In order to search for DM, we need to also understand the expected features of a photon (or neutrino) flux (Φ) that DM would produce. For a DM particle χ of mass m_χ moving at a relative velocity v, this can be described using:

$$\Phi(E,\phi) = \frac{<\sigma v>}{8\pi {m_\chi}^{(2)}} \frac{dN}{dE} \int [\rho(r)]^{(2)} dl \tag{8.1}$$

[85] where σ is the annihilation cross section for the DM particle. For decaying DM σ is inversely proportional to the lifetime. For annihilating DM, the quantity $\frac{<\sigma v>}{2}$ is the expected interaction rate for DM particles. It is thought that the interaction rate is determined by the relic (remaining) density of DM particles following thermal freeze-out in the early universe [63]. Cosmological observations and measurements have placed tight constraints on the possible masses and interaction rates of DM particles.

The functional form of $\frac{dN}{dE}$, depends on the particles produced following annihilation, as well as the branching ratio in a given channel. Figure 8.3 shows how the energy spectrum shape varies for different decay products.

The integral arises from the astrophysical environment the DM is in, it is an integral of the DM density ($\rho(r)$) over the line of sight l. Note that this is the density in a spherically symmetric object. This integral is known as the J-factor for self-annihilation (see Figure 8.1) and the D-factor for decay (see Figure 8.2). The factor of 2 on the mass term (m_χ) and in the integral ($\rho(r)^2$) apply in the self-annihilation regime.

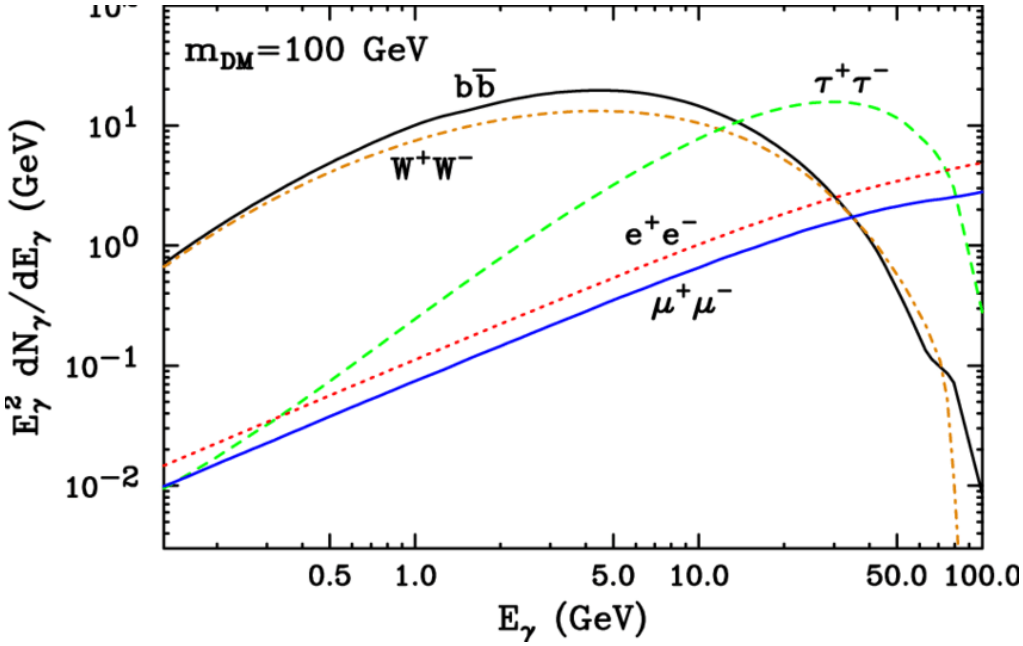

Figure 8.3: Taken from [42]. Shows the expected gamma-ray energy spectrum for different annihilation channels for a DM particle of mass $m_\chi = 100\,\text{GeV}$. Note how the spectral shape changes depending on the particles produced when the DM decays.

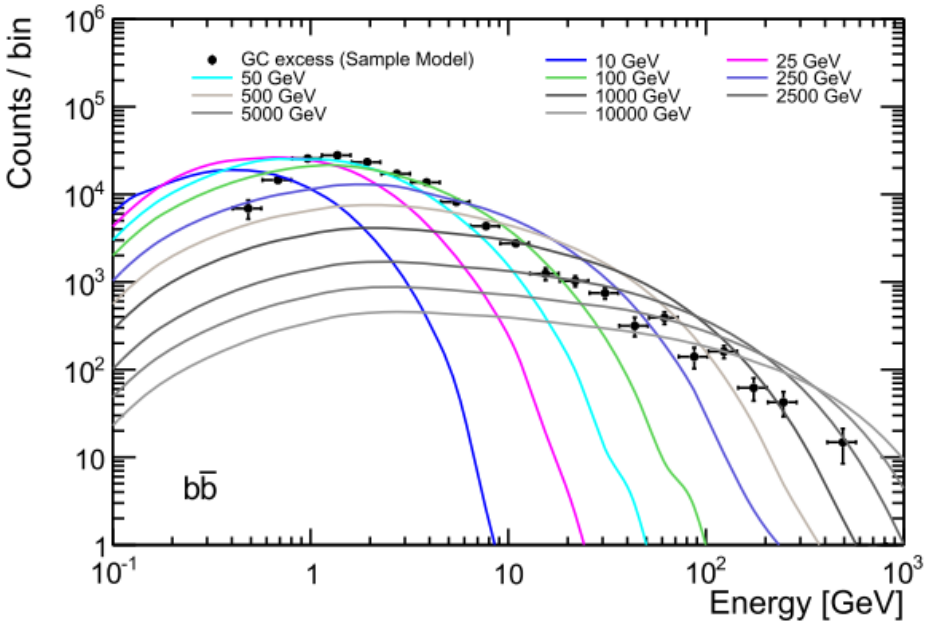

Figure 8.4: Plot taken from [15] which demonstrates how the DM particle mass determines the energy of peak emission. This is shown here for DM annihilation into $b\bar{b}$ pairs. A lower mass DM particle leads to a more peaked energy spectrum.

8.2.3 Recent Searches for DM via Indirect Detection

Indirect DM searches can be difficult because there are many systematic uncertainties that occur when predicting density distribution of DM in a given object. Additionally large backgrounds (such as the isotropic diffuse emission) could make distinguishing a DM signal difficult.

In order to study DM indirectly it is advantageous to study objects that have (at least) one of the following:

1. A larger annihilation or decay rate
2. A distinct spectral shape, that is well understood
3. Regions that are likely to have a larger than average DM density i.e the centre of a galaxy, or within galaxy clusters - this is due to the strong gravity in this region

There are several objects and regions of space that satisfy the above criteria, and have been studied. In the next few sections I am going to discuss them.

The Galactic Centre

The Galactic Centre is, in theory, a good place to search for a DM signal because of the very large observed gamma-ray excess flux, which has an angular distribution and energy spectrum consistent with DM particles of mass $25 - 30$ MeV and annihilation cross -section $\sigma = 9 \times 10^{-26}$ cm^{3}s^{-1} [64].

However, the emission from the Galactic Centre is complex : the are many known astrophysical sources contributing to the observed emission (such as some observed MSPs, supernovae remnants and notably the supermassive black hole right at the centre) which create a significant challenge when trying to separate a potential DM signal. Furthermore, *Fermi*-LAT (and other gamma-ray telescopes such as HESS) does not have sufficient angular resolution to resolve these point sources in the Galactic Centre. It is therefore, for example, difficult to distinguish between an ensemble of MSPs or a smooth, peaked spectrum expected from DM annihilation.

Dwarf Spheroidal Galaxies

Dwarf spheroidal galaxies (dSpyhs) are small, low-luminosity galaxies. They are similar to GCs in that they tend to house an old stellar population, but are usually much larger, fainter and are often more elliptical in shape [127]. Owing to their age, dSphys tend to have very little dust or gas and it would therefore be easier to distinguish a DM signature from astrophysical sources. There is also some evidence to suggest that the mass required to explain the stellar encounter rates is much larger than the mass inferred from the mass-to-light ratio at optical wavelengths. This could imply that dSphys contain a larger than average DM fraction as well as having a clean background to place more stringent bounds on the DM annihilation cross-section (σ) [20].

Globular Clusters

The advantages for searching for evidence of DM in GCs over dSphys is that they are brighter in gamma-rays: there are 39 GCs that have associated gamma-ray emission in the most recent *Fermi*-LAT source catalogue, and no dSphys (they are only associated sources, meaning there is no evidence above 5σ significance that there is any emission from the galaxy itself)[84]. The reason for this is that dSphys tend to be satellites to the Milky Way and are therefore too far away to have observable gamma-ray emission.

Previous studies of GC 47 Tuc [40] and Omega Centauri [39] have found evidence to suggest that DM annihilation may be responsible for some of the gamma-ray emission based on the spectral shape of the GC. At this time of study in [39], no MSPs had been detected in Omega Centauri, so it was not possible to place limits on possible MSP

emission using timing information from the MSPs. Additionally, no individual MSP had been detected in 47 Tuc in gamma-rays. It is thought that GCs are likely to have evolved in DM halos [1] [58], but no observational evidence has so far been found to support this hypothesis. One theory is that a DM halo could have been destroyed by tidal disruption (caused by the supermassive black hole at the centre of the Milky Way) [40].

8.3 Analysis - Looking for Evidence of DM in selected GCs

8.3.1 DM Model Selection

The DM-induced flux is given in equation 8.1, and the spectral shape of different annihilation channels is shown in Figure 8.3. In this study I am going to assume that the DM contribution to the gamma-ray spectrum is from prompt emission from DM particles of mass $m_\chi = 31 \pm 4$ GeV (a 2σ uncertainty) annihilating into $b\bar{b}$ quark pairs. This spectrum was derived as the best fit DM spectrum in previous analyses of 47 Tuc [40] and ω Centauri [39].) This DM model was derived by assuming that an IMBH in the centre of the GC would lead to an enhanced DM density around the IMBH, and would result in a 'spiky' DM spectrum. In this study, the best fit model was determined by leaving m_χ (which sets the energy of peak emission as shown in Figure 8.4) and the annihilation cross section $< \sigma v >$ (which sets the shape and total flux as shown in Figure 8.3) as free parameters. The results of this study produce consistent results with the best-fit DM explanation for the Galactic Centre gamma-ray excess observed [74, 65].

8.3.2 Scenarios of Emission

I am going to look for evidence of DM in each GC by looking at three different scenarios for emission:

1. Emission only from an ensemble of MSPs (described using Xing+Wang spectral model [134]):

$$\phi_{\mathrm{MSP}} = N_0 \left(\frac{E}{E_0}\right)^{\gamma_1} \exp\left(-\frac{E}{E_c}\right) \tag{8.2}$$

   In my analysis, the normalisation, N_0 is left free to vary.

2. Emission only from DM annihilation using the model described in Section 8.3.1:

$$\phi_{\mathrm{DM}} = N_1 \left.\frac{dN}{dE}\right|_{\mathrm{DM}} \tag{8.3}$$

   In my analysis, the normalisation, N_1 is left free to vary.

3. Emission from a combination of MSPs + DM:

$$\phi_{\mathrm{DM+\ MSP}} = C_1 \left.\frac{dN}{dE}\right|_{\mathrm{DM}} + C_2 \left(\frac{E}{E_0}\right)^{\gamma_1} \exp\left(-\frac{E}{E_c}\right) \tag{8.4}$$

[1] If DM is 'cold', meaning it moves slowly ($v << c$)it would allow large scale structures to form, in agreement with cosmological observations.

where C_1 and C_2 are coefficients that can vary depending on the proportion of DM and MSP emission respectively. The parameters E_0, γ_1 and E_c are defined in the Xing+Wang spectral model in [134].

8.3.3 Determining Which Model is Preferred

In order to statistically compare the different scenarios of emission I have just described I will use the following methods:

1. **TS:** I will use the loglikelihood values for calculated when each model is fitted to the GC spectrum. The relative statistical fit of each model can then be compared by calculating the TS as I did in Chapter 6.

2. **Akaike Information Criterion (AIC):** I discussed the significance of the AIC in Section 5.4.1 and the AIC criterion is defined in (5.8). The number of degrees of freedom, k, for the models I am comparing are as follows:
   The normalisation of the DM model is its only free parameter so $k = 1$. I have called this the 'DM only' model.
   The Xing+Wang model is fitted with only the normalisation free to vary so $k = 1$.
   In the combined fit 'DM+MSP', the normalisation of the MSP and DM contributions has been left free to vary, so $k = 2$.

8.3.4 Calculating the Combined DM+MSP Model

I used the *curve_fit()* method in the `SCIPY` Python package to calculate a non-linear, least squares fit to the spectrum of the GC [130]. This method will calculate C_1 and C_2 in equation 8.4, which are then used to calculate the differential energy flux over the energy range of the analysis. This model is then used as the spectral shape to compute the log likelihood of the model as described in Section 8.3.5.

8.3.5 Calculating the Likelihood of Each Model

I use the *fit()* command in the `GTAnalysis` method in the `FERMIPY` Python package to calculate the log likelihood for each of the models described in Section 8.3.2.

To do this, I used the *create()* command to reload the analysis instance after my full, complete analysis of each of the GC. I then used *free_sources()* to fix all objects in the ROI to their best fit values that had already been determined. I then removed the GC (using *delete_source()*) and re-added it as a new source, at the same Galactic latitude and longitude (as the GC), but this time the spectral shape is defined as a **FileFunction**, which is a text file containing the energy and corresponding differential energy flux $\frac{dN}{dE}$ of the combined model. I then freed the normalisation of the GC and then calculated the log likelihood of the new model using the *fit()* method.

8.4 Results

8.4.1 ω Centauri

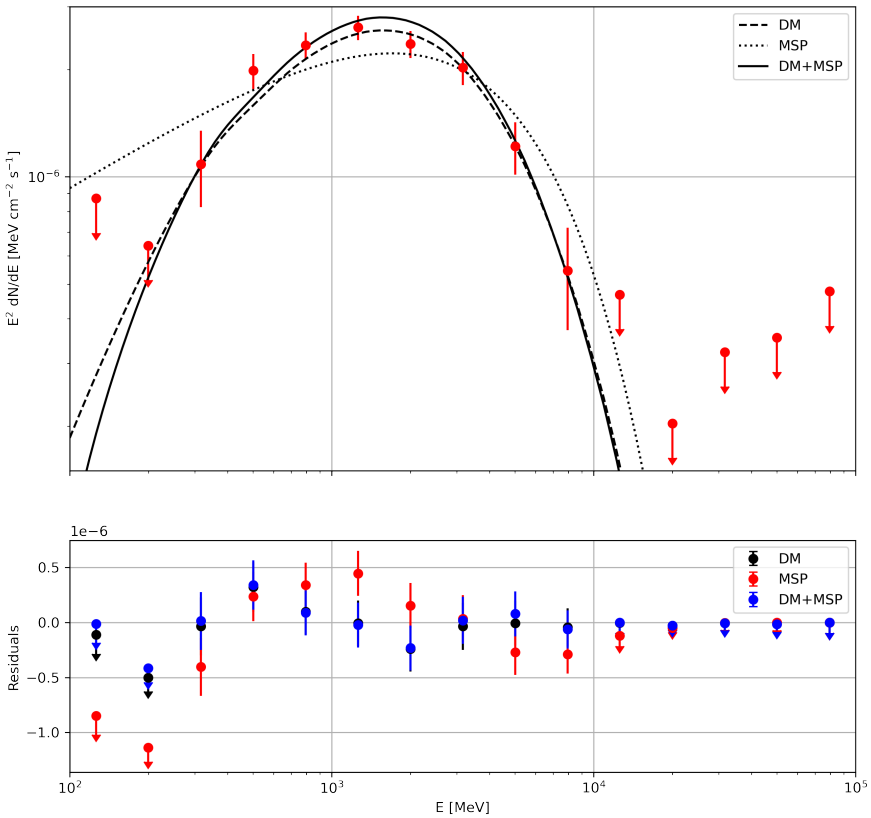

Figure 8.5: Best 'DM+MSP' , 'MSP', 'DM' fits to ω Centauri's spectrum (shown in red). The residual plot shows the difference between the spectrum of ω Centauri and each model.The error bars show 1σ uncertainty on $E^2 \frac{dN}{dE}$ and are evaluated from the likelihood curvature. Spectral bins with a $TS < 16$ are marked as 95% confidence level upper limits which are evaluated from the profile likelihood.

Statistical Comparison of Models

Model	Log likelihood	AIC	Δ AIC
'DM+ MSP'	1598141.411	-1598137.411	1.65
'DM'	1598141.058	-1598139.058	0.00
'MSP'	1598127.746	-1598125.746	11.70

Table 8.1: Table of the log likelihood and AIC statistic for the fit of each model to ω Centauri's spectrum. The column labelled Δ AIC is the difference in AIC between a model and the model with the lowest AIC. The AIC implies that the 'DM' and 'DM+MSP' models cannot be distinguished but the 'MSP' model is a significantly worse fit .

Models being compared	TS
'DM' vs. 'MSP'	27
'DM' vs. 'DM+MSP'	0.71
'DM+MSP' vs. 'MSP'	27

Table 8.2: A comparison of the fit of the models to ω Centauri's spectrum. The TS is the statistical significance that a model is preferred over the other (as defined in equation 5.6). The TS values imply that the 'DM' and 'DM+MSP' models are both preferred over the 'MSP' model and that there is no statistically significant difference between the 'DM' and 'DM+MSP' models.

Discussion

The small scale residuals in Figure 8.5 suggest that all three models are a good fit to the spectrum of ω Centauri. Comparing the TS values in Table 8.2, suggests that the 'DM+MSP' and 'DM' models are much better fits over a 'MSP' only model. Additionally the 'MSP' only model appears to match the spectrum particularly poorly below 500 MeV. The AIC statistic suggests no statistically significant preference between 'DM+MSP' and 'DM' (a probability of 0.02 of 'DM+MSP' being preferred over and 'DM' only). Given that the maximum likelihood analysis has demonstrates that models with a DM component are significantly preferred over a MSP only model this could be interpreted of the presence of DM in ω-Centauri.

8.4.2 47 Tuc

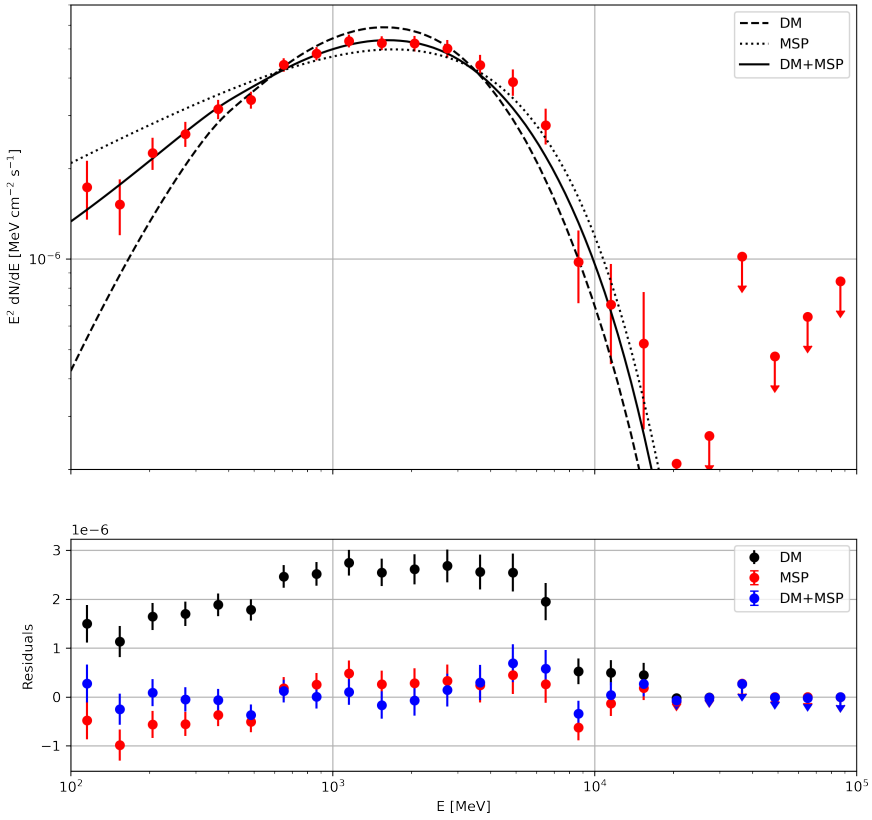

Figure 8.6: Best 'DM+MSP' , 'MSP', 'DM' fits to 47 Tuc's spectrum (shown in red). Residual plot showing the difference between the spectrum of 47 Tuc and each model. The error bars show 1σ uncertainty on $E^2 \frac{dN}{dE}$ and are evaluated from the likelihood curvature. Spectral bins with a $TS < 16$ are marked as 95% confidence level upper limits which are evaluated from the profile likelihood.

Statistical Comparison of Models

Model	Log likelihood	AIC	Δ AIC
'DM + MSP'	-116787.735	116791.735	0
'DM'	-116807.739	116809.739	18.0
'MSP'	-116803.625	116805.625	13.9

Table 8.3: Table of the log likelihood and AIC statistic for the fit of each model to 47 Tuc's spectrum. The column labelled Δ AIC is the difference in AIC between a model and the model with the lowest AIC score. The AIC implies that the best model is 'DM+MSP' followed by 'MSP' and then 'DM'. The Δ AIC also shows that the 'DM+MSP' is also a statistically better model than the 'MSP' or 'DM' models.

Models being compared	TS
'MSP' vs. 'DM'	8.2
'DM+MSP' vs. 'DM'	40.0
'DM+MSP' vs. 'MSP'	31.8

Table 8.4: A comparison of the fit of the models to 47 Tuc's spectrum. The TS is the statistical significance that a model is preferred over the other (as defined in 5.6). The TS values imply that the 'DM+MSP' model is significantly preferred over the 'DM' and 'MSP' models. The 'MSP' model is slightly preferred over the 'DM' model.

Discussion

The TS values demonstrate 'DM+MSP' model is preferred significantly over both the 'DM' (with a TS = 40) and 'MSP' (with a TS = 32) models. Additionally the AIC values shown in Table 8.3 ranks the models from best to worst as 'DM+MSP', 'MSP', 'DM', and the difference in AIC values (Δ AIC) also indicates that 'DM+MSP' is a superior model to 47 Tuc's spectrum compared to the 'DM' and 'MSP' models. These findings would suggest that both DM and MSP contribute significantly to 47 Tuc's spectrum. Additionally the 'MSP' only model is preferred over 'DM' only model by a TS = 8 and a ΔAIC = 4, this suggests that the 'MSP' model is a slightly better fit than the 'DM' only, and this is clear in Figure 8.6, the 'DM' model does not account for the observed energy flux below 1000 MeV, but the 'MSP' model slightly over predicts the GC energy flux below 1000 MeV.

The residuals shown in Figure 8.6 also show that the 'DM' only model under estimates the energy flux and that the 'DM+MSP' and 'MSP' model model the energy flux more closely. This may indicate that the MSP do make a significant contribution to the GC flux, even if we are not able to detect any pulsed emission from individual MSPs.

8.4.3 NGC 7078

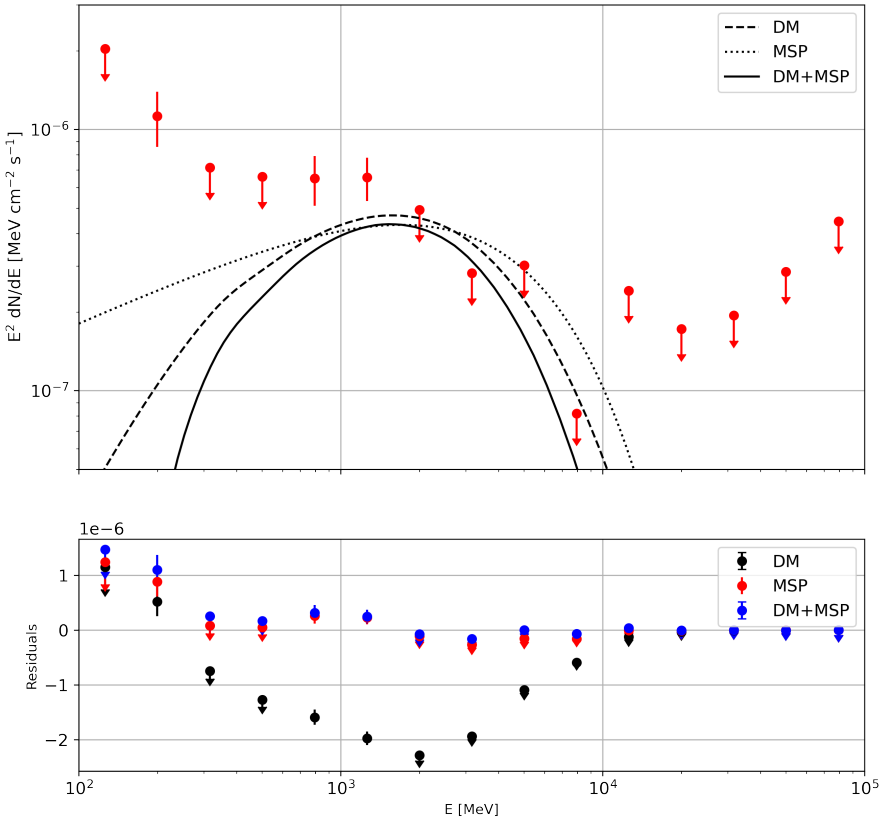

Figure 8.7: Best 'DM+MSP' , 'MSP', 'DM' fits to NGC 7078's spectrum (shown in red). Residual plot showing the difference between the spectrum of NGC 7078 and each model.The error bars show 1σ uncertainty on $E^2 \frac{dN}{dE}$ and are evaluated from the likelihood curvature. Spectral bins with a $TS < 16$ are marked as 95% confidence level upper limits which are evaluated from the profile likelihood.

Statistical Comparison of Models

Model	Log likelihood	AIC	Δ AIC
'DM+ MSP'	287865.386	-287861.386	3.88
'DM'	287866.014	-287864.014	1.26
'MSP'	287867.270	-287865.270	0

Table 8.5: Table of the log likelihood and AIC statistic for the fit of each model to NGC 7078's spectrum. The column labelled Δ AIC is the difference in AIC between a model and the model with the lowest AIC. The AIC ranks the models (from best to worsts) as 'DM+ MSP', 'DM' , 'MSP' . However the difference in AIC values implies that the 'DM' and 'MSP' models cannot be distinguished.

Models being compared	TS
'MSP' vs. 'DM'	2.51
'DM' vs. 'DM+MSP'	1.26
'MSP' vs. 'DM+MSP'	3.77

Table 8.6: A comparison of the fit of the models to NGC 7078's spectrum. The TS is the statistical significance that a model is preferred over the other (as defined in 5.6). The TS values suggest that none of the models can be distinguished statistically.

Discussion

None of the models considered are consistent with the NGC 7078's spectrum below 1000 MeV. The TS values in Table 8.6 imply that it is not possible to distinguish statistically between any of the models. The AIC values in Table 8.5 suggest that the 'MSP' and 'DM' models are better models than the 'DM+MSP' (ΔAIC > 2 between the 'DM+MSP' and 'MSP' or 'DM' models) which has more degrees of freedom. It is also clear from Figure 8.7 that the spectrum is not consistent with a MSP only, DM only or only a combination of just DM+MSP. These findings do not provide any compelling evidence for DM or MSP emission from NGC 7078. Nevertheless, this finding does not rule out the presence of DM in NGC 7078: I have only considered one annihilation channel in this study, and it is entirely possible that the there are other sources of gamma-ray emission in NGC 7078 apart from the two possibilities of DM and MSP considered here.

8.4.4 NGC 6752

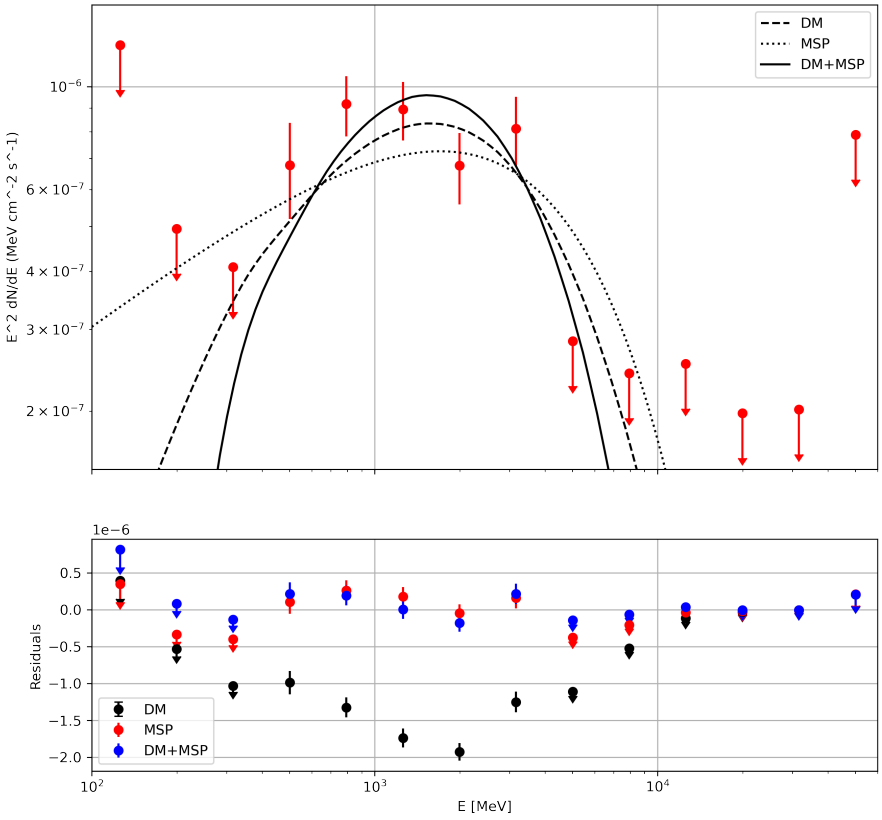

Figure 8.8: Best 'DM+MSP', 'MSP', 'DM' fits to NGC 6752's spectrum (shown in red). Residual plot showing the difference between the spectrum of NGC 6752 and each model. The error bars show 1σ uncertainty on $E^2 \frac{dN}{dE}$ and are evaluated from the likelihood curvature. Spectral bins with a $TS < 16$ are marked as 95% confidence level upper limits which are evaluated from the profile likelihood.

Statistical Comparison of Models

Model	Log likelihood	AIC	Δ AIC
'DM+ MSP'	201763.718	-201759.718	0
'DM'	201761.439	-201759.439	0.28
'MSP'	201756.763	-201754.763	4.95

Table 8.7: Table of the log likelihood and AIC statistic for the fit of each model to NGC 6752's spectrum. The column labelled Δ AIC is the difference in AIC between a model and the model with the lowest AIC. The AIC implies that the 'DM+MSP' and 'DM' are equal models to NGC 6752's spectrum, and the 'MSP' is a comparatively worse model.

Models being compared	TS
'DM' vs. 'MSP'	21.4
'DM+MSP' vs. 'DM'	4.60
'DM+MSP' vs. 'MSP'	13.9

Table 8.8: A comparison of the fit of the models to NGC 6752's spectrum. The TS is the statistical significance that a model is preferred over the other (as defined in 5.6). The TS values indicate that the models containing a DM component are significantly preferred over a MSP only model.

Discussion

The AIC values shown in Table 8.7 suggest that the 'DM' and 'DM+MSP' are equally good models to NGC 6752's spectrum, and Table 8.8 shows that the 'DM+MSP' model is only preferred over the 'DM' only model with a $TS = 4.6$. These findings show that the models with a DM component cannot be distinguished statistically. Both the 'DM+MSP' and 'DM' are considered better models to the spectrum than the 'MSP' only model (with an $\Delta\text{AIC} > 4$). The TS values also show that the 'DM' model is statistically preferred over the 'MSP' only model (with a TS = 21.4) These findings mean that there is some evidence to suggest a DM component resides in this GC. However it is important to remember that there are only four significant spectral points, and the differences between models are most significant at higher/lower energies where we have less significant emission. I also note from that none of the spectral models considered are consistent with all of the spectral bins shown in Figure 8.8, which could suggest that either there are other sources of gamma-ray emission in this GC, and also that the DM or MSP models I am using are not quite accurate for this GC.

8.4.5 NGC 6641

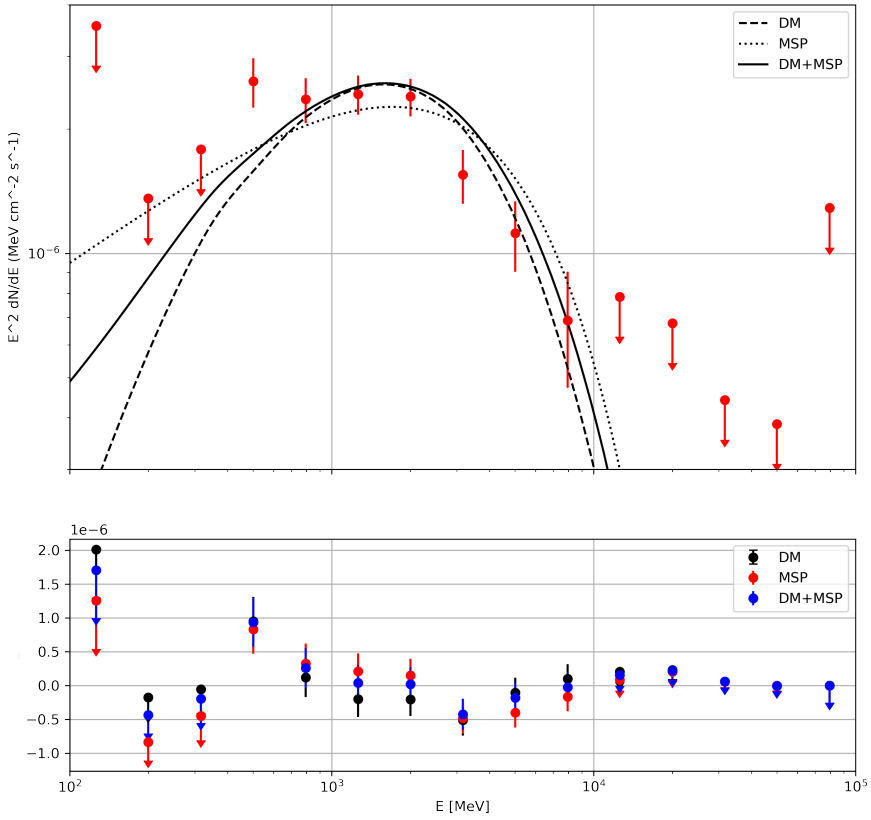

Figure 8.9: Best 'DM+MSP' , 'MSP', 'DM' fits to NGC 6441's spectrum (shown in red). Residual plot showing the difference between the spectrum of NGC 6441 and each model. The error bars show 1σ uncertainty on $E^2 \frac{dN}{dE}$ and are evaluated from the likelihood curvature. Spectral bins with a $TS < 16$ are marked as 95% confidence level upper limits which are evaluated from the profile likelihood.

Statistical Comparison of Models

Model	Log likelihood	AIC	Δ AIC
'DM+ MSP'	7224550.708	-7224546.708	1.00
'DM'	7224549.540	-7224547.540	0.17
'MSP'	7224549.705	-7224547.705	0

Table 8.9: Table of the log likelihood and AIC statistic for the fit of each model to NGC 6441's spectrum. The column labelled Δ AIC is the difference in AIC between a model and the model with the lowest AIC. The similar AIC values imply that all three models are comparable fits to the spectrum.

Models being compared	TS
'MSP' vs. 'DM'	0.33
'DM+MSP' vs. 'DM'	2.34
'DM+MSP' vs. 'MSP'	2.01

Table 8.10: A comparison of the fit of the models to NGC 6441's spectrum. The TS is the statistical significance that one model is preferred over another (as defined in 5.6). The TS values suggest that none of the models can be distinguished statistically.

Discussion

The AIC values shown in Table 8.9 and the TS values in 8.10 indicate that there is no statistically significant difference between any of the models. The reason for this is partly because of the spectral shape of NGC 6441, and that there is no significant emission below 500 MeV and the upper limits are consistent with all the models. This means there is insufficient evidence to rule out DM contribution to the emission, but NGC 6441's spectrum could also be explained without a DM contribution.

There is most discrepancy between the three models at energies below 1000 MeV, which is interesting because NGC 6441 is close to the Galactic plane and it has been observed that GC close to the Galactic plane have more low energy emission compared to GC with high latitude/longitudes.

8.4.6 Terzan 5

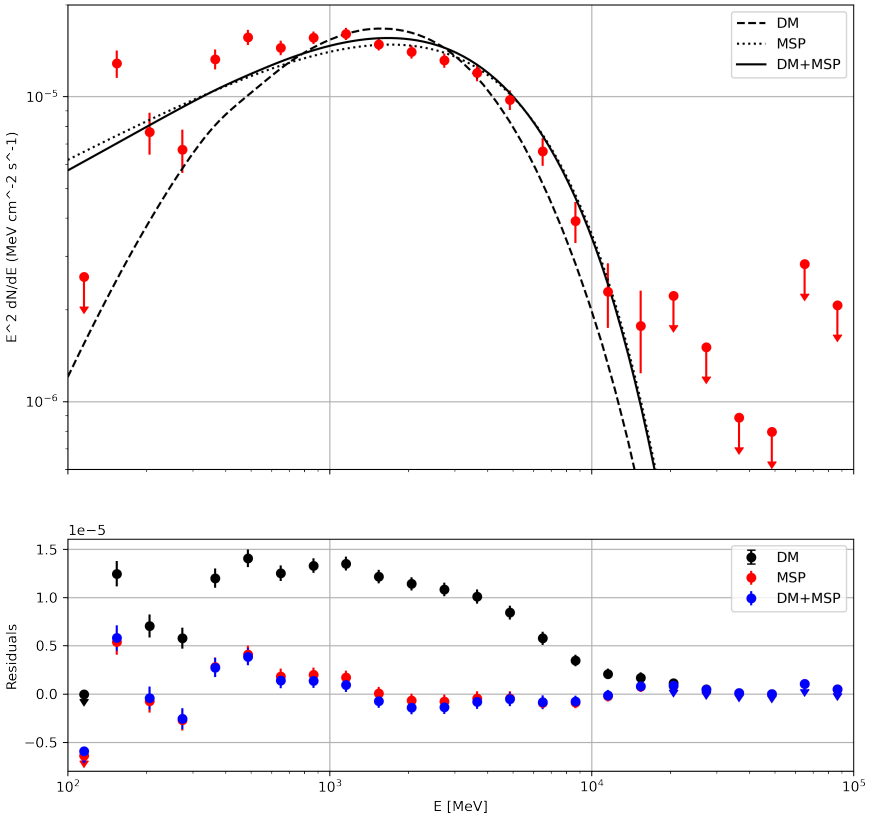

Figure 8.10: Best 'DM+MSP' , 'MSP', 'DM' fits to Terzan 5's spectrum (shown in red). Residual plot showing the difference between the spectrum of Terzan 5 and each model.The error bars show 1σ uncertainty on $E^2 \frac{dN}{dE}$ and are evaluated from the likelihood curvature. Spectral bins with a $TS < 16$ are marked as 95% confidence level upper limits which are evaluated from the profile likelihood.

Statistical Comparison of Models

Model	Log likelihood	AIC	Δ AIC
'DM+ MSP'	24527973.269	-24527969.269	1.86
'DM'	24527924.466	-24527922.466	48.7
'MSP'	24527973.132	-24527971.132	0

Table 8.11: Table of the log likelihood and AIC statistic for the fit of each model to Terzan 5's spectrum. The column labelled Δ AIC is the difference in AIC between a model and the model with the lowest AIC. The AIC values indicate that the 'DM+MSP' and 'MSP' models are a comparable fit to the spectrum, and that the 'DM' model is a significantly worse model.

Models being compared	TS
'MSP' vs. 'DM'	97
'DM+MSP' vs. 'DM'	97
'DM+MSP' vs. 'MSP'	0.27

Table 8.12: A comparison of the fit of the models to Terzan 5's spectrum. The TS is the statistical significance that a model is preferred over the other (as defined in 5.6). The TS values indicate that the 'DM+MSP' and 'MSP' models are significantly preferred over the 'DM' model. The TS values also indicate that it is not possible to distinguish statistically between the 'DM+MSP' and 'MSP' models.

Discussion

The TS values in Table 8.12 suggest that the 'MSP' and 'DM+MSP' are significantly preferred over a 'DM' model. This is consistent with the AIC values given in Table 8.11: where the models are ranked 'MSP', 'DM+MSP', 'DM' with no statistical preference between the 'MSP' and 'DM+MSP' models. These findings imply that there is a substantial MSP contribution to Terzan 5's emission, and also suggest that we cannot rule out DM annihilation as a component of the emission. I note that the DM model fits particularly poorly at the lower energies, below 500 MeV. This could be explained by Terzan 5 being close to the Galactic plane where there is more background emission.

8.5 Discussion

8.5.1 Evidence for DM in GC?

Based on a maximum likelihood analysis when fitting the different emission models described in Section 8.3.2, a DM component cannot be ruled out for any of the GCs I have studied. A DM component seems most likely in ω Centauri, 47 Tuc, and NGC 6752. This is strengthened by the fact that I have been unable to detect any significant emission from any MSP. NGC 7078's spectrum does not seem to be consistent with any combination of MSP and DM emission, based on the models I have used. A DM component cannot be ruled out for NGC 6441 because it is not possible to determine statistically which model is preferred. A DM component can also not be ruled out in Terzan 5, however the results of my analysis suggest that the spectrum could be equally modelled using only MSP.

8.5.2 How much of the GC Emission could be Accounted for by MSPs?

If the gamma-ray emission from each GC originates entirely from DM and MSP contributions then I can estimate the total energy flux from the MSP using the following calculation. It is possible to calculate the energy flux using the integral [35]:

$$\text{Energy Flux} = \int E \frac{dN}{dE} dE \tag{8.5}$$

Where $\frac{dN}{dE}$, the differential energy flux, is the MSP term in equation 8.4. To calculate the energy flux from MSP I use the integral:

$$\text{Energy Flux from MSP} = N \int_{100\,\text{MeV}}^{100\,\text{GeV}} E \left(\frac{E}{E_0}\right)^{\gamma_1} \exp\left(-\frac{E}{E_c}\right) dE \tag{8.6}$$

where the total energy flux will have units $\text{MeVcm}^{-2}\text{s}^{-1}$. I am integrating over the energy range of my analysis (between 100 MeV-100 GeV).
The normalisation, N, is given as:

$$N = C_2 \times N_0 \tag{8.7}$$

where the coefficient C_2 is from the 'DM+MSP' fit in 8.4 which was calculated using the method described in Section 8.3.4. N_0 is the normalisation of the best fit 'MSP' only model, described in equation 8.2 (i.e the Xing + Wang model fitted to the GC spectrum with just the normalisation free to vary).

Table 8.13 shows the normalisation, N, for the energy flux of each GC, the measured energy flux (from the analysis in Chapter 6), the energy flux from the predicted MSP contribution (calculated using equation 8.6 as described). Using the energy fluxes, I have also calculated the percentage of the GC emission that could be explained by MSP:

$$\%\ \text{MSP} = \frac{\text{Integrated MSP Energy Flux}}{\text{Measured GC Energy Flux}} \tag{8.8}$$

GC	Normalisation ($\times 10^{-14}$) $\mathrm{MeV}^{-1}\mathrm{cm}^{-2}\mathrm{s}^{-1}$	GC Energy flux ($\times 10^{-6}$) $\mathrm{MeVcm}^{-2}\mathrm{s}^{-1}$	MSP Energy flux ($\times 10^{-6}$) $\mathrm{MeVcm}^{-2}\mathrm{s}^{-1}$	% MSP
ω Centauri	1.13 ± 0.04	6.77 ± 0.33	1.08 ± 0.24	16 ± 24
47 Tuc	9.76 ± 0.18	17.04 ± 0.44	9.37 ± 0.04	55 ± 5
NGC 7078	0.81 ± 0.10	2.62 ± 0.30	0.78 ± 0.30	30 ± 30
NGC 6752	2.39 ± 0.19	2.06 ± 0.20	2.29 ± 0.43	110 ± 43
NGC 6441	3.13 ± 0.17	7.92 ± 0.65	3.00 ± 0.51	38 ± 51
Terzan 5	47.51 ± 0.80	52.51 ± 1.45	45.61 ± 0.08	87 ± 8

Table 8.13: Table with the estimated energy flux of the MSP contribution using the 'DM+MSP' model. The normalisation is calculated using equation 8.7, the GC energy flux is from the analysis in Chapter 6 and the MSP energy flux is calculated using equation 8.6. The final column (% MSP) gives the percentage of the GC energy flux that can be accounted for by MSP (from equation 8.8).

The results in Table 8.13 show that there is (with the exception of 47 Tuc) a large uncertainty in the % contribution of MSP to the GC emission. Despite the large uncertainty, these results indicate that ω Centauri's emission can be, at most 40% from MSP. Whilst 47 Tuc and NGC 7078 can be at most 60%. This shows that these three GC could have a significant MSP contribution, but also that their gamma-ray emission cannot be explained entirely by MSP and there is some evidence to suggest there is a DM component. This is important, because it is contrary to the findings in [10]. Table 8.13 also shows that it would be possible to explain the majority of the GC emission with MSP, but it is also entirely possible not to. For example NGC 6441, could be 90% MSP, or 0%! Whilst these findings provide motivation for a more intense search for DM in GCs, it also really throws doubt on the theory that GC emission can be entirely explained by MSP.

8.5.3 Do any of the Models Account for the Observed Energy Flux?

The measured energy flux (discussed in Chapter 6 and shown in Table 6.25) can be compared to integrated total energy flux when the MSP only, DM only, and DM+MSP models are fitted to each GC spectrum, which can be calculated using the *fit()* method in *GTAnalysis*. The energy fluxes calculated for each model and the measured energy flux are compared in Table 8.14.

GC	Energy Flux ($\times 10^{-6}$ $\mathrm{MeVcm}^{-2}\mathrm{s}^{-1}$)			
	Measured	MSP	DM	DM+MSP
ω Centauri	6.77 ± 0.33	7.62 ± 0.30	6.74 ± 0.27	6.60 ± 0.26
47 Tuc	17.04 ± 0.44	17.11 ± 0.03	15.41 ± 0.29	16.44 ± 0.30
NGC 6752	2.06 ± 0.20	2.49 ± 0.19	2.18 ± 0.17	2.00 ± 0.15
NGC 7078	2.61 ± 0.27	1.5 ± 0.19	1.23 ± 0.16	1.11 ± 0.15
NGC 6441	7.91 ± 0.65	7.77 ± 0.41	6.72 ± 0.35	7.13 ± 0.38
Terzan 5	52.50 ± 1.45	50.80 ± 0.86	43.71 ± 0.75	50.01 ± 0.84

Table 8.14: A table comparing the measured energy flux (from my 13 year analysis discussed in Chapter 6 and shown in Table 6.25) and the integrated energy flux for each of the three physical models I am considering.

Table 8.14 demonstrates that the 'DM+MSP' and 'DM' only models are consistent

with the measured energy flux for ω Centauri. However the 'MSP' only model is not consistent and predicts a larger energy flux than is measured. This implies that if all the emission was from MSPs, then the measured energy flux from the GC would be higher : this can be seen from the MSP model in Figure 6.1 where the MSP model significantly over-predicts the energy flux below around 500 MeV.

The 'MSP' only and 'DM+MSP' models have an energy flux consistent with the measured energy flux for 47 Tuc. The 'DM' fitted energy flux is lower than the measured flux and means that 'DM' alone cannot explain the gamma-ray emission from this GC [2]. These findings would suggest that MSP's or a combination of DM and MSPs could provide the energy flux observed. Of course, the observed energy flux does not tell us the relative likelihood of a model describing the observed spectrum: as we saw from Table 8.3, the 'DM+MSP' is statistically preferred over the 'MSP' only model (with a TS = 31.8).

The 'DM' and 'DM+MSP' models have a consistent energy flux with the measured energy flux in NGC 6752. Similarly to ω Centauri, the 'MSP' model gives a higher energy flux than is measured, which is again due to the GC having a low energy flux measured below 500 MeV. These findings would suggest that DM, or a combination of DM and MSPs alone could produce the energy flux observed for NGC 6752, and that no other sources of gamma-ray emission would be needed. This is consistent with the findings in [88], that although there are a number of nearby X-ray sources close to the GC, including several AGN and a number of cataclysmic variables, both of which could both contribute to the gamma-ray emission but this has not been observed (the emission from both AGN and cataclysmic variables would vary in time, however no significant variation in NGC 6752's energy flux has been observed [88]).

The energy flux measured from NGC 7078 is not consistent with any of the models, and would suggest that a combination of DM and MSPs alone cannot explain the observed gamma-ray emission from this GC, which could indicate that there are other sources contributing to the emission.

The 'MSP' and 'DM+MSP' models both produce energy fluxes consistent with the measured energy flux for GC's NGC 6441 and Terzan 5. For both GC, the DM only model cannot account for the measured energy flux.

[2] for the specific DM annihilation channel I have chosen

Chapter 9

Placing Upper Limits on MSP Emission

In Chapter 7 I demonstrated that no significant pulsed emission could be detected from any MSP in the GC I have selected for study. In Chapter 8, I considered whether a combination of DM and MSP emission was consistent with each GC spectrum. I will now place upper limits on the proportion of MSP emission in each GC based on :

1. Comparisons with the GC energy flux and the energy flux that could be accounted for by MSP
2. A statistical upper limit on the MSP contribution given that no individual MSP can be detected

9.1 Upper Limits Based on the Known MSP in each GC

If it is assumed that the MSP account for all of the GC emission, we can compare the observed energy flux from the GC to the expected energy flux based on the number of MSPs and the distance of the GC. The expected energy flux from a MSP (ϵ) is given by:

$$\epsilon = \epsilon_{MSP} \times \text{N.o of MSP} \times \left(\frac{d_{MSP}}{\text{GC distance}}\right)^2 \tag{9.1}$$

Where ϵ_{MSP} is the average energy flux of a MSP, which is the arithmetic mean energy flux of all MSP in the Second *Fermi* Pulsar catalogue [9] (which are the MSP used in the Xing +Wang model [134].

The average energy flux (ϵ_{MSP}) is: $(1.49\pm0.11)\times10^{-5}$ MeVcm^{-2}s^{-1} and the average distance of a MSP (in the Second *Fermi* Pulsar catalog, d_{MSP}) is 1.58 ± 0.30 kpc.

The uncertainty given for the energy flux and distance averages is the average of the uncertainties given on the energy flux and distance measurements for each MSP in the catalogue [9]. This uncertainty is larger than the standard deviation of measurements. The distance uncertainty is particularly large because it is difficult to accurately measure the distance to individual MSP. Most distances are calculated using either the Dispersion Measure which is to do with the electron density of the space surrounding the MSP. The

dispersion is higher closer to the galactic plane and other diffuse sources, which leads to a larger uncertainty on the measurement. It is particularly important to consider the distance uncertainty because the GC I have chosen to study are significantly further away than the MSP in the model [1].

9.1.1 Results of Comparing Energy Flux

GC	Energy Flux Observed ($\times 10^{-6}$) MeVcm^{-2}s^{-1}	Energy Flux Expected ($\times 10^{-6}$) MeVcm^{-2}s^{-1}	Distance kpc
47 Tuc	17.0 ± 0.44	51.5 ± 25	4.45 ± 0.01 [44]
ω Cen	6.77 ± 0.33	20.7 ± 12	4.84 ± 0.34 [129]
Terzan 5	52.5 ± 0.11	30.5 ± 19	5.9 ± 0.5 [83]
NGC 7078	2.61 ± 0.27	2.88 ± 1.4	10.94 ± 0.13 [34]
NGC 6752	2.06 ± 0.2	21.0 ± 12	4.0 ± 0.25 [38]
NGC 6441	7.91 ± 0.26	2.77 ± 1.6	13.1 ± 0.7 [101]

Table 9.1: A comparison between the observed energy flux (from my analysis in Chapter 6) and the expected energy flux based on the number of MSPs in each GC.

- In the case of 47 Tuc, ω Cen, NGC 6752, Table 9.1 shows that the observed energy flux is considerably smaller than the expected energy flux based on the estimated energy flux from the population of MSPs observed in the GC. This would suggest that the MSP in these GC are considerably fainter than those in the Xing + Wang model. Observations at other wavelengths have shown no evidence of any differences between the population of MSPs used in the Xing+Wang model and the MSP residing in GC [59]. However this observed discrepancy in energy flux could suggest that the MSP inside these GC emit less strongly in gamma-rays than the MSP in [9].

- There is a large uncertainty on the expected energy flux, the greatest source of which is the uncertainty on the distance measurements to the MSPs in the Xing+Wang model. Even with this large uncertainty, the observed and expected energy fluxes are not consistent for any of the GC (apart from NGC 7078 which is faint, and therefore may have an unreliable measurement).

- Terzan 5 and NGC 6441 have a larger observed flux than is expected from their MSP population; however interestingly these GC are both closer to the Galactic plane and may well be dominated by lower energy, diffuse emission.

- GC with high latitude/longitude have lower energy fluxes than expected whereas those closer to the Galactic plane have higher fluxes than expected. This is a small sample so it is not possible to draw too many conclusions, but could be to do with the way GC has formed (there is some evidence that some GC are evolved Dwarf Galaxies [27, 127]) or because the Galactic emission is not well modelled.

[1] The nearest GC in my selection is 47 Tuc at a distance of 4.45 kpc [117, 44] which has been measured using parallax. For this reason, it is necessary to account for distance when estimating the possible energy flux from a MSP in the GC.

9.2 Upper Limits based on the Observed GC Energy Flux

The number of MSPs needed to account for the total gamma-ray emission is:

$$\frac{E_{GC}}{\epsilon_{MSP}} \times \left(\frac{d_{GC}}{d_{XW}}\right)^2 \tag{9.2}$$

where E_{GC} is the energy flux observed from the GC and ϵ_{MSP}, d_{MSP} are the average energy flux and distance of a MSP a discussed in equation 9.1.

GC	Energy Flux Observed ($\times 10^{-6}$) MeVcm^{-2}s^{-1}	MSP known	MSP needed to account for observed energy flux
47 Tuc	17.0 ± 0.44	28	9 ± 2
ω Cen	6.77 ± 0.33	15	5 ± 2
Terzan 5	52.5 ± 0.11	39	67 ± 2
NGC 7078	2.61 ± 0.27	9	8 ± 2
NGC 6752	2.06 ± 0.20	10	9 ± 2
NGC 6441	7.91 ± 0.26	9	29 ± 2

Table 9.2: Number of MSP needed to account for the gamma-ray emission in the GC based on the observed GC energy flux and the energy flux of an average MSP in the Xing+Wang model. Calculation used to calculate the number of MSPs is given in 9.2.

- 47 Tuc and ω Centauri have more observed MSPs than are needed to account for the energy flux, which suggests that the MSPs in these GC are fainter than those used in the Xing+Wang model (in [9]). However, as noted above there is no observational evidence that the GC MSP population are different from that in the Galactic plane.
- Terzan 5 and NGC 6441 need more MSP than are currently known to exist in these GC to accounts for the observed gamma-ray emission. Further Radio surveys could be used to determine whether there are more MSPs within these GC that have not yet been detected. Alternatively, it is possible that the MSPs in these GC are actually brighter than expected (from the Xing+Wang model), however if this were the case it is even more surprising that no individual MSP can be resolved.
- In NGC 7078 and NGC 6752 the number of MSPs is consistent with the observed gamma-ray emission.

9.3 Placing Statistical Upper Limits on the MSP Emission

If no pulsed emission is detected from any single MSP then upper limits can be placed on the possible contribution of MSP to the total GC emission. This is a statistical approach which is not unreasonable because the GC I have selected for study are bright and therefore have high photon counts (especially when integrated over a 13 year period).

9.3.1 Method 1 - What could be the Maximum Total % MSP Contribution to the GC?

If we make the assumption that the MSP population in a given GC account for all the emission then we can estimate the minimum number of photons needed from each MSP for this to be the case. We can then calculate a possible upper limit on the contribution from the MSPs observed in the GC. If we suppose that n_{pred} photons have been observed from a GC (integrated over the analysis period), and that there are N MSPs observed in the GC then if each MSP is equal in intensity the maximum number of photons from each MSP would be n_{msp}:

$$n_{msp} = \frac{n_{pred}}{N} \tag{9.3}$$

Assuming that we would need a minimum of 3σ per MSP for detection, then:

$$3\sigma = 3\sqrt{n_{msp}} \tag{9.4}$$

At best, we would have n_{ul} photons

$$n_{ul} = 3\sqrt{n_{msp}} \tag{9.5}$$

So the maximum total emission from all MSPs is N_{UL} where

$$N_{UL} = n_{ul} \times N \tag{9.6}$$

As a percentage P_{msp} of the total GC emission this is

$$P_{msp} = \frac{N_{UL}}{N} \times 100 \tag{9.7}$$

Results

GC	GC photon count	N.o of MSP [46]	UL on MSP emission (%)
47 Tuc	7403	29	19 ± 3
ω Cen	3068	15	21 ± 4
Terzan 5	24,029	39	11 ± 2
NGC 7078	2222	9	19 ± 5
NGC 6752	905	9	30 ± 6
NGC 6441	4081	10	19 ± 5

Table 9.3: Table showing an estimate of the % contribution of MSP to the GC emission, assuming that the MSP are the dominant source of gamma-ray emission. The number of photons from each GC has been calculated in the full 13 year analysis described in Chapter 6.

- One interpretation of the results in Table 9.3 is that it should be possible to detect MSP emission in every GC even if the total MSP contribution is around one quarter of the overall emission from the GC. If this was the case, we really ought to be able to resolve some of the MSPs, even if they did not account for the GC emission.
- Another interpretation is that it is quite likely that the MSP are not the only source of gamma-ray emission in GC, and may not even be the dominant source.

- The UL is based on the total number of MSPs, so each individual MSP would not be a large contributor to the GC emission. This could explain why we cannot resolve individual MSPs but it would also suggest that perhaps the MSP in GCs are much fainter than those in the Galactic neighbourhood (as shown in 9.2) which suggests there is a different population of MSPs in the GC compared to the Galactic neighbourhood.
- Is the assumption really valid that the MSP are all equal gamma-ray emitters? We know in the case of NGC 6624 and NGC 6626 that there is one bright detectable MSP, and in the case of NGC 6624 at least 10 other MSPs that have not been detected and do not appear to be strong gamma-ray emitters (based on the photon count and energy flux observed).

9.3.2 Method 2 - Minimum Number of Photons Needed to Detect MSP in the Main pulse above the GC Emission

It is possible to estimate the minimum energy flux required to detect an MSP (using the phase folded light-curve) in the GC by making a few assumptions and approximations. Figure 9.1 shows an imaginary phase folded light curve. Assume that there are N bins, such that each bin has width of $\frac{1}{N}$. The mean number of counts per bin $\overline{x}$ is given in equation (9.8), where n_{pred} is the number of photons detected from the GC in my analysis.

$$\overline{x} = \frac{n_{pred}}{N} \tag{9.8}$$

If we make a conservative assumption, that we can only distinguish the MSP during the on-pulse, and assuming there is no inter-pulse. Additionally, I am going to assume that the width of the pulse is around 10% of the total light curve which is typical for radio observations. Assuming that the number of counts follows a Poisson distribution such that the standard deviation

$$\sigma = \sqrt{\overline{x}} \tag{9.9}$$

I am going to define the minimum detection threshold as being emission of over 3σ above the average counts per bin as shown in equation 9.10 over the width of the radio pulse.

$$\text{Peak at } 3\ \sigma = \left(\overline{x} + 3\sqrt{\frac{n_{pred}}{N}}\right) \times 0.1N \tag{9.10}$$

So the minimum number of photons emitted from a detectable MSP, m, is

$$m = 0.1N(\overline{x} + 3\sqrt{\overline{x}}) \tag{9.11}$$

with an uncertainty of $\sqrt{m}$. I can use this to calculate P, the % of the GC that would needed to be accounted for by a MSP in order to detect it:

$$P = \left(\frac{m}{n_{pred}}\right) \times 100 \tag{9.12}$$

Furthermore, the energy flux, E, needed from a MSP in order to be detected is

$$\mathrm{E} = \frac{m}{n_{pred}} \times \text{energy flux measured from GC} \tag{9.13}$$

which can then be compared to the energy flux expected from MSP observed by *Fermi*-LAT in [9]. If the energy flux is much lower than the average energy flux (ϵ_{MSP} calculated for the MSP in [9]) it indicates that the MSP should be observable if it is emitting gamma-rays. A higher than average energy flux could indicate that only an MSP with a particularly high energy flux is likely to be resolved from within a GC.

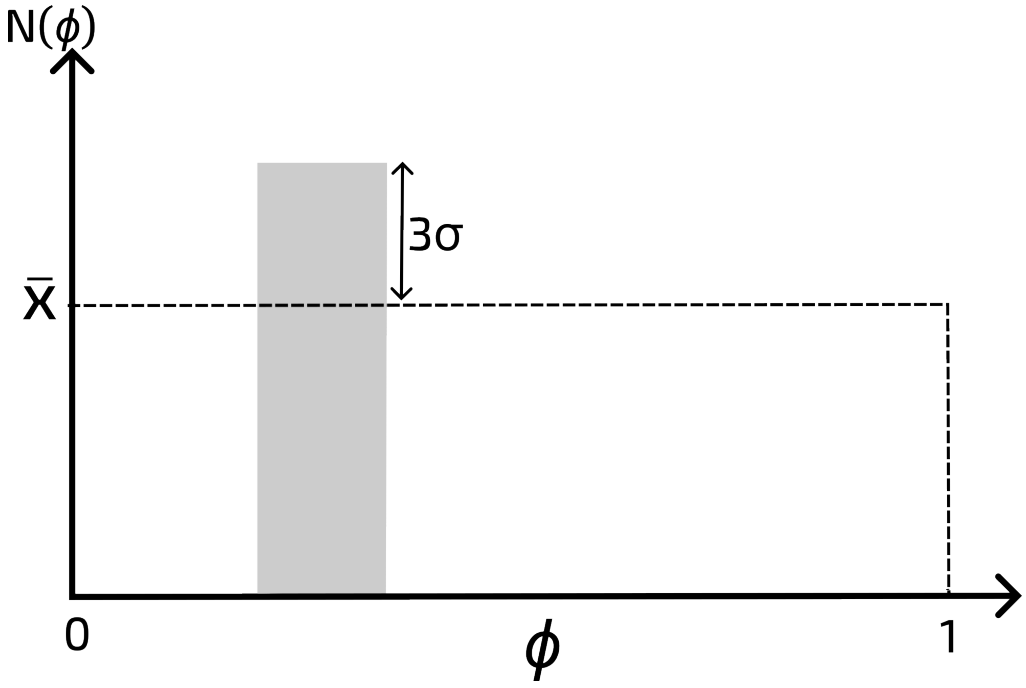

Figure 9.1: A diagram showing the expected light curve of a MSP inside a GC which is at the detection threshold. I have assumed that the MSP is only emitting above the detection threshold in the main pulse and that the main pulse is just at the detection threshold (assumed to be 3σ above the GC emission). The number of photons detected from the GC per bin is $\overline{x}$.

Results

GC	P (%)	E $\times 10^{-6}$ MeVcm^{-2}s^{-1}	% of ϵ_{MSP}
47 Tuc	12.5 ± 4.5	2.13 ± 0.10	14 ± 9
ω Cen	13.8 ± 6.7	0.93 ± 0.06	6.3 ± 5.7
Terzan 5	11.3 ± 2.4	6.0 ± 0.1	4.1 ± 1.3
NGC 7078	14.5 ± 7.7	0.38 ± 0.03	2.5 ± 2.6
NGC 6752	17.0 ± 11.0	0.35 ± 0.04	2.4 ± 3.5
NGC 6441	13.3 ± 5.9	1.1 ± 0.1	7.1 ± 5.6

Table 9.4: Table showing the percentage (P) of a GC emission needed from a single MSP in order for that MSP to be resolved in gamma-rays. The corresponding energy flux (E) and the percentage difference between E and average energy flux (ϵ_{MSP}) from the X+W model.

The results in Table 9.4 suggest that a MSP would not need to be particularly bright compared to the GC in order to detect it. We don't observe any individual MSP so this would suggest that the MSP in the GC I have studied are fainter than this. It therefore seems quite plausible that the MSP population in each GC may not account for all of the emission. These results also imply that the MSP detected in gamma-rays in NGC 6624 (as shown in Chapter 5) is unusually bright and energetic because it accounts for nearly all the GC emission [60], and quite likely atypical of MSP residing in GC.

The results of this study also suggest that the energy flux needed for a MSP to be detected is significantly smaller than ϵ_{MSP}. The comparison is shown in the fourth column of Table 9.4 but suggests that MSP in GC could be at 80% less bright than those in [9] and still be detected. This is further evidence that the MSP in GC are fainter than those in the Galactic neighbourhood. However it is important to consider that the on-pulse emission may not be quite so distinct in a GC (with all the other emission) and harder to resolve compared to isolated MSP. Additionally, if there are a number of of MSP within a GC with very similar pulse profiles it could be considerably more challenging to resolve an individual MSP.

Chapter 10

Discussion and Conclusions

10.1 Summary of Thesis

For this thesis, I selected six GC from the *Fermi* 4FGL-DR2 catalogue that have a bright gamma-ray flux, have been detected with high significance and GC where MSP have been detected and measured to produce good ephemerides. I analysed 13 years of `PASS 8` *Fermi*-LAT data within a 15° radius centred on each GC. I produced refined gamma-ray spectra of each GC and compared the relative fit of different possible spectral models conducting likelihood fits and by using the AIC criterion. I used radio ephemerides to phase-fold the gamma-ray data and produce light curves for MSP in the GCs. After using NGC 6244 (where pulsed emission had already been detected) as a test case for my methods, I found no evidence for statistically significant pulsed emission from any of the other GC. Finally, I compared the likelihood fits of a MSP only, DM only and MSP+DM fit to the spectra of each of the GC and used the results to estimate upper limits on the energy flux from MSP. In this section I present a summary of the results of this work. Based on these findings, I consider whether there is any evidence to suggest a DM component to any of the GC's gamma-ray emission.

10.2 Comments on Methodology Used

10.2.1 GC Selection Criteria

I have considered only six GC in this thesis which is a small sample, and selected them GC based on their (high) TS and energy flux. Whilst making the choice to analyse bright GC ensured that I had good photon statistics, it is possible that I may have inadvertently produced a biased sample. I have also specifically chosen GC where several MSP have been detected with radio telescopes in order to search for evidence of pulsed emission.

10.2.2 Search for Pulsed Emission

I used two statistical tests to search for evidence of pulsation in the phase folded light curves from MSP inside the GC, neither of which showed any strong evidence for any pulsed emission. These statistical tests have been used before [60] and ought to be able to resolve at least some MSP. The ephemerides of the MSP I have phase-folded appear to be good (based on data available and errors on phase) but we are still relying on

the radio MSPs emitting sufficient gamma-rays to detect them. This is an assumption because no studies to date have shown evidence for a correlation between the radio and gamma-ray emission of MSP. However, observations at gamma-ray and radio wavelengths have indicated that the MSP in GC are no different to those in our local Galactic neighbourhood [3, 113], and that the GC MSP X-ray luminosities are also consistent with the local MSP populations [61, 37].

In addition, it may be more challenging to resolve individual MSP when the population of MSP is large. For example, Terzan 5 and 47 Tuc have been observed as having particularly large MSP populations (39 and 23 respectively) and for this reason it may not be that surprising that no pulsed emission has been observed. Another study could be to look at how many 'bright' MSP we should expect to detect from GC, based on the distribution of energy fluxes of known MSPs.

10.2.3 Xing +Wang Model of MSP Spectrum

The Xing + Wang model only uses a relatively small sample of MSPs (39 in total) [134] which, at the time the study was published, were all of the MSP individually detected by *Fermi*-LAT [9]. Since then, many more MSP have been detected with *Fermi*-LAT, and the authors of [134] published an updated MSP model after I had completed my analysis [133]. This updated model uses the normalised spectra of 104 MSP detected with *Fermi*-LAT, and following a maximum analysis found a spectral model consistent with the findings in [134].

The energy flux and particularly distance measurements of the MSP in [9] have some large uncertainties. These uncertainties are intrinsic to many astronomical measurements and are difficult to improve on with the current telescopes available. Additionally, the MSP in the model are only those that have been individually resolved with *Fermi*-LAT which means they are all isolated MSP. Whilst there is no evidence that these MSP are any different to those residing in GC [59] it is possible nevertheless that the MSP in the Xing + Wang model are brighter in gamma-rays than the MSP populations observed in GC. To account for this, I have left the normalisation free to vary when calculating the maximum likelihood fit of the Xing+Wang model. However I am also assuming the Xing+Wang spectral shape is valid for GC MSPs; whilst there is no evidence that this is not a suitable model for the MSP in the GC it is a possible limitation.

10.2.4 Considering the Combination of DM + MSP

I have considered only a DM component consisting of one annihilation channel, a 31 $\pm$ 4 GeV DM pair/antiparticle pair annihilating into pairs of $b\bar{b}$ quarks [39]. Rather than choosing a DM profile that best fits each individual GC). The annihilation channel affects the gamma-ray spectral shape; Figure 8.3 clearly shows the spectral shapes of annihilation of DM into e^+e^- or $\mu^+\mu^-$ pairs are not consistent with any of the observed GC spectra. However, the W^+W^- and $\tau^+\tau^-$ DM annihilation channel spectra are similar in shape to the GC spectra, and in a further study, it would be possible to consider a DM model using a different annihilation channel, or a combination of channels. Additionally, the total flux from annihilation is dependent on the DM particle mass (as shown in Figure 8.4).

The choice to use the $b\bar{b}$ annihilation channel is motivated by evidence from previous studies of 47 Tuc [40] and of ω Centauri [39], these studies made different assumptions about the DM density profile[1] and also made no assumption regarding the annihilation cross-section. Both studies found consistent results for the best fit DM mass and interaction cross-section. Additionally, observations of the Galactic Centre in [74] also found the best fit DM to be consistent with these results. The fact that these three studies independently produce a consistent best-fit DM mass, whilst making different assumptions in different objects suggests that this was a good choice.

The combined 'DM+MSP' model fit means that assumptions regarding the relative emission in the number of MSP or their relative emission strengths within the GC can be relaxed: it does not rely on radio observations to have detected all the MSP, nor does it assume that all the MSP have the same energy flux (which was necessary when placing a statistical upper limit on the MSP emission). However there is still an assumption that the spectral shape of the MSP is consistent with the Xing + Wang model [134]. I have also only considered the potential contributions of DM and MSP : there could be additional components such as a contribution from low mass X-ray binary stars [70] (which are believed to be progenitors of MSPs [56]), and of course the diffuse Galactic emission background may contribute to the observed emission from some GCs.

10.2.5 Energy Flux Comparisons and Statistical Estimation

There is an uncertainty on the number of MSP in each GC that is difficult to quantify. For example, 10 new MSPs were discovered in ω Centauri whilst writing this thesis [55]. This uncertainty is likely to differ between GC depending on the radio surveys that have been completed. There are again large uncertainties on the energy flux due to the uncertainties in the Xing+Wang model.

I have assumed that the MSPs are 'equal emitters' within each GC when making statistical comparisons and we know that this is not always the case. I demonstrated this in Chapter 5 for NGC 6624, 10 MSP have been detected in this GC, however pulsed emission has only been detected from one MSP, which seems to account for the GC emission (if the MSP were 'equal emitters' then we would expect each MSP to account for around 10% of the GC emission.

10.3 Summary of Evidence for the Presence of DM in each GC

The evidence for DM in each GC can be evaluated by comparing the results of the different analyses techniques I have used. In Table 10.1 I compare the results I obtained for each GC by considering the following factors:

1. The preferred model for the spectrum, indicates whether a model with a DM component is significantly preferred or not. If the 'DM only' and 'DM+MSP' models cannot be distinguished then this could imply that the GC emission is DM dominated. On the other hand, the relative likelihoods of the models could be similar because we do not have sufficient photon statistics to separate them

[1] 47 Tuc's DM distribution was fitted assuming the observed gamma-ray emission from is enhanced around an IMBH at its centre, producing a 'spiky' DM distribution around it. ω Centauri's DM distribution was fitted assuming a Navarro-Frenk-White (NFW) profile [98] with an IMBH at the centre

2. The upper limit (UL) on the MSP energy flux (derived by estimating the energy flux from the MSP component of the 'DM+MSP' model) indicates if DM is likely to be a significant contributor to the gamma-ray emission

3. If any of the preferred models (DM/MSP/DM+MSP) have an energy flux consistent with the measured energy flux this indicates whether there might be additional sources of emission

4. If fewer MSP have been detected than expected on the basis of the gamma-ray flux then perhaps DM could account for the discrepancy between the observed and expected energy flux.

5. The statistical upper limit on the MSP flux cannot be used as direct evidence for the presence of DM. However it does indicate what proportion of the GC emission cannot be accounted for by MSPs and whether or not another source of emission (such as DM) is required.

GC	Preferred model(s)	UL on MSP contribution from model (%)	Do preferred model(s) account for energy flux?	O vs. E MSP	Statistical UL on MSP emission based on observed MSP population (%)
ω Centauri	DM, DM+MSP	16.0 ± 23.9	Yes	O > E	21 ± 4
47 Tuc	DM+MSP	55.0 ± 4.5	DM+MSP	O > E	19 ± 3
NGC 7078	No preferred model	29.6 ± 29.9	No	O $\approx$ E	19 ± 5
NGC 6752	DM, DM+MSP	111.2 ± 43.4	Yes	O $\approx$ E	30 ± 6
NGC 6441	No preferred model	37.9 ± 51.1	DM+MSP, MSP	O < E	19 ± 5
Terzan 5	MSP, DM+MSP	86.9 ± 7.51	Yes	O < E	11 ± 2

Table 10.1: A summary of the evidence for DM in the GC I have studied based on the preferred physical model (in Chapter 8), the Upper Limits (UL) on the (%) MSP contribution to the energy flux from the 'DM+MSP' model from Table 8.13, whether the preferred models in column 2 are consistent with the measured energy flux from Table 8.14, a comparison between the observed (O) and expected (E) number of MSP based on the expected energy flux from Table 9.1, and a statistical upper limit on the MSP contribution (from the number of observed MSP) based on no detection from Table 9.3.

The results in Table 10.1 imply that a DM component cannot be ruled out for any of the GC I have studied. However ω Centauri, 47 Tuc are most likely to have a significant DM component. NGC 6752 appears next likely to contain a DM component, but is a fainter GC and therefore there is less conclusive evidence. Whilst Terzan 5 and NGC 6441 may have a DM component, the emission could also be accounted for by MSP. NGC 7078's spectrum is not consistent with gamma-ray emission from DM or MSP.

1. ω Centauri: The models containing a DM component are significantly preferred over a MSP only emission model, and both the 'DM' and 'DM+MSP' models have energy fluxes consistent with the GC measured value. The upper limits (in the

second and fifth columns of Table 10.1) on the MSP GC contribution are consistent with each other and imply that the MSP could (at most) account for 40% of ω Centauri's emission, suggesting that ω Centauri could in fact be dominated by DM emission. This supports the findings by [39] and it is also an interesting result because there is substantial evidence that ω Centauri is an evolved dSphy [27, 32, 100]: objects which are thought to contain DM but are too faint (due to their distance) to detect using gamma-rays. The finding that there are more MSP than are expected to account for the emission also suggests that they are fainter than those in [9] and that there could be a new sub-population of MSP inside ω Centauri, further study would be needed to determine if this is the case. There is also evidence of an IMBH in this GC [128], which, if present, would potentially cause the 'spiky' DM profile [82].

2. 47 Tuc: The model containing contributions of DM and MSP emission is significantly preferred over the 'MSP' only and 'DM' only models. The 'DM+MSP' model also has an energy flux consistent with that measured in my analysis. It is also clear from the spectral shape (seen in Figure 8.6) that neither the 'DM' or 'MSP' only models can describe 47 Tuc's emission below 1000 MeV, which is the reason the 'DM+MSP' is preferred statistically. These findings show that a combination of DM and MSP could account for all 47 Tuc's gamma-ray emission and the UL on the MSP energy flux implies that DM and MSP both could contribute around 50% of the energy flux. The UL on the % MSP energy flux (based on the 'DM+MSP' model) is much higher than than the statistical UL on the % MSP contribution, however both UL indicate that I cannot rule out that DM could contribute at least 40% of the gamma-ray emission. As observed for ω Centauri, the MSP appear fainter than expected. There is also evidence that 47 Tuc contains an IMBH [79] that has allowed for enhanced DM annihilation rates to produce observable gamma-ray emission.

3. NGC 7078: NGC 7078 is much fainter than other GC I have studied which may be the main reason analysis is inconclusive and for the large uncertainties on both the 'DM+MSP' model UL and the statistical UL for MSP emission. The spectral shape shown in Figure 8.7 is inconsistent with a 'MSP' emission model and therefore MSPs are unlikely to be the dominant source of gamma-ray emission in NGC 7078, especially since there is no evidence of significant pulsed emission. However, NGC 7078's spectral shape is not consistent with either the 'DM' only or 'DM+MSP' models so it appears unlikely that NGC 7078 has a similar DM component to either ω Centauri or 47 Tuc. There is no evidence that NGC 7078 is an evolved dSphy, nor that it contains an IMBH. It is possible that DM could be present, but the annihilation rate is too low to detect, or that a different DM model (not based on the presence of an IMBH) would be more appropriate. It is interesting that the number of MSP observed is consistent with that expected: but none of them can be detected individually.

4. NGC 6752: The number of MSPs is consistent with the number expected to account for emission) yet I cannot detect any individually. The UL on MSP emission has large uncertainties, but the energy flux for a DM+MSP model is consistent with the measured value. There is therefore insufficient evidence to discount the

possibility of a DM contribution to emission. There is some evidence of an IMBH inside NGC 6752 [49] but no evidence it is an evolved dSphy, which could mean that NGC 6752 is likely to contain a smaller proportion of DM compared to ω Centauri.

5. NGC 6441: None of the models can be distinguished statistically by the AIC or by the TS values. The 'DM+MSP' and 'MSP' models have an energy flux consistent with the measured value, the fact that the 'DM' only model cannot account for the measured energy flux strongly suggests that even if DM is present in NGC 6441, there are other gamma-ray sources, which could well include MSP. There are very large uncertainties on the MSP UL (in the third column of Table 10.1), which is due to NGC 6441's spectrum having fewer significant spectral bins (compared to 47 Tuc for example). The number of observed MSP is smaller than expected, however NGC 6441 has a smaller Galactic latitude than some of the other GC I have studied: it is harder to detect MSP using radio waves closer to the Galactic plane because of dispersion, and it is entirely possible that are some undetected MSP in this GC. NGC 6441 has been identified as a promising candidate for containing an IMBH (because of its high mass) however studies so far have been inconclusive [68].

6. Terzan 5: The results in Table 10.1 suggest that a high proportion of the GC emission can be attributed to MSP. There is a large discrepancy between the UL on the MSP emission from the 'DM+MSP' models and the statistical UL, and given that the number of MSP observed is much smaller than expected could suggest that there are a number of undetected MSP in Terzan 5. MSP timing measurements have also enabled upper limits to be placed on a potential IMBH in Terzan 5 [108] and it is therefore possible that any DM annihilation in Terzan 5 is not enhanced (and therefore there is less gamma-ray emission from the DM) compared to ω Centauri for example.

10.4 Ideas for Further Studies

There are a number of possible avenues of further research that could be investigated relating to the analysis I have completed in this thesis, I have outlined some of them below:

1. I have analysed only a small subset of GC. In the future, all of the *Fermi*-LAT GC could be analysed, In some GC, no MSP have so far been detected (for example the GLIMPSE GC listed in Table 3.1). Comparing the results of a maximum likelihood fit of the 'DM' only, 'MSP' only, and 'DM+MSP' models may assist in estimating the number of MSP, even if the MSP are too faint to resolve in gamma-rays.

2. More extensive radio surveys are needed in order to more accurately determine the number of MSPs within each GC. This should be possible with the new radio telescopes such as MeerKAT [55]. If the number of MSP observed is larger than expected (based on the energy flux) in more GC then this would provide more evidence to suggest that in some GC, the MSP are weaker gamma-ray emitters than the general Galactic population of MSP.

3. The discrepancy between the number of MSP observed and expected in some GC I have studied could be interpreted as evidence that perhaps the MSP populations in some GC are intrinsically different, which could be because they have somehow evolved differently to the MSP in [9]. Further studies investigating the evolution of MSP are needed.

4. In this work I have considered only DM as an alternative source of gamma-ray emission in GC. There are other potential gamma-ray sources that could be contributing to the emission such as low mass X-Ray binary stars [70] or shocked material from within the GC [125] .

5. MSPs in GC are initially detected at radio wavelengths because *Fermi*-LAT does not have sufficient angular resolution to pick out individual MSPs inside GC. 'Blind' searches have detected some (isolated) MSP that had not been detected at radio wavelengths [111]. More blind searches could help to better determine whether there is a correlation between the radio and gamma-ray emission from MSP. This may help establish if it is likely that there are MSP in GC that are bright gamma-ray emitters, but are below the detection threshold for radio detection[2].

6. As I have already mentioned, in this work I have considered only one DM annihilation channel. It would be possible to calculate the best-fit DM mass, and annihilation channel(s) for each GC in a maximum likelihood analysis. It will be interesting to see whether the result is consistent with findings in studies such as [40, 39]

7. Studies investigating the origin of the observed gamma-ray excess from the Galactic Centre have so far not identified the source of gamma-rays. The two leading hypotheses are an unresolved population of MSP [25], or DM annihilation [64]. The studies have been unable to determine whether the emission from the Galactic centre is smooth (which would be evidence of DM annihilation) or from point sources (which would be evidence of emission from MSP) [91, 86]. In my analysis, I have found some evidence that the MSP in GC appear to be weaker gamma-ray emitters than expected. A population of fainter MSPs may look even more similar to DM annihilation than MSP from the general Galactic population. If the MSP in GC are indeed fainter, then a new MSP model containing MSP in GC could be applied to the Galactic centre. It should be possible to determine how many of these 'faint' MSP would be needed to account for the emission from the Galactic centre, and whether this seems plausible.

8. It has been suggested that the majority of gamma-ray MSP also emit at radio wavelengths [67]. However, perhaps this is not as strongly correlated as previously thought: perhaps some MSP emit strongly in radio waves but not in gamma-rays. X-ray studies of GC MSP (such as [57]) may help to determine to what extent the high energy and radio emission are correlated.

9. I have already estimated on the MSP energy flux from each GC. A similar calculation could be done to calculate the energy flux from annihilating DM. This

[2]Blind gamma-ray searches would also help determine whether the MSP had not yet been detected because their radio emission is too weak, or because their position means that the signal is too distorted by dispersion to be detected.

could be used to estimate the potential mass of DM in each GC under various assumptions about the interaction cross-section. The consistency of mass with the estimated GC mass could be checked, based on the visible matter and the estimated mass based on the stellar encounter rate and dynamics within the GC. It may also be possible to look for evidence of gravitational microlensing effects from the GC (initial studies in [78] have already investigated the possibility of using this technique from 47 Tuc), to estimate the GC mass.

10. As I discussed in Chapter 6, Terzan 5 is currently the only GC with associated VHE emission. HESS has placed an upper limit on the possible VHE emission from 47 Tuc [17] and NGC 7078 [13]. Surveys with CTA may be able to determine if 47 Tuc (and other GC) have any VHE that has not yet been detected, and place more stringent upper-limits on the emission. The presence of VHE (or lack of) indicates the processes occurring in the GC and the types of sources likely to be present.

Bibliography

[1] Benjamin P Abbott et al. "First search for gravitational waves from known pulsars with Advanced LIGO". In: *The Astrophysical Journal* 839.1 (2017), p. 12.

[2] A. A. Abdo et al. "A Population of Gamma-Ray Millisecond Pulsars Seen with the Fermi Large Area Telescope". In: *Science* 325.5942 (2009), pp. 848–852. DOI: 10.1126/science.1176113.

[3] A. A. Abdo et al. "Detection of 16 Gamma-Ray Pulsars Through Blind Frequency Searches Using the Fermi LAT". In: *Science* 325.5942 (Aug. 2009), p. 840. DOI: 10.1126/science.1175558. arXiv: 1009.0748 [astro-ph.GA].

[4] A. A. Abdo et al. "Detection of High-Energy Gamma-Ray Emission from the Globular Cluster 47 Tucanae with Fermi". In: *Science* 325.5942 (2009), pp. 845–848. DOI: 10.1126/science.1177023. eprint: https://www.science.org/doi/pdf/10.1126/science.1177023. URL: https://www.science.org/doi/abs/10.1126/science.1177023.

[5] A. A. Abdo et al. "Detection of High-Energy Gamma-Ray Emission from the Globular Cluster 47 Tucanae with Fermi". In: *Science* 325.5942 (2009), pp. 845–848. DOI: 10.1126/science.1177023. eprint: https://www.science.org/doi/pdf/10.1126/science.1177023. URL: https://www.science.org/doi/abs/10.1126/science.1177023.

[6] A. A. Abdo et al. "Gamma-Ray Emission from the Shell of Supernova Remnant W44 Revealed by the Fermi LAT". In: *Science* 327.5969 (2010), pp. 1103–1106. DOI: 10.1126/science.1182787. eprint: https://www.science.org/doi/pdf/10.1126/science.1182787. URL: https://www.science.org/doi/abs/10.1126/science.1182787.

[7] A. A. Abdo et al. "PSR J0007+7303 in the CTA Supernova Remnant: New Gamma-Ray results from two years of Fermi Large Area Telescope Observations". In: *The Astrophysical Journal* 744.2 (Dec. 2011), p. 146. DOI: 10.1088/0004-637x/744/2/146. URL: https://doi.org/10.1088/0004-637x/744/2/146.

[8] A. A. Abdo et al. "Pulsed Gamma Rays from the Millisecond Pulsar J0030+0451 with the Fermi Large Area Telescope". In: 699.2 (July 2009), pp. 1171–1177. DOI: 10.1088/0004-637X/699/2/1171. arXiv: 0904.4377 [astro-ph.HE].

[9] A. A. Abdo et al. "The Second Fermi Large Area Telescope Catalog of Gamma-Ray Pulsars". In: *apjs* 208.2, 17 (Oct. 2013), p. 17. DOI: 10.1088/0067-0049/208/2/17. arXiv: 1305.4385 [astro-ph.HE].

[10] Abdo, A. A. et al. “A population of gamma-ray emitting globular clusters seen with the Fermi Large Area Telescope”. In: *A&A* 524 (2010), A75. DOI: 10.1051/0004-6361/201014458. URL: https://doi.org/10.1051/0004-6361/201014458.

[11] A. Abramowski et al. “The 2012 flare of PG1553+113 seen with H.E.S.S. and FERMI-LAT”. In: *The Astrophysical Journal* 802.1 (Mar. 2015), p. 65. DOI: 10.1088/0004-637x/802/1/65. URL: https://doi.org/10.1088%2F0004-637x%2F802%2F1%2F65.

[12] A. Abramowski et al. “Very-high-energy gamma-ray emission from the direction of the Galactic globular cluster Terzan 5”. In: *Astronomy &amp Astrophysics* 531 (July 2011), p. L18. DOI: 10.1051/0004-6361/201117171.

[13] Abramowski, A. et al. “Search for very-high-energy emission from Galactic globular clusters with H.E.S.S.” In: *A&A* 551 (2013), A26. DOI: 10.1051/0004-6361/201220719. URL: https://doi.org/10.1051/0004-6361/201220719.

[14] F. Acero et al. “Fermi Large Area Telescope Third Source Catalog”. In: *apjs* 218.2, 23 (June 2015), p. 23. DOI: 10.1088/0067-0049/218/2/23. arXiv: 1501.02003 [astro-ph.HE].

[15] M. Ackermann et al. “The Fermi Galactic Center GeV Excess and Implications for Dark Matter”. In: *The Astrophysical Journal* 840.1 (May 2017), p. 43. DOI: 10.3847/1538-4357/aa6cab. URL: https://doi.org/10.3847%2F1538-4357%2Faa6cab.

[16] *Add weights*. https://fermi.gsfc.nasa.gov/ssc/data/analysis/user/add_weights.txt. Accessed: 2022-04-30.

[17] Aharonian, F. et al. “HESS upper limit on the very high energy emission from the globular cluster 47 Tucanae”. In: *A&A* 499.1 (2009), pp. 273–277. DOI: 10.1051/0004-6361/200811564. URL: https://doi.org/10.1051/0004-6361/200811564.

[18] M. Ajello et al. “A Decade of Gamma-Ray Bursts Observed by iFermi/i-LAT: The Second GRB Catalog”. In: *The Astrophysical Journal* 878.1 (June 2019), p. 52. DOI: 10.3847/1538-4357/ab1d4e. URL: https://doi.org/10.3847%2F1538-4357%2Fab1d4e.

[19] H. Akaike. “A new look at the statistical model identification”. In: *IEEE Transactions on Automatic Control* 19.6 (1974), pp. 716–723. DOI: 10.1109/TAC.1974.1100705.

[20] A. Albert et al. “Searching for Dark Matter Annihilation in Recently Discovered Milky Way Satellites with Fermi-Lat”. In: *apj* 834.2, 110 (Jan. 2017), p. 110. DOI: 10.3847/1538-4357/834/2/110. arXiv: 1611.03184 [astro-ph.HE].

[21] N R Arakelyan, S V Pilipenko, and N I Libeskind. “Spatial distribution of globular clusters in the Galaxy”. In: *Monthly Notices of the Royal Astronomical Society* 481.1 (Aug. 2018), pp. 918–929. ISSN: 0035-8711. DOI: 10.1093/mnras/sty2320. eprint: https://academic.oup.com/mnras/article-pdf/481/1/918/25697703/sty2320.pdf. URL: https://doi.org/10.1093/mnras/sty2320.

[22] W. B. Atwood et al. "THE LARGE AREA TELESCOPE ON THE FERMI GAMMA-RAY SPACE TELESCOPE MISSION". In: *The Astrophysical Journal* 697.2 (May 2009), pp. 1071–1102. DOI: 10.1088/0004-637x/697/2/1071. URL: https://doi.org/10.1088%2F0004-637x%2F697%2F2%2F1071.

[23] Arash Bahramian et al. "STELLAR ENCOUNTER RATE IN GALACTIC GLOBULAR CLUSTERS". In: *The Astrophysical Journal* 766.2 (Mar. 2013), p. 136. DOI: 10.1088/0004-637x/766/2/136. URL: https://doi.org/10.1088/0004-637x/766/2/136.

[24] J. Ballet et al. *Fermi Large Area Telescope Fourth Source Catalog Data Release 2*. 2020. DOI: 10.48550/ARXIV.2005.11208. URL: https://arxiv.org/abs/2005.11208.

[25] Richard Bartels, Suraj Krishnamurthy, and Christoph Weniger. "Strong support for the millisecond pulsar origin of the Galactic center GeV excess". In: *Phys. Rev. Lett.* 116.5 (2016), p. 051102. DOI: 10.1103/PhysRevLett.116.051102. arXiv: 1506.05104 [astro-ph.HE].

[26] N. Bastian and J. Strader. "Constraining globular cluster formation through studies of young massive clusters – III. A lack of gas and dust in massive stellar clusters in the LMC and SMC". In: *Monthly Notices of the Royal Astronomical Society* 443.4 (Aug. 2014), pp. 3594–3600. ISSN: 0035-8711. DOI: 10.1093/mnras/stu1407. eprint: https://academic.oup.com/mnras/article-pdf/443/4/3594/6295169/stu1407.pdf. URL: https://doi.org/10.1093/mnras/stu1407.

[27] H. Baumgardt and M. Hilker. "A catalogue of masses, structural parameters, and velocity dispersion profiles of 112 Milky Way globular clusters". In: *mnras* 478.2 (Aug. 2018), pp. 1520–1557. DOI: 10.1093/mnras/sty1057. arXiv: 1804.08359 [astro-ph.GA].

[28] Michael A. Beasley. "Globular Cluster Systems and Galaxy Formation". In: *Reviews in Frontiers of Modern Astrophysics*. Springer International Publishing, 2020, pp. 245–277. DOI: 10.1007/978-3-030-38509-5_9. URL: https://doi.org/10.1007%2F978-3-030-38509-5_9.

[29] G. Beccari et al. "Discovery of a Double Blue Straggler Sequence in M15: New Insight into the Core-collapse Process". In: *apj* 876.1, 87 (May 2019), p. 87. DOI: 10.3847/1538-4357/ab13a4. arXiv: 1903.11113 [astro-ph.SR].

[30] W. Bednarek and J. Sitarek. "High-energy gamma-rays from globular clusters". In: *Monthly Notices of the Royal Astronomical Society* 377.2 (Apr. 2007), pp. 920–930. ISSN: 0035-8711. DOI: 10.1111/j.1365-2966.2007.11664.x. eprint: https://academic.oup.com/mnras/article-pdf/377/2/920/3508860/mnras0377-0920.pdf. URL: https://doi.org/10.1111/j.1365-2966.2007.11664.x.

[31] Bednarek, W. and Bartosik, M. "Gamma-rays from the pulsar wind nebulae". In: *A&A* 405.2 (2003), pp. 689–702. DOI: 10.1051/0004-6361:20030593. URL: https://doi.org/10.1051/0004-6361:20030593.

[32] K. Bekki and K. C. Freeman. "Formation of ω Centauri from an ancient nucleated dwarf galaxy in the young Galactic disc". In: *mnras* 346.2 (Dec. 2003), pp. L11–L15. DOI: 10.1046/j.1365-2966.2003.07275.x. arXiv: astro-ph/0310348 [astro-ph].

[33] Gianfranco Bertone, Dan Hooper, and Joseph Silk. "Particle dark matter: evidence, candidates and constraints". In: *physrep* 405.5-6 (Jan. 2005), pp. 279–390. DOI: 10.1016/j.physrep.2004.08.031. arXiv: hep-ph/0404175 [hep-ph].

[34] Anupam Bhardwaj et al. "Optical and Near-infrared Pulsation Properties of RR Lyrae and Population II Cepheid Variables in the Messier 15 Globular Cluster". In: *The Astrophysical Journal* 922.1 (Nov. 2021), p. 20. DOI: 10.3847/1538-4357/ac214d. URL: https://doi.org/10.3847%2F1538-4357%2Fac214d.

[35] S.J. Blundell and K.M. Blundell. *Concepts in Thermal Physics*. OUP Oxford, 2010. ISBN: 9780199562091. URL: https://books.google.co.uk/books?id=T0luBAAAQBAJ.

[36] Kimberly K. Boddy and Jason Kumar. "Minding the MeV gap: The indirect detection of low mass dark matter". In: *AIP Conference Proceedings*. Author(s), 2016. DOI: 10.1063/1.4953276. URL: https://doi.org/10.1063%5C%2F1.4953276.

[37] Slavko Bogdanov et al. "Chandra X-Ray Observations of 19 Millisecond Pulsars in the Globular Cluster 47 Tucanae". In: 646.2 (Aug. 2006), pp. 1104–1115. DOI: 10.1086/505133. arXiv: astro-ph/0604318 [astro-ph].

[38] J. Boyles et al. "Young Radio Pulsars in Galactic Globular Clusters". In: *The Astrophysical Journal* 742.1 (Nov. 2011), p. 51. DOI: 10.1088/0004-637x/742/1/51. URL: https://doi.org/10.1088%2F0004-637x%2F742%2F1%2F51.

[39] Anthony M. Brown et al. *The glow of annihilating dark matter in Omega Centauri*. 2019. DOI: 10.48550/ARXIV.1907.08564. URL: https://arxiv.org/abs/1907.08564.

[40] Anthony M. Brown et al. "Understanding the γ -ray emission from the globular cluster 47 Tuc: Evidence for dark matter?" In: *Physical Review D* 98.4 (Aug. 2018). DOI: 10.1103/physrevd.98.041301. URL: https://doi.org/10.1103%2Fphysrevd.98.041301.

[41] P. Bruel. "Extending the event-weighted pulsation search to very faint gamma-ray sources". In: *aap* 622, A108 (Feb. 2019), A108. DOI: 10.1051/0004-6361/201834555. arXiv: 1812.06681 [astro-ph.IM].

[42] Matthew Buckley and Dan Hooper. "Dark Matter Subhalos In the Fermi First Source Catalog". In: *Physical Review D* 82 (Apr. 2010). DOI: 10.1103/PHYSREVD.82.063501.

[43] P. M. Chadwick, I. J. Latham, and S. J. Nolan. "Topical Review: TeV gamma-ray astronomy". In: *Journal of Physics G Nuclear Physics* 35.3, 033201 (Mar. 2008), p. 033201. DOI: 10.1088/0954-3899/35/3/033201.

[44] Seery Chen et al. "Distances to the Globular Clusters 47 Tucanae and NGC 362 Using Gaia DR2 Parallaxes". In: *The Astrophysical Journal* 867.2 (Nov. 2018), p. 132. DOI: 10.3847/1538-4357/aae089. URL: https://doi.org/10.3847%2F1538-4357%2Faae089.

[45] J Clear et al. "A detailed analysis of the high energy gamma-ray emission from the Crab pulsar and nebula". In: *Astronomy and Astrophysics* 174 (1987), pp. 85–94.

[46] Pulsars in globular clusters. *P.Freire*. 2022. URL: http://www.naic.edu/~pfreire/GCpsr.html.

[47] NASA/DOE/Fermi LAT Collaboration. *Fermi Bubbles*. URL: https://fermi.gsfc.nasa.gov/science/constellations/pages/bubbles.html.

[48] NASA/DOE/Fermi LAT Collaboration. *Fermi's Five-year View of the Gamma-ray Sky*. URL: https://svs.gsfc.nasa.gov/11342.

[49] Monica Colpi, Alessia Gualandris, and Andrea Possenti. *Is NGC6752 hiding a double black hole binary in its core ?* 2002. DOI: 10.48550/ARXIV.ASTRO-PH/0209393. URL: https://arxiv.org/abs/astro-ph/0209393.

[50] Peter Creasey et al. "Globular clusters formed within dark haloes I: present-day abundance, distribution, and kinematics". In: 482.1 (Jan. 2019), pp. 219–230. DOI: 10.1093/mnras/sty2701. arXiv: 1806.11118 [astro-ph.GA].

[51] Shi Dai et al. "Discovery of Millisecond Pulsars in the Globular Cluster Omega Centauri". In: *apjl* 888.2, L18 (Jan. 2020), p. L18. DOI: 10.3847/2041-8213/ab621a. arXiv: 1912.08079 [astro-ph.HE].

[52] Shi Dai et al. "Discovery of Millisecond Pulsars in the Globular Cluster Omega Centauri". In: *The Astrophysical Journal* 888.2 (Jan. 2020), p. L18. DOI: 10.3847/2041-8213/ab621a. URL: https://doi.org/10.3847%2F2041-8213%2Fab621a.

[53] Kris Davidson and Yervant Terzian. "Dispersion Measures of Pulsars". In: 74 (Sept. 1969), p. 849. DOI: 10.1086/110872.

[54] de Jager, O. C. and Büsching, I. "The H-test probability distribution revisited: improved sensitivity". In: *A&A* 517 (2010), p. L9. DOI: 10.1051/0004-6361/201014362. URL: https://doi.org/10.1051/0004-6361/201014362.

[55] ebarr@mpifr-bonn.mpg.de. *TRAPUM*. URL: http://trapum.org/discoveries/. (accessed: 16.05.2022).

[56] É Érgma and AG Masevich. "Low-mass x-ray binaries and millisecond pulsars". In: *Astrophysics* 36.1 (1993), pp. 82–101.

[57] L. M. Forestell et al. "A Chandra look at the X-ray faint millisecond pulsars in the globular cluster NGC 6752". In: *mnras* 441.1 (June 2014), pp. 757–768. DOI: 10.1093/mnras/stu559. arXiv: 1403.4624 [astro-ph.HE].

[58] Elaine C. F. S. Fortes et al. "What could be the observational signature of dark matter in globular clusters?" In: *jcap* 2020.8, 010 (Aug. 2020), p. 010. DOI: 10.1088/1475-7516/2020/08/010. arXiv: 1912.12262 [astro-ph.HE].

[59] P. C. Freire et al. "Further results from the timing of the millisecond pulsars in 47 Tucanae". In: *mnras* 340.4 (Apr. 2003), pp. 1359–1374. DOI: 10.1046/j.1365-8711.2003.06392.x.

[60] P. C. C. Freire et al. "Fermi Detection of a Luminous γ-Ray Pulsar in a Globular Cluster". In: *Science* 334.6059 (Nov. 2011), p. 1107. DOI: 10.1126/science.1207141. arXiv: 1111.3754 [astro-ph.GA].

[61] P. C. C. Freire et al. "Long-term observations of the pulsars in 47 Tucanae - II. Proper motions, accelerations and jerks". In: *mnras* 471.1 (Oct. 2017), pp. 857–876. DOI: 10.1093/mnras/stx1533. arXiv: 1706.04908 [astro-ph.HE].

[62] Stefan Funk. "Ground and Space-Based Gamma-Ray Astronomy". In: *Annual Review of Nuclear and Particle Science* 65.1 (2015), pp. 245–277. DOI: 10.1146/annurev-nucl-102014-022036. eprint: https://doi.org/10.1146/annurev-nucl-102014-022036. URL: https://doi.org/10.1146/annurev-nucl-102014-022036.

[63] Stefan Funk. "Indirect detection of dark matter with gamma-rays". In: *Proceedings of the National Academy of Sciences* 112.40 (2015), pp. 12264–12271. DOI: 10.1073/pnas.1308728111. eprint: https://www.pnas.org/doi/pdf/10.1073/pnas.1308728111. URL: https://www.pnas.org/doi/abs/10.1073/pnas.1308728111.

[64] Lisa Goodenough and Dan Hooper. *Possible Evidence For Dark Matter Annihilation In The Inner Milky Way From The Fermi Gamma Ray Space Telescope*. DOI: 10.48550/ARXIV.0910.2998. URL: https://arxiv.org/abs/0910.2998.

[65] Chris Gordon and Oscar Macías. "Dark matter and pulsar model constraints from Galactic Center Fermi-LAT gamma-ray observations". In: *Phys. Rev. D* 88 (8 Oct. 2013), p. 083521. DOI: 10.1103/PhysRevD.88.083521. URL: https://link.aps.org/doi/10.1103/PhysRevD.88.083521.

[66] Raffaele Gratton et al. "What is a globular cluster? An observational perspective". In: *The Astronomy and Astrophysics Review* 27.1 (Nov. 2019). DOI: 10.1007/s00159-019-0119-3. URL: https://doi.org/10.1007%5C%2Fs00159-019-0119-3.

[67] Guillemot, L. et al. "The gamma-ray millisecond pulsar deathline, revisited - New velocity and distance measurements". In: *A&A* 587 (2016), A109. DOI: 10.1051/0004-6361/201527847. URL: https://doi.org/10.1051/0004-6361/201527847.

[68] Maximilian Häberle et al. "Hunting for intermediate-mass black holes in globular clusters: an astrometric study of NGC 6441". In: *Monthly Notices of the Royal Astronomical Society* 503.1 (Feb. 2021), pp. 1490–1506. DOI: 10.1093/mnras/stab474. URL: https://doi.org/10.1093%2Fmnras%2Fstab474.

[69] T. H. Hankins and J. M. Cordes. "Interpulse emission from pulsar 0950+08 : how many poles ?" In: *apj* 249 (Oct. 1981), pp. 241–253. DOI: 10.1086/159281.

[70] Max Harvey, Cameron Rulten, and Paula Chadwick. "The X-Ray Binary Population with Fermi-LAT". In: *Proceedings of 37th International Cosmic Ray Conference — PoS(ICRC2021)*. Sissa Medialab, July 2021. DOI: 10.22323/1.395.0621. URL: https://doi.org/10.22323%5C%2F1.395.0621.

[71] W Hermsen. "COS-B views on the diffuse galactic gamma-ray emission and some point sources." In: *Space Science Reviews* (1989). URL: https://doi.org/10.1007/BF00173739.

[72] Antony Hewish et al. "74. Observation of a Rapidly Pulsating Radio Source". In: *A Source Book in Astronomy and Astrophysics, 1900–1975*. Harvard University Press, 2013, pp. 498–504.

[73] G. B. Hobbs, R. T. Edwards, and R. N. Manchester. "TEMPO2, a new pulsar-timing package - I. An overview". In: *mnras* 369.2 (June 2006), pp. 655–672. DOI: 10.1111/j.1365-2966.2006.10302.x. arXiv: astro-ph/0603381 [astro-ph].

[74] Dan Hooper and Tim Linden. "Origin of the gamma rays from the Galactic Center". In: *Phys. Rev. D* 84 (12 Dec. 2011), p. 123005. DOI: 10.1103/PhysRevD.84.123005. URL: https://link.aps.org/doi/10.1103/PhysRevD.84.123005.

[75] B. A. Jacoby et al. "Measurement of Orbital Decay in the Double Neutron Star Binary PSR B2127+11C". In: *apjl* 644.2 (June 2006), pp. L113–L116. DOI: 10.1086/505742. arXiv: astro-ph/0605375 [astro-ph].

[76] T. J. Johnson et al. "BROADBAND PULSATIONS FROM PSR B1821–24: IMPLICATIONS FOR EMISSION MODELS AND THE PULSAR POPULATION OF M28". In: *The Astrophysical Journal* 778.2 (Nov. 2013), p. 106. DOI: 10.1088/0004-637x/778/2/106. URL: https://doi.org/10.1088/0004-637x/778/2/106.

[77] M. Kerr. "Improving Sensitivity to Weak Pulsations with Photon Probability Weighting". In: *apj* 732.1, 38 (May 2011), p. 38. DOI: 10.1088/0004-637X/732/1/38. arXiv: 1103.2128 [astro-ph.IM].

[78] Fulya Kıroğlu et al. "Gravitational Microlensing Rates in Milky Way Globular Clusters". In: *The Astrophysical Journal* 928.2 (Apr. 2022), p. 181. DOI: 10.3847/1538-4357/ac5895. URL: https://doi.org/10.3847/1538-4357/ac5895.

[79] Bülent Kızıltan, Holger Baumgardt, and Abraham Loeb. "An intermediate-mass black hole in the centre of the globular cluster 47 Tucanae". In: *Nature* 542.7640 (Feb. 2017), pp. 203–205. DOI: 10.1038/nature21361. URL: https://doi.org/10.1038%2Fnature21361.

[80] A. K. H. Kong, C. Y. Hui, and K. S. Cheng. "FERMI DISCOVERY OF GAMMA-RAY EMISSION FROM THE GLOBULAR CLUSTER TERZAN 5". In: *The Astrophysical Journal* 712.1 (Feb. 2010), pp. L36–L39. DOI: 10.1088/2041-8205/712/1/l36. URL: https://doi.org/10.1088/2041-8205/712/1/l36.

[81] A. K. H. Kong, C. Y. Hui, and K. S. Cheng. "Fermi Discovery of Gamma-ray Emission from the Globular Cluster Terzan 5". In: 712.1 (Mar. 2010), pp. L36–L39. DOI: 10.1088/2041-8205/712/1/L36. arXiv: 1002.2431 [astro-ph.HE].

[82] Thomas Lacroix, Cé line Bœhm, and Joseph Silk. "Ruling out thermal dark matter with a black hole induced spiky profile in the M87 galaxy". In: *Physical Review D* 92.4 (Aug. 2015). DOI: 10.1103/physrevd.92.043510. URL: https://doi.org/10.1103%2Fphysrevd.92.043510.

[83] B. Lanzoni et al. "NEW DENSITY PROFILE AND STRUCTURAL PARAMETERS OF THE COMPLEX STELLAR SYSTEM TERZAN 5". In: *The Astrophysical Journal* 717.2 (June 2010), pp. 653–657. DOI: 10.1088/0004-637x/717/2/653. URL: https://doi.org/10.1088%2F0004-637x%2F717%2F2%2F653.

[84] LAT Collaboration et al. *Incremental Fermi Large Area Telescope Fourth Source Catalog*. 2022. DOI: 10.48550/ARXIV.2201.11184. URL: https://arxiv.org/abs/2201.11184.

[85] Rebecca K. Leane. *Indirect Detection of Dark Matter in the Galaxy*. 2020. DOI: 10.48550/ARXIV.2006.00513. URL: https://arxiv.org/abs/2006.00513.

[86] Rebecca K. Leane and Tracy R. Slatyer. "Revival of the Dark Matter Hypothesis for the Galactic Center Gamma-Ray Excess". In: 123.24, 241101 (Dec. 2019), p. 241101. DOI: 10.1103/PhysRevLett.123.241101.

[87] Fraser Lewis, Adam Butler, and Lucy Gilbert. "A unified approach to model selection using the likelihood ratio test". In: *Methods in Ecology and Evolution* 2.2 (2011), pp. 155–162. DOI: https://doi.org/10.1111/j.2041-210X.2010.00063.x. eprint: https://besjournals.onlinelibrary.wiley.com/doi/pdf/10.1111/j.2041-210X.2010.00063.x. URL: https://besjournals.onlinelibrary.wiley.com/doi/abs/10.1111/j.2041-210X.2010.00063.x.

[88] Sheridan J Lloyd, Paula M Chadwick, and Anthony M Brown. "Gamma-ray emission from high Galactic latitude globular clusters". In: *Monthly Notices of the Royal Astronomical Society* (Aug. 2018). DOI: 10.1093/mnras/sty2150. URL: https://doi.org/10.1093%5C%2Fmnras%5C%2Fsty2150.

[89] Malcolm S. Longair. *High Energy Astrophysics*. 2011.

[90] Andrew Lyne and Francis Graham-Smith. *Pulsar Astronomy*. 4th ed. Cambridge Astrophysics. Cambridge University Press, 2012. DOI: 10.1017/CBO9780511844584.

[91] Oscar Macias et al. "Galactic bulge preferred over dark matter for the Galactic centre gamma-ray excess". In: *Nature Astronomy* 2.5 (Mar. 2018), pp. 387–392. DOI: 10.1038/s41550-018-0414-3. URL: https://doi.org/10.1038%2Fs41550-018-0414-3.

[92] R. N. Manchester. "Millisecond Pulsars, their Evolution and Applications". In: *Journal of Astrophysics and Astronomy* 38.3 (Sept. 2017). DOI: 10.1007/s12036-017-9469-2. URL: https://doi.org/10.1007%2Fs12036-017-9469-2.

[93] J. R. Mattox et al. "The Likelihood Analysis of EGRET Data". In: *apj* 461 (Apr. 1996), p. 396. DOI: 10.1086/177068.

[94] Nestor Miraba. *Source Model Definitions for gtlike*. 2018. URL: https://fermi.gsfc.nasa.gov/ssc/data/analysis/scitools/source_models.html.

[95] L. Monaco et al. "Wide-field photometry of the Galactic globular cluster M22". In: *Monthly Notices of the Royal Astronomical Society* 349.4 (Apr. 2004), pp. 1278–1290. DOI: 10.1111/j.1365-2966.2004.07599.x. URL: https://doi.org/10.1111%2Fj.1365-2966.2004.07599.x.

[96] NASA. *Fermi Spacecraft and Instruments*. URL: https://www.nasa.gov/content/goddard/fermi-spacecraft-and-instruments.

[97] NASA. *LAT Photon, Event, and Spacecraft Data Query*. 2022. URL: https://fermi.gsfc.nasa.gov/cgi-bin/ssc/LAT/LATDataQuery.cgi.

[98] Julio F. Navarro, Carlos S. Frenk, and Simon D. M. White. "The Structure of Cold Dark Matter Halos". In: *The Astrophysical Journal* 462 (May 1996), p. 563. DOI: 10.1086/177173. URL: https://doi.org/10.1086%2F177173.

[99] H. Ndiyavala et al. "Probing the Pulsar Population of Terzan 5 via Spectral Modeling". In: *The Astrophysical Journal* 880.1 (July 2019), p. 53. DOI: 10.3847/1538-4357/ab24ca. URL: https://doi.org/10.3847%2F1538-4357%2Fab24ca.

[100] Eva Noyola, Karl Gebhardt, and Marcel Bergmann. "Gemini and Hubble Space Telescope Evidence for an Intermediate-Mass Black Hole in ω Centauri". In: *apj* 676.2 (Apr. 2008), pp. 1008–1015. DOI: 10.1086/529002. arXiv: 0801.2782 [astro-ph].

[101] R. A. P. Oliveira et al. “Precise distances from OGLE-IV member RR Lyrae stars in six bulge globular clusters”. In: *Astronomy &amp Astrophysics* 657 (Jan. 2022), A123. DOI: 10.1051/0004-6361/202141596. URL: https://doi.org/10.1051%2F0004-6361%2F202141596.

[102] L. Origlia et al. “Variable Stars in Terzan 5: Additional Evidence of Multi-age and Multi-iron Stellar Populations”. In: *The Astrophysical Journal* 871.1 (Jan. 2019), p. 114. DOI: 10.3847/1538-4357/aaf730. URL: https://doi.org/10.3847/1538-4357/aaf730.

[103] J. L. Palfreyman et al. “TEMPORAL EVOLUTION OF THE VELA PULSAR’S PULSE PROFILE”. In: *The Astrophysical Journal* 820.1 (Mar. 2016), p. 64. DOI: 10.3847/0004-637x/820/1/64. URL: https://doi.org/10.3847%2F0004-637x%2F820%2F1%2F64.

[104] R. C. Peterson and D. W. Latham. “Stellar Velocity Dispersions for Four Low-Concentration Globular Clusters”. In: 305 (June 1986), p. 645. DOI: 10.1086/164278.

[105] Planck Collaboration et al. “Planck 2015 results. XIII. Cosmological parameters”. In: *aap* 594, A13 (Sept. 2016), A13. DOI: 10.1051/0004-6361/201525830. arXiv: 1502.01589 [astro-ph.CO].

[106] H. C. Plummer. “On the problem of distribution in globular star clusters”. In: 71 (Mar. 1911), pp. 460–470. DOI: 10.1093/mnras/71.5.460.

[107] Posti, Lorenzo and Helmi, Amina. “Mass and shape of the Milky Way´s dark matter halo with globular clusters from Gaia and Hubble”. In: *A&A* 621 (2019), A56. DOI: 10.1051/0004-6361/201833355. URL: https://doi.org/10.1051/0004-6361/201833355.

[108] Brian J. Prager et al. “Using Long-term Millisecond Pulsar Timing to Obtain Physical Characteristics of the Bulge Globular Cluster Terzan 5”. In: *The Astrophysical Journal* 845.2 (Aug. 2017), p. 148. DOI: 10.3847/1538-4357/aa7ed7. URL: https://doi.org/10.3847%2F1538-4357%2Faa7ed7.

[109] S. M. Ransom et al. “THREE MILLISECOND PULSARS IN FERMI LAT UNASSOCIATED BRIGHT SOURCES”. In: *The Astrophysical Journal* 727.1 (Dec. 2010), p. L16. DOI: 10.1088/2041-8205/727/1/l16. URL: https://doi.org/10.1088%2F2041-8205%2F727%2F1%2Fl16.

[110] P. S. Ray et al. “Precise γ-ray Timing and Radio Observations of 17 Fermi γ-ray Pulsars”. In: *apjs* 194.2, 17 (June 2011), p. 17. DOI: 10.1088/0067-0049/194/2/17. arXiv: 1011.2468 [astro-ph.HE].

[111] P. S. Ray et al. “RADIO DETECTION OF THE iFERMI/i -LAT BLIND SEARCH MILLISECOND PULSAR J1311–3430”. In: *The Astrophysical Journal* 763.1 (Jan. 2013), p. L13. DOI: 10.1088/2041-8205/763/1/l13. URL: https://doi.org/10.1088%2F2041-8205%2F763%2F1%2Fl13.

[112] Florent Renaud, Oscar Agertz, and Mark Gieles. “The origin of the Milky Way globular clusters”. In: *Monthly Notices of the Royal Astronomical Society* 465.3 (Nov. 2016), pp. 3622–3636. DOI: 10.1093/mnras/stw2969. URL: https://doi.org/10.1093%2Fmnras%2Fstw2969.

[113] A. Ridolfi et al. “Long-term observations of the pulsars in 47 Tucanae – I. A study of four elusive binary systems”. In: *Monthly Notices of the Royal Astronomical Society* 462.3 (July 2016), pp. 2918–2933. ISSN: 0035-8711. DOI: 10.1093/mnras/stw1850. eprint: https://academic.oup.com/mnras/article-pdf/462/3/2918/8012538/stw1850.pdf. URL: https://doi.org/10.1093/mnras/stw1850.

[114] K. F. Riley, M. P. Hobson, and S. J. Bence. *Mathematical Methods for Physics and Engineering: A Comprehensive Guide*. 2nd ed. Cambridge University Press, 2002. DOI: 10.1017/CBO9781139164979.

[115] Leszek Roszkowski, Enrico Maria Sessolo, and Sebastian Trojanowski. “WIMP dark matter candidates and searches—current status and future prospects”. In: *Reports on Progress in Physics* 81.6 (May 2018), p. 066201. DOI: 10.1088/1361-6633/aab913. URL: https://doi.org/10.1088%2F1361-6633%2Faab913.

[116] Eric M. Schlegel et al. “Gamma-Ray Emission from Cataclysmic Variables. I. The Compton EGRET Survey”. In: *apj* 439 (Jan. 1995), p. 322. DOI: 10.1086/175175.

[117] Zhengyi Shao and Lu Li. “Gaia parallax of Milky Way globular clusters – A solution of mixture model”. In: *Monthly Notices of the Royal Astronomical Society* 489.3 (Aug. 2019), pp. 3093–3101. DOI: 10.1093/mnras/stz2317. URL: https://doi.org/10.1093%2Fmnras%2Fstz2317.

[118] Linda S. Sparke and John S. Gallagher III. *Galaxies in the Universe: An Introduction*. 2nd ed. Cambridge University Press, 2007. DOI: 10.1017/CBO9780511807237.

[119] Ingrid H. Stairs. “Testing General Relativity with Pulsar Timing”. In: *Living Reviews in Relativity* 6.1 (Sept. 2003). DOI: 10.12942/lrr-2003-5. URL: https://doi.org/10.12942%2Flrr-2003-5.

[120] Lister Staveley-Smith et al. “A search for annihilating dark matter in 47 Tucanae and Omega Centauri”. In: *pasa* 39, e026 (June 2022), e026. DOI: 10.1017/pasa.2022.23. arXiv: 2205.01270 [astro-ph.HE].

[121] Floyd W. Stecker, Chris R. Shrader, and Matthew. A. Malkan. “The Extragalactic Gamma-Ray Background from Core-dominated Radio Galaxies”. In: *The Astrophysical Journal* 879.2 (July 2019), p. 68. DOI: 10.3847/1538-4357/ab23ee. URL: https://doi.org/10.3847/1538-4357/ab23ee.

[122] Meng Su, Tracy R. Slatyer, and Douglas P. Finkbeiner. “GIANT GAMMA-RAY BUBBLES FROMiFERMI/i-LAT: ACTIVE GALACTIC NUCLEUS ACTIVITY OR BIPOLAR GALACTIC WIND?” In: *The Astrophysical Journal* 724.2 (Nov. 2010), pp. 1044–1082. DOI: 10.1088/0004-637x/724/2/1044. URL: https://doi.org/10.1088%2F0004-637x%2F724%2F2%2F1044.

[123] ESO/M.-R. Cioni/VISTA Magellanic Cloud survey. *The globular star cluster 47 Tucanae*. 2022. URL: https://www.eso.org/public/images/eso1302a/.

[124] P. H. T. Tam et al. “GAMMA-RAY EMISSION FROM THE GLOBULAR CLUSTERS LILLER 1, M80, NGC 6139, NGC 6541, NGC 6624, AND NGC 6752”. In: *The Astrophysical Journal* 729.2 (Feb. 2011), p. 90. DOI: 10.1088/0004-637x/729/2/90. URL: https://doi.org/10.1088%2F0004-637x%2F729%2F2%2F90.

[125] Marco Tavani. “Gamma Rays from Globular Clusters”. In: 407 (Apr. 1993), p. 135. DOI: 10.1086/172499.

[126] D. J. Thompson et al. “SAS-2 high-energy gamma-ray observations of the Vela pulsar.” In: *apjl* 200 (Sept. 1975), pp. L79–L82. DOI: 10.1086/181902.

[127] Sidney Van Den Bergh. “Globular clusters and dwarf spheroidal galaxies”. In: *Monthly Notices of the Royal Astronomical Society: Letters* 385.1 (Mar. 2008), pp. L20–L22. ISSN: 1745-3925. DOI: 10.1111/j.1745-3933.2008.00424.x. eprint: https://academic.oup.com/mnrasl/article-pdf/385/1/L20/6202339/385-1-L20.pdf. URL: https://doi.org/10.1111/j.1745-3933.2008.00424.x.

[128] Roeland P. van der Marel and Jay Anderson. “New Limits on an Intermediate-Mass Black Hole in Omega Centauri. II. Dynamical Models”. In: *apj* 710.2 (Feb. 2010), pp. 1063–1088. DOI: 10.1088/0004-637X/710/2/1063. arXiv: 0905.0638 [astro-ph.GA].

[129] G. van de Ven et al. “The dynamical distance and intrinsic structure of the globular cluster Omega Centauri”. In: *Astronomy &amp Astrophysics* 445.2 (Dec. 2005), pp. 513–543. DOI: 10.1051/0004-6361:20053061. URL: https://doi.org/10.1051%2F0004-6361%3A20053061.

[130] Pauli Virtanen et al. “SciPy 1.0: Fundamental Algorithms for Scientific Computing in Python”. In: *Nature Methods* 17 (2020), pp. 261–272. DOI: 10.1038/s41592-019-0686-2.

[131] Samuel S Wilks. “The large-sample distribution of the likelihood ratio for testing composite hypotheses”. In: *The annals of mathematical statistics* 9.1 (1938), pp. 60–62.

[132] Matthew Wood et al. *Fermipy: An open-source Python package for analysis of Fermi-LAT Data*. 2017. DOI: 10.48550/ARXIV.1707.09551. URL: https://arxiv.org/abs/1707.09551.

[133] Wei Wu et al. “Gamma-Ray Spectral Properties of the Galactic Globular Clusters: Constraint on the Number of Millisecond Pulsars”. In: *The Astrophysical Journal* 927.1 (Mar. 2022), p. 117. DOI: 10.3847/1538-4357/ac4f48. URL: https://doi.org/10.3847/1538-4357/ac4f48.

[134] Yi Xing and Zhongxiang Wang. “Fermi Study of Gamma-ray Millisecond Pulsars: the Spectral Shape and Pulsed Emission from J0614-3329 up to 60 GeV”. In: *apj* 831.2, 143 (Nov. 2016), p. 143. DOI: 10.3847/0004-637X/831/2/143. arXiv: 1604.08710 [astro-ph.HE].

[135] Pengfei Zhang, Yi Xing, and Zhongxiang Wang. *Discovery of gamma-ray pulsations of PSR J1835−3259B in the Globular Cluster NGC 6652*. 2022. DOI: 10.48550/ARXIV.2206.13667. URL: https://arxiv.org/abs/2206.13667.